

INFORMATION TO USERS

This manuscript has been reproduced from the microfilm master. UMI films the text directly from the original or copy submitted. Thus, some thesis and dissertation copies are in typewriter face, while others may be from any type of computer printer.

The quality of this reproduction is dependent upon the quality of the copy submitted. Broken or indistinct print, colored or poor quality illustrations and photographs, print bleedthrough, substandard margins, and improper alignment can adversely affect reproduction.

In the unlikely event that the author did not send UMI a complete manuscript and there are missing pages, these will be noted. Also, if unauthorized copyright material had to be removed, a note will indicate the deletion.

Oversize materials (e.g., maps, drawings, charts) are reproduced by sectioning the original, beginning at the upper left-hand corner and continuing from left to right in equal sections with small overlaps.

**ProQuest Information and Learning
300 North Zeeb Road, Ann Arbor, MI 48106-1346 USA
800-521-0600**

UMI[®]

**Fluid and Particle simulations of the Interaction
of the Solar Wind with Magnetic Anomalies
on the Surface of the Moon and Mars.**

Erika Megan Harnett

**A dissertation submitted in partial fulfillment
of the requirements for the degree of**

Doctor of Philosophy

University of Washington

2003

Program Authorized to Offer Degree: Department of Earth and Space Sciences

UMI Number: 3079223

Copyright 2003 by
Harnett, Erika Megan

All rights reserved.

UMI[®]

UMI Microform 3079223

Copyright 2003 by ProQuest Information and Learning Company.
All rights reserved. This microform edition is protected against
unauthorized copying under Title 17, United States Code.

ProQuest Information and Learning Company
300 North Zeeb Road
P.O. Box 1346
Ann Arbor, MI 48106-1346

**©Copyright 2003
Erika Megan Harnett**

In presenting this dissertation in partial fulfillment of the requirements for the Doctoral degree at the University of Washington, I agree that the Library shall make its copies freely available for inspection. I further agree that extensive copying of this dissertation is allowable only for scholarly purposes, consistent with "fair use" as prescribed in the U.S. Copyright Law. Requests for copying or reproduction of this dissertation may be referred to Bell and Howell Information and Learning, 300 North Zeeb Road, Ann Arbor, MI 48106-1346, to whom the author has granted "the right to reproduce and sell (a) copies of the manuscript in microform and/or (b) printed copies of the manuscript made from microform."

Signature Erika Obernott

Date March 14, 2003

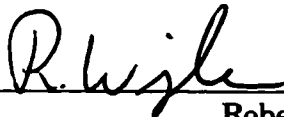
University of Washington
Graduate School

This is to certify that I have examined this copy of a doctoral dissertation by

Erika Megan Harnett

and have found that it is complete and satisfactory in all respects,
and that any and all revisions required by the final
examining committee have been made.

Chair of Supervisory Committee:



Robert M. Winglee

Reading Committee:



Robert Winglee



Robert Holzworth



Ronald Merrill

Date: March 14, 2003

University of Washington

Abstract

**Fluid and Particle simulations of the Interaction
of the Solar Wind with Magnetic Anomalies
on the Surface of the Moon and Mars.**

by Erika Megan Harnett

Chair of Supervisory Committee:

Professor Robert M. Winglee
Earth and Space Sciences

Simulations of the solar wind interacting with the Moon and Mars indicate that the presence of magnetic anomalies on the surface can lead to the formation of mini-magnetospheres around the anomalies. These mini-magnetospheres are not just small scale versions of planetary magnetospheres, but rather their small size leads to merged boundaries. Mini-magnetospheres also possess an increased sensitivity to solar wind parameters, the IMF direction in particular. The small scale size also leads to non-ideal MHD behavior, such as localized charge separation, which modifies particle acceleration, and ion cyclotron effects that lead to evolution of the magnetic field.

This thesis presents results that show that mini-magnetospheres at the Moon, while small in comparison to the size of the Moon, can change the size and shape of the wake region even when the anomalies are on the day side. Some magnetic field configurations can completely prevent solar wind access to the surface of the Moon, suggesting that the regions of surface magnetization may provide a source of material that has been exposed only to cosmic radiation.

The magnetic anomalies at Mars create a mini-magnetopause in place of the magnetic pileup boundary, and depending on IMF configuration lead to either an increase

of decrease in the scale height of the ionosphere opposite the magnetized region. Non-ideal MHD plasma behavior is associated with both the magnetic pileup boundary and the mini-magnetopause. The location of the magnetic anomalies greatly effects the plasma in the tail, leading to plasma voids and density enhancements that are several Martian radii in size.

TABLE OF CONTENTS

List of Figures	iii
List of Tables	v
Chapter 1: Introduction	1
1.1 Lunar Measurements	3
1.2 Previous Numerical Calculations for the Moon	10
1.3 Mars Global Surveyor Measurements	11
1.4 Previous Martian Simulations	19
1.5 Organization	19
Chapter 2: Numerical Methods	21
2.1 MHD Model	21
2.2 Particle Simulations	23
2.3 Non-ideal MHD	24
2.4 Calculation of Magnetic Anomaly Source	25
Chapter 3: Initial 2D MHD Lunar Simulations	26
3.1 Initial Conditions	27
3.2 Model Results	30
3.3 Discussion	36
3.4 Characteristics of a Satellite Fly-by	38
Chapter 4: 2.5D Particle and MPD Simulations	42
4.1 Lunar Particle Simulations	44
4.2 Non-ideal MHD Simulations	60

4.3	Comparison between particle and MPD simulations	70
4.4	Summary	73
Chapter 5:	2.5D Simulations of multiple dipole anomalies	75
5.1	Introduction	75
5.2	Model parameters	77
5.3	Two Dipoles	78
5.4	Four Dipoles	84
5.5	Summary	89
Chapter 6:	3D MPD Simulations of the Moon	91
6.1	Model and Initial Conditions	92
6.2	Single Dipole Magnetic Field Simulations	92
6.3	Global Effect for a Single Dipole	97
6.4	Multiple Dipole Magnetic Field Simulations	100
6.5	Discussion	103
Chapter 7:	3D MPD Simulations of Mars	105
7.1	Model	106
7.2	Northward vs. Southward IMF	109
7.3	Martian Magnetotail	116
7.4	Conclusions	122
Chapter 8:	Summary and Future Simulations	124
8.1	Martian magnetic pileup boundary	125
8.2	Saturian System	128
8.3	The Jovian Moons	131
Bibliography		133

LIST OF FIGURES

1.1	Lunar Magnetic Anomalies	5
1.2	Lunar Prospector Data for Five Successive Orbits	7
1.3	High Resolution Magnetic Field Measurements	8
1.4	Lunar Prospector Energy Spectrum Measurements	9
1.5	Martian Magnetic Anomalies	13
1.6	Position of the Martian Bow Shock	15
1.7	A Crossing of the Martian bow shock and the MPB	16
1.8	Martian Flux Spikes and Plasma Voids	18
3.1	Key to Figures	28
3.2	Pressure Contours for Three Different Initial Conditions	29
3.3	Case A: IMF in Ecliptic Plane	31
3.4	Case B: Southward IMF	32
3.5	Case C: Northward IMF	34
3.6	Cross-sectional cuts of Density, Temperature and Magnetic field	39
3.7	Two dipoles in anomalous region	41
4.1	Key to Figures	45
4.2	2.5D particle simulations : nominal case	48
4.3	Total Current	51
4.4	Electron Kinetic Energy and Velocity	52
4.5	Ion Kinetic Energy and Velocity	53
4.6	Velocity Distributions	55
4.7	Effect of Decreased Solar Wind Velocity	57
4.8	The Effect of mass ratios	59

4.9	MPD simulation - IMF and dipole moment Parallel	63
4.10	The Magnitude of the Pressure Gradient	64
4.11	The Magnitude of the Hall component	65
4.12	MPD simulation : IMF and dipole moment anti-parallel	67
4.13	MPD simulation : no IMF	69
5.1	2 Dipoles	80
5.2	4 Dipoles	86
6.1	Near Surface Density and Magnetic field lines for northward and southward IMF	93
6.2	2D vs 3D - IMF and dipole moment anti-parallel	94
6.3	2D vs 3D - IMF and dipole moment parallel	95
6.4	The Wake Region for Four Different Cases	98
6.5	3 dipoles and Northward IMF	101
7.1	The Simulated Martian Magnetic Field at 400 km	108
7.2	The Pressure in the Plane Running Through the Noon Meridian	109
7.3	Electric and Magnetic Field - South IMF	111
7.4	Electric and Magnetic Field - North IMF	112
7.5	The Effect of the Anomalies on Ionospheric Scale Height	114
7.6	Nightside density percent difference	117
7.7	Streamlines around Mars for equal day and night side densities	118
7.8	Night side Density - 1/10th reduction	120
7.9	Streamlines around Mars for reduced night side densities	121

LIST OF TABLES

5.1	2 dipoles	79
5.2	4 Dipoles	85

ACKNOWLEDGMENTS

The work presented here could not have been completed without the help from my adviser Professor Robert Winglee. Not only has his support and advice been crucial for my success, he also makes coming in to work fun. Further thanks goes to Professors Bob Holzworth, Ron Merrill, Micheal McCarthy and Don Brownlee for their scientific guidance and the many thoughtful discussions we have had over the years.

I also want to thank my fellow graduate students, Sean Matt and Carol Paty for our many discussions, be they scientific or non-scientific. And I especially wish to thank Laurel Rachmeler for help in generating so many of the images found in this thesis.

The research presented in this thesis was supported by the NASA Graduate Student Research Fellowship NGT-5-50285.

DEDICATION

To my parents for their unwavering support.

Chapter 1

INTRODUCTION

Examples of large scale magnetospheres are quite common in nature. They occur around planets, stars and other astronomical bodies. The plasma interactions that occur within magnetospheres leads to a wide variety of dynamics. The interaction of the Earth's magnetic field with the solar wind leads to a magnetosphere that protects the atmosphere from erosion by the solar wind, sheltering the life that lives on the surface below. The strong magnetic field and rapid rotation of Jupiter, on the other hand, leads to a environment inside the magnetosphere bathed in harmful, high energy particles. And the feedback between Jupiter and it's moons, generates EM signals that indicate the existence of moons with ion sources and magnetic fields. The strong magnetic fields and rotation of young stars may lead to the formation of massive jets emanating from the poles.

While the magnetic field strengths and dynamics may differ for all these cases, they all share the characteristic that the magnetic fields are global in structure and large enough in size that particle interactions occur over a distance much smaller than the scale size of the magnetosphere. But if the magnetic fields are localized to a small region on a moon, planet or star, particle processes would be occurring over a range comparable to the scale size of the structure. Also, if the magnetic fields are embedded in rock, and there is no substantial ionosphere around the moon or planet, then the surface acts solely as a sink for particles. This is unlike most planetary sized magnetospheres, like the Earth, where the ionosphere provides both a sink and source for particles.

While the regions involved are smaller than the planet or moon, they could interact with the ambient plasma (such as the solar wind) in such a way to form a small scale

magnetosphere, or mini-magnetosphere. The presence of a mini-magnetosphere was first suggested to explain the solar wind plasma and magnetic field modification seen near the Moon by Lunar Prospector [45]. Identification of other mini-magnetospheres has yet to be made but this work could help determine the signatures to look for. Magnetic anomalies have also been found on Mars, with the potential for localized magnetic fields existing on other planetary bodies, such as the moons of Jupiter. And the interaction of plasma and twisted magnetic fields originating from the Sun may be the mechanism that heats the plasma in the corona so that it is 1000 times hotter than the surface.

In addition to providing insight into magnetospheric dynamics, mini-magnetospheres form in the region where plasma begins to transition from acting collectively as an MHD fluid to one where gyroradius and charge separation effects control the dynamics. Comparison of fluid simulations and particle simulations with data in this regime may help determine how the transition between particle and fluid behavior occurs, which would provide important insight into a wide range of plasma physics applications.

One example of possible applications is in addressing unresolved issues arising from data taken during the Apollo missions. Solar wind measurements made on the lunar surface by the ALSEP instrument [54, 17] showed possible modulation of the incident ions by nearby magnetic anomalies. *Hood and Williams* [29] proposed that such modulation could explain the variation in surface albedo near anomalous regions, for example the markings near Reiner Gamma. Such modulation could affect chemical composition of the surface. *Hood and Williams* suggested that regions where the solar wind is deflected would reduce the deposition of hydrogen, leading to a surface that has not been darkened by impact of solar wind particles. This shielding of the surface from space weathering at the Moon could provide a source of material that has been subject to primarily galactic radiation exposure. This type of material would be of great use for determining the isotopic makeup of the early system and have implication in the study of the formation of the solar system.

At Mars, the anomalous regions could supplement the partial shielding of cosmic

rays provided by the atmosphere. Localized magnetic fields at the Galilean moons could also provide similar shielding but from the deadly radiation generated inside the Jovian magnetosphere. Possible radiation shielding has astrobiological implications where primitive life has been suggested as existing at an early Mars [38] and theorized for a watery Europa.

This thesis presents model based predictions for the structure and dynamics of mini-magnetospheres occurring around magnetic anomalies on the surface of the Moon and Mars, and compares those predictions to observations where data is available. The work was initially motivated by the claim from the Lunar Prospector research team that the satellite had traveled through a mini-magnetosphere over the Serenitatis antipode [45]. The discovery of magnetic anomalies on the surface of Mars and the possibility that the research could lead to insight about plasma properties in general, lead to the expansion of the project into the work detailed here. This thesis presents a model for the behavior of plasmas around localized magnetic sources at the Moon and Mars, and determines that non-ideal MHD behavior is extremely important in describing the dynamics of the resulting mini-magnetospheres. The comparison of the particle and fluid type behavior with observations also provides the initial steps in the development of a theory describing the nature of the transition of a plasma between collective, fluid interactions and turbulent, single particle interactions.

This chapter discusses the global magnetic field maps made at the Moon and Mars, indicating both possess strong surface magnetization. It also discusses the early indications from Apollo measurements that the solar wind may interact with magnetic anomalies and the previous work done by Hood et al.[28, 29] to explain the high Lunar surface albedo in the vicinity of some magnetic anomalies. Also presented in this chapter are the recent plasma measurements made at Mars and some of the other initial modeling attempts made to investigate the Martian magnetosphere.

1.1 Lunar Measurements

Lunar magnetic field measurements made during the Apollo missions provided the first suggestions that the Moon has regions of high magnetic field. Satellite-based

magnetometers measured regions of magnetic fields up to 100 km in size. Ground-based measurements found field strengths up to 300 nanotesla [46]. *Dyal et al.* [15] compared orbital magnetometer data from Apollo missions that did not make surface field measurements with those missions that did and determined that field strengths on the order of 1000 nT at the surface and 2 nT at 100 km above the surface may be present in some small regions.

In 1998, Lunar Prospector mapped the magnetic field strengths over the entire Lunar surface using both magnetometers and electron reflection detectors, and found surface magnetic fields up to 300 nT (for 5° by 5° resolution), on spatial scales of 7 to 1000 km [45] (Figure 1.1). The magnetized regions located near the antipodes of the Imbrium and Serenitatis impact craters are 1200 km and 740 km (respectively) in diameter with a magnitude on the order of 300 nT for a large portion of those regions.

Also seen was the indication by Lunar Prospector (LP) that these localized magnetized regions are strong enough to hold off the solar wind and possibly form a bow shock. This bow shock is seen in the LP data as enhancements in the magnetic fields at the satellite altitudes when compared to the same region when it was in the vacuum of the Lunar wake (Figure 1.2). In conjunction with measurements indicating a change in the shape of the electron spectrum (Figure 1.4) and small changes in the angle of the magnetic field (Figure 1.3), it was concluded that the surface magnetic fields were able to cause a pile-up of the interplanetary magnetic field (IMF).

When the energy spectrum of electrons at three different locations around a shock structure (Figure 1.3) was calculated, the slope of the spectrum changed as LP traveled through the region (Figure 1.4). Bow shocks are a region of particle acceleration and the region upstream contains high energy particles that have been reflected and accelerated by the shock. Inside the bow shock, in the magnetosheath, the kinetic energy of the particles is converted into thermal energy. The energy spectra from Lunar Prospector show a decrease of low energy particles and increase of high energy particles, consistent with the satellite crossing a foreshock region. As LP traveled further into the region, the energy spectrum steepened as the electrons were decelerated. If

Lunar Prospector Electron Reflectometry

NORTH POLE

SOUTH POLE

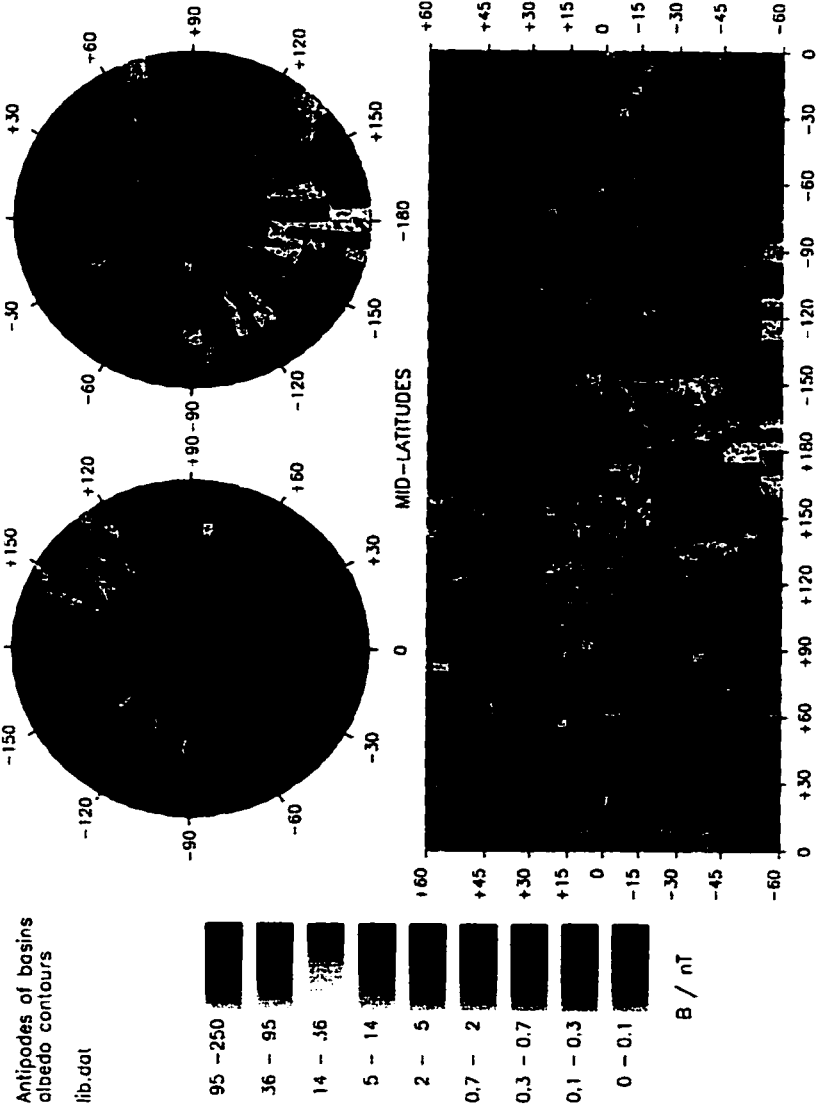


Figure 1.1: Lunar Magnetic Anomalies: Electron Reflection mapping of the surface magnetic field by Lunar Prospector. The resolution is 5° by 5°. The white circles indicate the antipodes of large impact basins. The two circles at the Imbrium antipode mark the main rim and partial outer rim, with a diameter of 1200 km and 1500 km respectively. The diameter of the Serenitatis rim is 740 km. From Lin, private communication, 1999

the satellite was measuring only the effects of an increase in surface magnetic field, the increased mirroring height and decrease in loss of electrons to the surface would correspond to a uniform increase in the flux at all energies and not a change in the slope of the spectrum.

If LP measured an unmodified surface magnetic field, large changes in the angle of the magnetic field should have been measured. Instead, only small angle changes were measured (Figure 1.2). This suggested to the Lunar Prospector team that the increase in the magnitude of the magnetic field was due to compression of the IMF, as it draped around the anomalous field.

The idea of small scale magnetospheres, or “mini-magnetospheres”, was reinforced by one set of measurements showing the disappearance and reappearance of an increase in the magnetic field at the satellite altitude during five successive orbits over an anomalous region. The disappearance, as detected in the fourth orbit in Figure 1.2, coincided with a large increase in the dynamic pressure of the solar wind. If LP was measuring only an unmodified surface field, its presence would not have been affected by the solar wind. Therefore *Lin et al.* [45] concluded that the increase in magnetic field measured over the anomaly was the pile-up of the IMF at a shock surface and when the dynamic pressure of the solar wind increased, the shock surface dropped below the altitude of the satellite.

Shock regions may have also been measured by the Apollo 15 and 16 satellites. As the satellites approached the terminator, they would occasionally measure an increase in the magnetic field. *Russell and Lichtenstein* [60] defined this “limb compression” as a 1.5 or greater amplification of the solar wind magnetic field at or in front of the terminator and analyzed the rate and location of limb compression. They showed the occurrence was not correlated to the direction of the IMF but rather appeared to coincide with regions of surface magnetization. The locations that they indicated as having a high occurrence rate for limb compression are in the vicinity of the Imbrium, Serenitatis, and Oriental antipodes; all three being large regions of high surface magnetic field. *Russell and Lichtenstein* concluded that it was highly likely that limb compressions were caused by deflection of the solar wind by magnetic anomalies in the limb

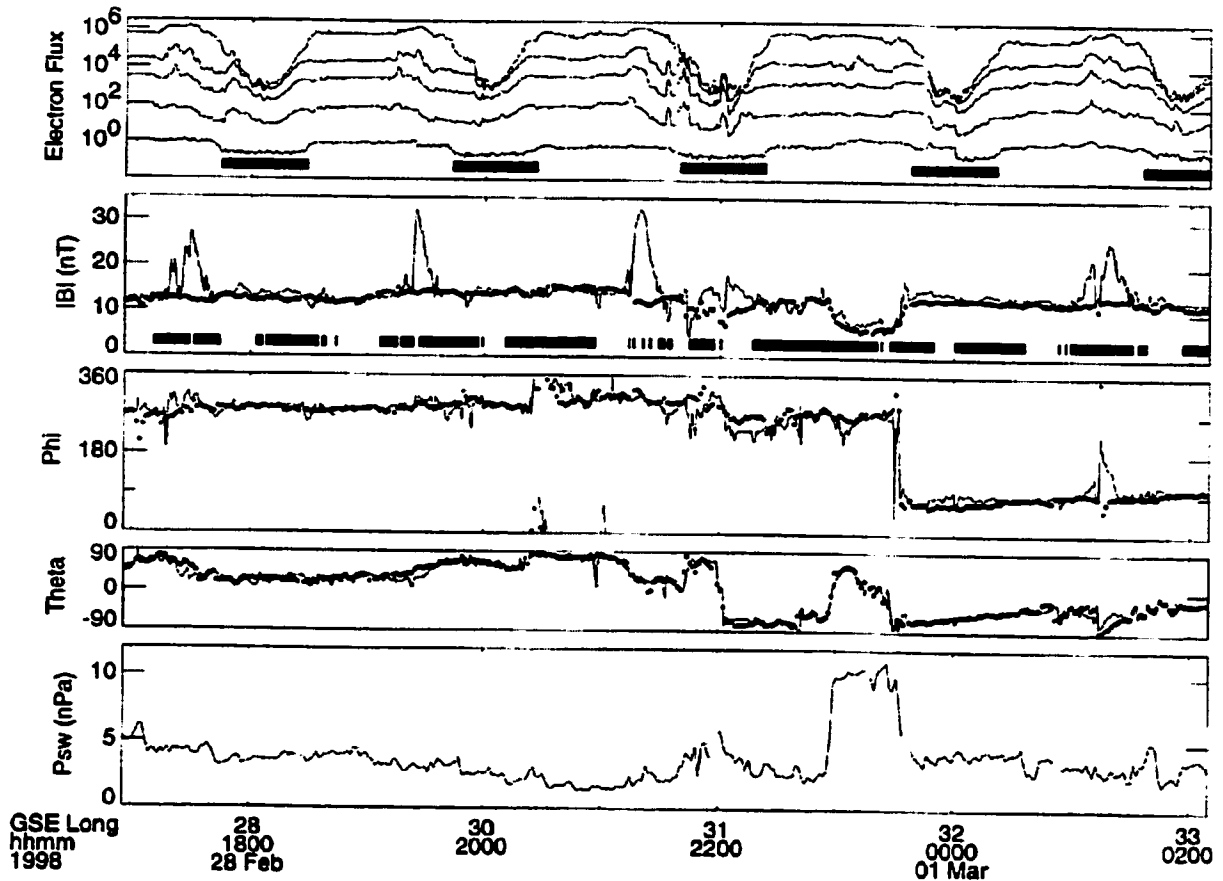


Figure 1.2: Lunar Prospector data for five successive orbits over the Serenitatis antipode (at approximately 180° longitude) while the Moon was in the solar wind. The solar wind pressure trace and the dark spots superimposed on the magnetic field data are measurements made by the Wind satellite. Wind was 1.2 million km up-stream and the data was shifted by 50 minutes to account for the travel time between Wind and the Moon. The black bars on the electron flux plot indicate when LP was in the Lunar wake and the ones on the magnetic field magnitude plot mark where LP was magnetically connected to the Moon. From *Lin et al.*, 1998 [45].

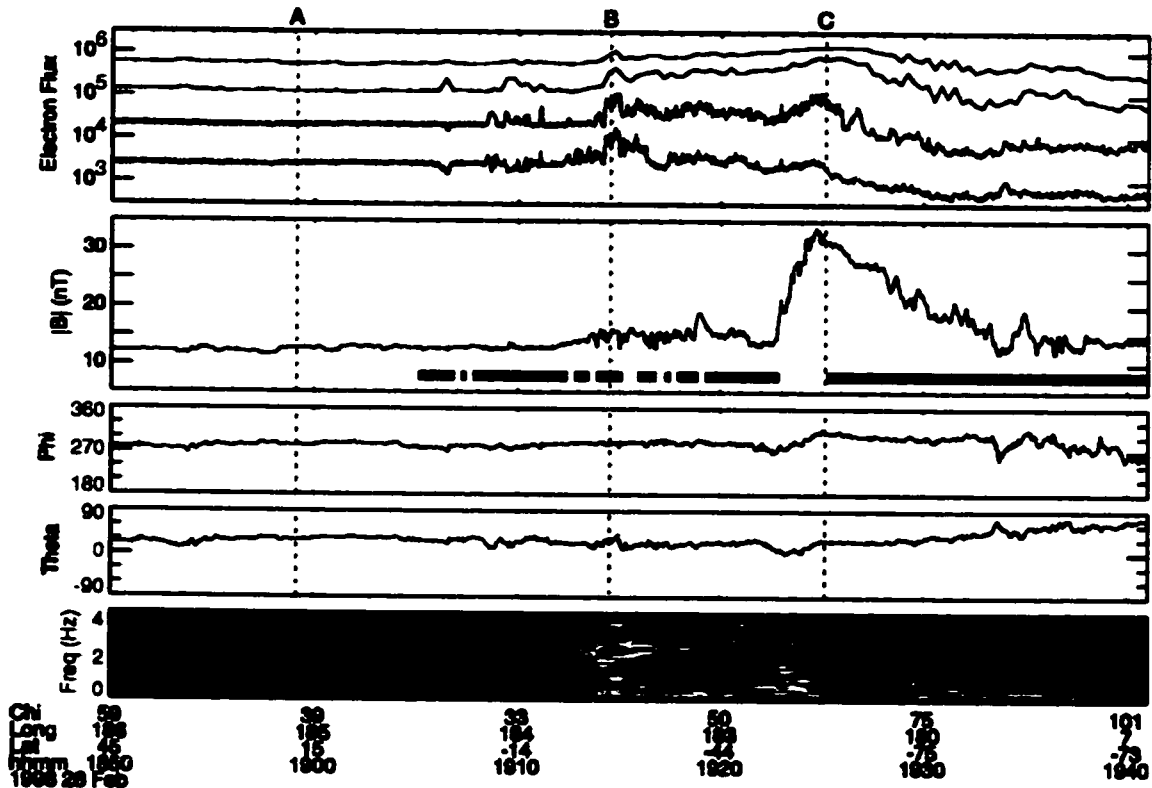


Figure 1.3: High resolution magnetic field measurements for the second orbit in Figure 1.2. Position (A) is the unaltered electron spectrum. At point (B) the satellite entered the shock region and is inside the shock at point (C). From *Lin et al.*, 1998 [45].

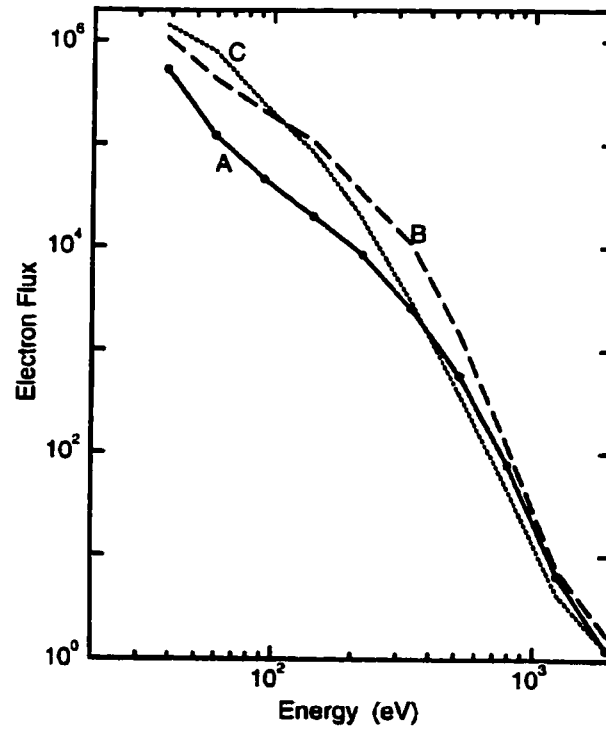


Figure 1.4: Lunar Prospector energy spectrum measurements for electron energy at the three points indicated in Figure 1.3. From *Lin et al.*, 1998 [45].

region and that the size of the compressions was controlled by direction of the IMF. Conclusive proof could not be obtained at the time due to limited data and the question was left unresolved.

Solar wind measurements made on the Lunar surface by the ALSEP instrument [54, 17] showed possible modulation of the incident ions by nearby magnetic anomalies. The ALSEP detector was situated at the location of the Apollo 12 landing site (3.01°S , 23.42°W). *Neugebauer et al.* [54] showed that instead of the solar wind rise preceding sunrise by the same amount of time that solar wind set preceded sunset, the solar wind rise occurred later than sunrise. This would occur if some mechanism to the east of the ALSEP deflected the solar wind away from the detector. Transient events were also measured by ALSEP [17]. *Freeman* [17] showed that in addition to the anomalous sunrise effect, bursts of solar wind ions with energies equal to and below solar wind energies were measured while ALSEP was deep in the Lunar night. Both characteristics can be explained by an interaction of the solar wind with the magnetic anomaly at the Orientale antipode, at approximately (15°N , 90°W).

1.2 Previous Numerical Calculations for the Moon

In attempt to explain the high albedo of the Lunar surface in the regions of large crustal magnetic fields, *Hood and Schubert* [28] theorized that the regions were shielded from the solar wind by large surface magnetic fields. They analytically determined that due to the charge separation that occurs in the finite thickness of a magnetopause, the effective scale size necessary for the anomalous region is not the proton gyroradius, but rather the geometric mean of the electron and proton gyroradii. The charge separation creates an electric field which transfers momentum from the protons to the electrons. They also showed that in order for the solar wind to be held off of the surface due to only the balance between the dynamic pressure of the solar wind and the magnetic pressure of the source region, the horizontal scale size must be much larger than the geometric mean of the electron and proton gyroradii. If the horizontal scale size is not large enough, forces due to field gradients become significant and a much stronger surface field is necessary. By assuming a buried dipole with

the magnetic moment parallel to a planar surface, *Hood and Schubert* determined that for solar wind velocities and densities of 400 km/s and $10/\text{cm}^3$, respectively, the dipole moment must be much greater than $5 \times 10^{13} \text{G} \cdot \text{cm}^3$ in order for field gradients to be insignificant. For a dipole buried 2 km below the surface, that translates to a surface magnetic field of 625 nT and 0.005 nT at 100 km above the surface along the dipole moment equator.

Later *Hood and Williams* [29] mapped the 3D particle trajectories for single particles interacting with Lunar magnetic anomalies. Their model neglected any collective effects on the incident particles and simply looked at the deflection of single particles by the Lorentz force. An estimate of the total deflection came from combining the results for an array of single particle interactions. *Hood and Williams* modeled the magnetic anomalies as a collection of 9-15 buried dipoles, contained in a region 100-200 km in diameter. The total field strengths were much greater than 1000 nT at the surface and on the order of 2 nT at 100 km above the surface. Their model predicted that the magnetic anomalies could produce a measurable deflection of the solar wind. They found that for surface fields above 1000-1200 nT, a large portion of the surface was shielded from incident ions. But for surface field strengths less than 800 nT little deflection occurred and the surface flux was negligibly different from the incident flux. Since collective effects were ignored, the model underestimated the deflection of ions by the anomalies and could not predict the formation of shocks or modification of the surface fields. *Hood and Williams* also focused on regions an order of magnitude smaller than the anomalous regions in the Imbrium and Serenitatis antipodes.

1.3 Mars Global Surveyor Measurements

Strong surface magnetic fields have also been detected on Mars by the Mars Global Surveyor [1, 8]. Magnetic fields in excess of 1500 nT were measured, with scale sizes up to 100 kilometers wide and 2000 kilometers long (Figure 1.5). The field strengths are at satellite altitudes when MGS was in an orbit between 100 and 200 km above the surface, since the density of the atmosphere prevented the use of the electron reflection telescope to measure the surface field directly via mirroring electrons.

Mars does not appear to have a global magnetic field generated by a dynamo. It does have an atmosphere thick enough for clouds and giant wind storms to form. The peak ionospheric density of approximately 10^5cm^{-3} occurs between 100 and 130 km above the surface (depending on solar activity) [16, 22], only about an order of magnitude smaller than the peak ion density in the Earth's ionosphere. Thus the ionospheric portion of the atmosphere has a high enough density that it can hold off the solar wind through thermal pressure alone, forming an ionopause at the location of pressure balance and a bow shock at about $0.7R_M$ (cf. [72, 10]) from the surface. Any effect by the magnetic anomalies would be to modify the existing magnetosphere rather than create a magnetosphere every time the anomalous region faced into the solar wind as in the case of the Moon. Above the anomalous region, a magnetopause would be created in place of an ionopause, introducing a large scale current system on top of the current generated by the interaction of the ionosphere with the incident IMF.

Vignes et al. [72] found large variation in the position of the Martian bow shock, as measured by Mars Global Surveyor (Figure 1.6). That its mean position compared well with measurements made by Phobos-2, nine year prior, suggested that the bow shock position is independent of solar cycle phase. Instead, the fluctuation in the bow shock is due to variations on a shorter time scale, such as the solar wind conditions or magnetic anomalies. Analyzing the location of the bow shock from 553 crossings, *Vignes et al.* [71] found no longitudinal dependence on the location and thus concluded that the southern anomalies do not affect the bow shock location. They did find a latitudinal asymmetry associated with mass loading by pickup ions. For the IMF in the $+B_y$ direction, this translated to the bow shock in the northern hemisphere being further away from the planet than in the southern hemisphere.

In between the Martian bow shock and ionopause, forms a magnetic pile-up boundary (MPB). *Crider et al.* [10] define the MPB is the location where the magnetospheric plasma transition from being shocked solar wind plasma to a region the flow lines are mass loaded by exospheric ions. It is also a location where the solar wind proton flux disappears due to charge exchange interactions with the planetary exosphere [59], and can be tens to hundreds of kilometers thick [50]. The solar wind electron population

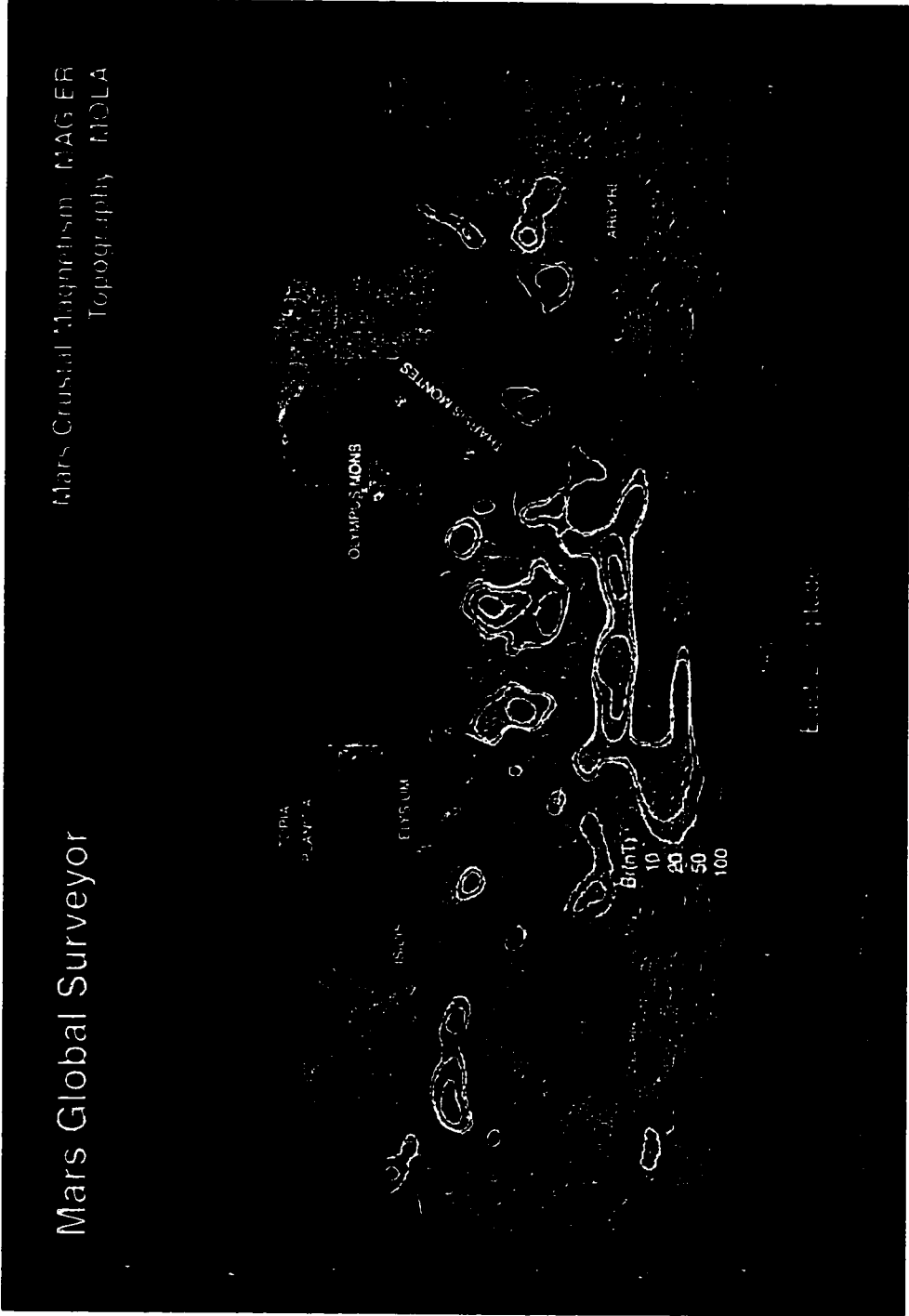


Figure 1.5: Martian Magnetic Anomalies: The magnitude of the radial component of the Martian magnetic field superimposed on a topographic map. From Connerney et al., 2001 [7]

is also greatly reduced through impact ionization of exospheric particles [11] (Figure 1.7). The total number of electrons increases due to electron impact ionization at the MPB but the solar wind electrons rapidly lose energy through the ionization process, and become indistinguishable from ionospheric electrons. Both solar wind electrons and IMF can both flow across the boundary [50]. The transition from outside the MPB to inside appears as a large increase in the magnitude of the magnetic field (Figure 1.7) with a simultaneous sharp decrease in the electron flux [72], as solar wind electrons begin ionizing planetary hydrogen and oxygen [11].

The location of the magnetic pile-up boundary layer is also largely variable, with the night-side location fluctuating more than the day side location. But the mean location is also independent of the solar cycle [72]. *Crider et al.* [10] found that the location of the MPB shows both latitudinal and longitudinal dependence. The average height of the MPB was 200 km higher on the day-side southern hemisphere than the day-side northern hemisphere. In the southern hemisphere, the average MPB height opposite the largest anomalous region is both 140 km higher than outside the anomalous region and more variable.

Observations using both radio occultation from MGS [52] and the MAG/ER instrument on MGS [50] show that the Martian magnetic anomalies lead to an increased scale height of the Martian ionosphere in the vicinity of the anomalies. *Mitchell et al.* [50] found the anomalies in the Arabia Terra region ($\sim 0 - 40^\circ\text{N}$ and $\sim 30^\circ\text{W} - 90^\circ\text{E}$) do not affect the location of the ionopause as the anomalous magnetic field is too weak to significantly modify the ionosphere at 400 km above the surface, where the ionopause would form due to thermal pressure alone. The data taken during aerobraking did not allow for a detailed analysis of the structure of the ionopause by the MAG/ER instrument over the strongest magnetic anomalies in the Southern hemisphere. *Ness et al.* [52] found that the electron density profiles in the Arabia Terra region are modified only slightly from the profiles above unmagnetized regions. Above the strong anomalies in the southern hemisphere, the electron density profiles are significantly modified.

Mitchell et al. [50] found multiple ionopause crossings in a single orbit, suggesting

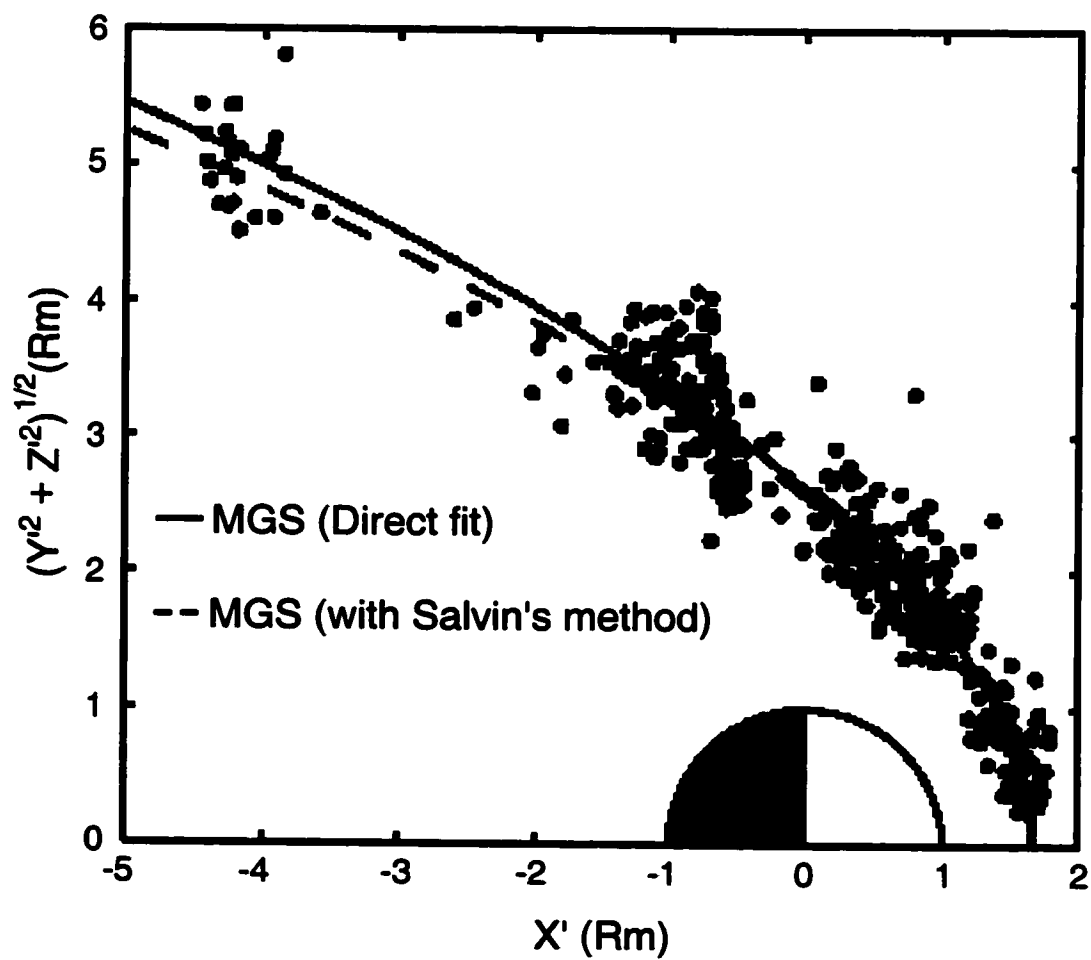


Figure 1.6: Positions of the Martian bow shock crossings made by Mars Global Surveyor. From *Vignes et al.*, 2000 [72].

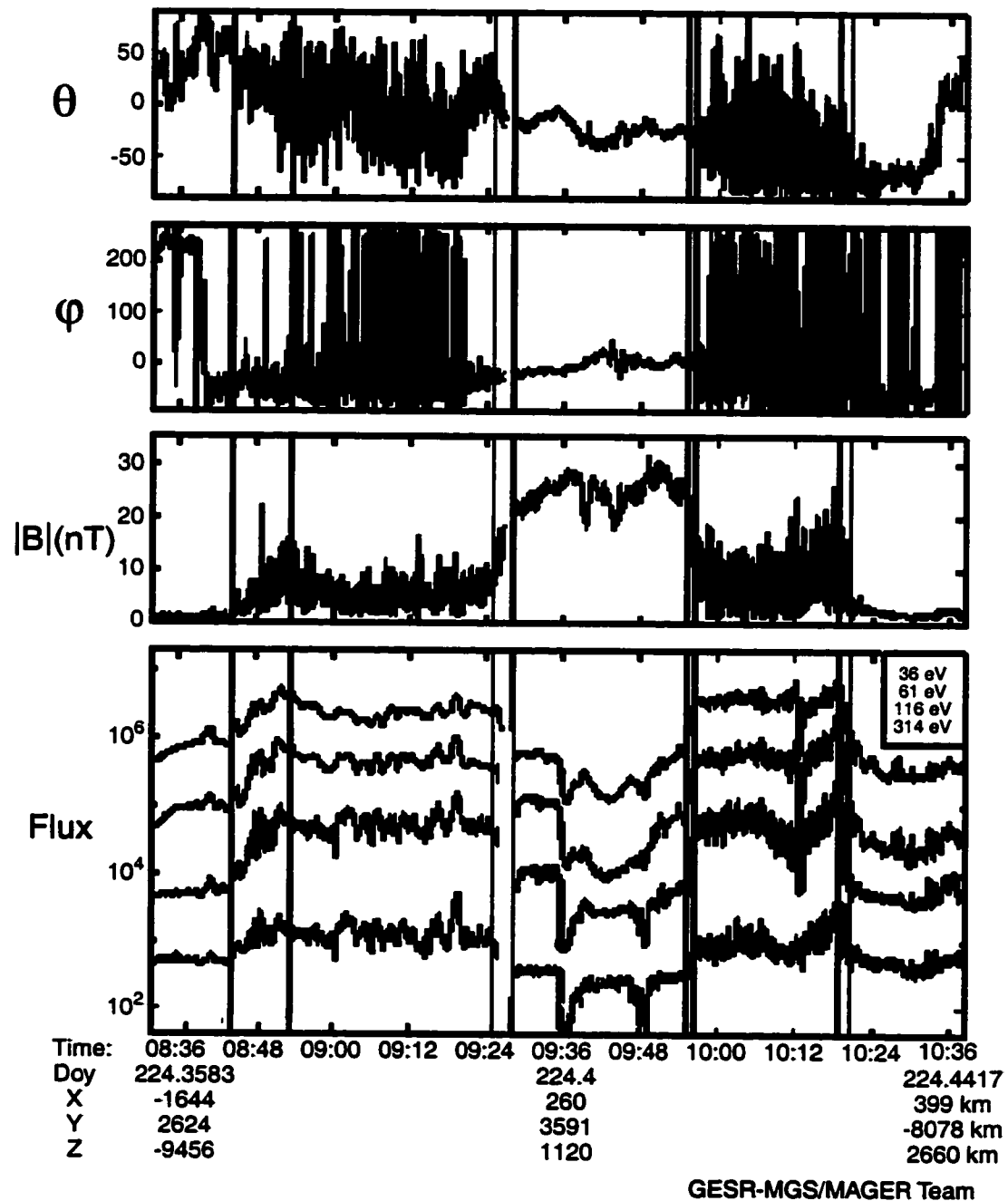
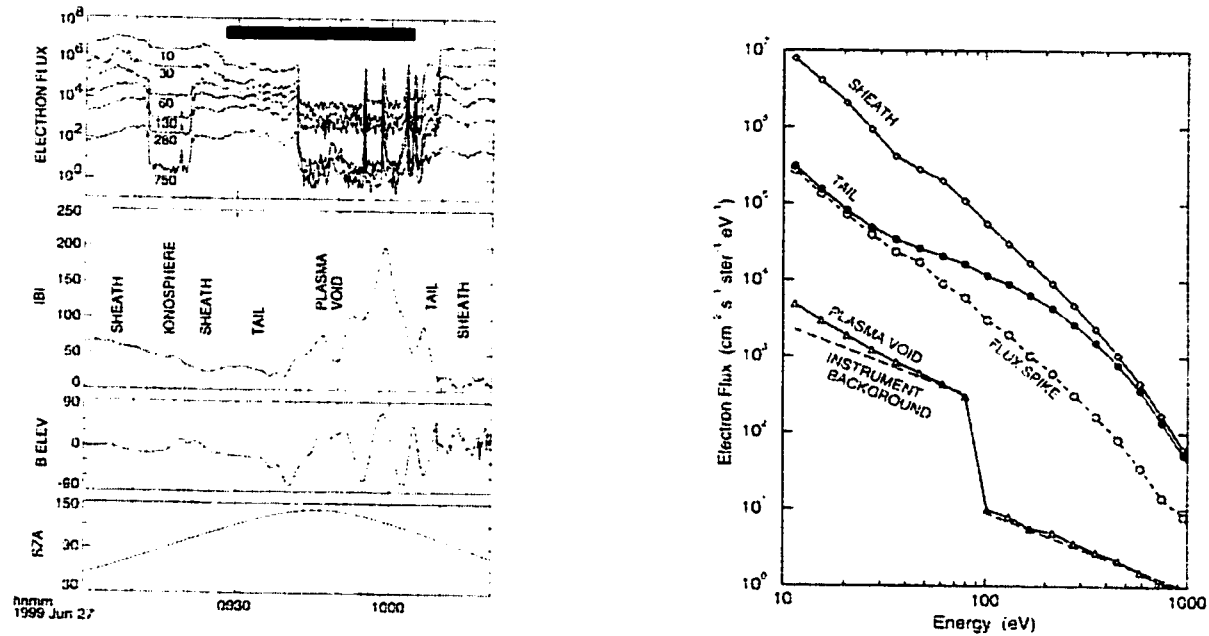


Figure 1.7: A crossing of the Martian bow shock and the MPB (magnetic pile-up boundary) by MGS. The dark lines around 08:48 UT and 10:20 UT indicate when MGS traversed the bow shock. MGS crossed the MPB in-bound at 09:26 UT and out-bound at 09:55 UT. From *Vignes et al.*, 2000 [72].

a complex morphology over several kilometers and/or movement of the ionopause on the order of 1 km/s. Their analysis showed that these fluctuations were not due to variations in the solar EUV flux. The fluctuations of the ionopause could also be due to variability in the solar wind conditions, as the solar wind conditions at the time are unknown. But they could also not rule out effects from the magnetic anomalies and the current systems they could generate in the ionosphere.

Ness et al. [52] found regions where the anomalous magnetic field is mostly radial, producing cusp-like structures. They proposed that the magnetic field could reconnect to the IMF, allowing solar wind to flow into the region, heating the atmosphere and inflating it. *Michell et al.* [50] then analyzed the characteristics of two adjacent regions of closed magnetic field line, one on either side of the terminator. The region on the night-side formed a “plasma void” region. This region was protected by the anomalous magnetic field from the solar wind traveling planetward, down the magnetotail, and from ionospheric plasma moving from the day side of the planet. The region on the day side had a reduced electron flux from the surrounding regions, but showed evidence of filling with locally produced ionospheric plasma. *Michell et al.* [50] also found that successive plasma voids would be separated by “flux spikes” (Figure 1.8), regions of plasma with an energy spectrum similar to magnetosheath plasma. This indicated that the magnetic field lines were once connected to the IMF. These “magneto-cylinders” are cusp-like in structure but have lateral sizes in excess of 2000 km, unlike the circular cusp at the Earth.

The magnetized region comprises approximately one quarter of the Martian surface and rotates in and out of the solar wind every 24.7 hours. Any interaction of the anomalies with the solar wind could therefore be dynamic and could cause large scale transport of plasma to the downstream region. Evidence of such tail transport is speculative and not yet conclusive as MGS is primarily a mapping satellite and is usually dormant during the nighttime portion of an orbit [*Dave Mitchell, private communication, 2001*].



(a) Flux spikes and magnetic field

(b) Energy spectrum of regions in (a)

Figure 1.8: Martian Flux Spikes and Plasma Voids: Examples of flux spikes separating plasma voids on the night-side of Mars (at 10:00 UT). The dark bar at the top indicates when MGS was in darkness. The electron flux is in units of $\text{cm}^{-2} \text{s}^{-1} \text{sr}^{-1} \text{eV}^{-1}$, with the traces for energy channels from 10 eV at the top to 840 eV at the bottom. The magnetic field is in units of nanotesla. The energy spectra are taken for correspondingly named regions in (a). The flux spike spectrum is for one flux spike in (a). From *Mitchell et al.*, 2001 [50].

1.4 Previous Martian Simulations

3D MHD simulations of the Martian magnetosphere have been conducted by *Ma et al.* [47]. They looked for the effects of a hot oxygen corona on the position of the bow shock and ionopause and found no significant changes in shape or position. When they added a model of the Martian magnetic field, they saw regions of closed magnetic fieldlines. The calculated position of the ionopause was also approximately 100 km further from the surface over the southern hemisphere than the northern hemisphere.

The *Ma et al.* model is ideal MHD and includes collisions with neutrals through tuned source and loss terms. They claim that they track multiple ion populations, but their model sets the unphysical condition that all of the ions have the same velocity and temperature. This effectively removes any physics associated with mass differences, thus reducing it back down to a single ion model. They also used a proxy to determine the location of the bow shock. Rather than using, say the gradient in the pressure, they set the position of the bow shock at the location where the total magnetic field was equal to 9 nT.

Brecht [3] used 3D hybrid simulations to look at the solar wind interaction with an unmagnetized Mars. Hybrid simulations allow for gyroscopic effects due to the large gyroradius of pick-up ions at Mars. *Brecht* predicted an asymmetric bow shock at Mars due to the large gyroradius of ions in the solar wind. The same calculations have not yet been repeated with the magnetic field included.

1.5 Organization

The organization of this thesis is as such. Chapter 2 discusses the numerical theory used to create the simulations. Chapter 3 details the initial 2D MHD simulations that were run initially to determine the possibility of mini-magnetospheres. The 2D results showed that not only the formation of mini-magnetospheres but also the large variability in shape with IMF conditions. Chapter 4 discusses the results from the 2.5D fluid and particle simulations investigating the non-ideal MHD and particle behavior of the plasma inside mini-magnetospheres. The comparison between the two types

of models show that fluid simulation do a good job of capturing the plasma physics at a mini-magnetosphere provided non-ideal MHD terms are included in Ohm's Law. Chapter 5 discusses the result of modeling the anomalous magnetic field with more than one dipole in 2.5D fluid simulations, thus investigating the effects of higher order moments on the structure of mini-magnetospheres. Models of the magnetic anomalies that include higher order terms are more realistic, as the magnetic fields from real magnetic anomalies are not dipolar in nature. Due to the fact that the interaction region between the solar wind and the anomalous magnetic field is close to the source region, the higher order moments are very important in determining the shape of the mini-magnetospheres that form. Chapter 6 presents the results from the 3D fluid simulations for the Moon, verifying the formation of mini-magnetospheres in 3D and showing the large scale effects that mini-magnetospheres can have on a system. Chapter 7 discusses the same results for Mars, as well as showing the large impact of the location of the southern anomalous region on the structure of the tail. Simulations of Mars are only shown for the 3D model as the larger ionospheric density of Mars prevents steady-state solutions in 2D. Chapter 8 summarizes the results and discusses the next step in the research to include multiple ion species and neutrals in the models and well as looking at other systems that could be studied with the models.

Chapter 2

NUMERICAL METHODS

The interaction of the solar wind with magnetic anomalies located on the Lunar and Martian surfaces is simulated using two different methods for representing the solar wind plasma, fluid and particle. Fluid simulations assume quasi-neutrality of the plasma and that the gyromotions of the plasma particles can be averaged over. Fluid simulations begin to break down when gyrotropic effects begin to dominate the behavior of the plasma. Modifications can be made to the fluid model to account for more particle-like behavior. Self-consistent particle simulation are also used to investigate where the fluid approximation breaks down and how the system behaves in that regime.

2.1 MHD Model

The ideal MHD equations will provide the basis for the fluid models presented. An ideal MHD fluid can be simulated by a combination of fluid dynamic equations and Maxwell's equations:

Continuity Equation

$$\frac{\partial \rho_m}{\partial t} + \nabla \cdot \mathbf{m} = 0 \quad (2.1)$$

Momentum Equation

$$\frac{\partial \mathbf{m}}{\partial t} + \frac{\mathbf{m}}{\rho_m} (\nabla \cdot \mathbf{m}) + (\mathbf{m} \cdot \nabla) \frac{\mathbf{m}}{\rho_m} + \nabla P = \mathbf{J} \times \mathbf{B}^{\text{tot}} \quad (2.2)$$

Energy Equation

$$\frac{\partial e}{\partial t} + \nabla \cdot \left(\frac{\mathbf{m}}{\rho_m} (e + P) \right) = \mathbf{E} \cdot \mathbf{J} \quad (2.3)$$

Faraday's Law

$$\frac{\partial \mathbf{B}}{\partial t} + \nabla \times \mathbf{E} = 0 \quad (2.4)$$

with *Ampere's Law*

$$\mathbf{J} = \nabla \times \mathbf{B} \quad (2.5)$$

and *Ohm's law* for closure

$$\mathbf{E} = -\mathbf{v} \times \mathbf{B} + \eta \mathbf{J} \quad (2.6)$$

where ρ_m is the mass density of the ion population, \mathbf{m} is the bulk momentum, e is the energy density (thus in units of J cm^{-3}), \mathbf{J} is the current, \mathbf{B} is the magnetic field, and \mathbf{E} is the electric field. η is the resistivity and equal to zero for ideal MHD. P is the gas pressure and equal to:

$$P = (\gamma - 1) \left[e - \frac{1}{2} \frac{|\mathbf{m} \cdot \mathbf{m}|}{\rho_m} \right]. \quad (2.7)$$

γ is the ratio of specific heats [56], and set to 1.4 for 2D simulations and $\frac{5}{3}$ for 3D.

A two step Lax-Wendroff process [58] is used to solve equations of the form:

$$\frac{\partial F}{\partial t} + \frac{\partial G(F)}{\partial x} + \frac{\partial H(F)}{\partial y} + \frac{\partial K(F)}{\partial z} = C \quad (2.8)$$

thus requiring Equation 2.2 to be in conservative form.

$$\frac{\partial \mathbf{m}}{\partial t} + \nabla \cdot \left(\mathbf{m} \frac{\mathbf{m}}{\rho_m} \right) + \nabla P = \mathbf{J} \times \mathbf{B}^{\text{tot}} \quad (2.9)$$

The variables, ρ_m , \mathbf{m} , e , and \mathbf{B} are assumed to be continuous at the simulation box boundaries. After the two step Lax-Wendroff, Lapidus smoothing [67] is used on ρ_m , \mathbf{m} , and e to remove numerical instabilities that arise at discontinuities, such as the bow shock.

Equations 2.4, 2.5, and 2.6 can be combined to form the transport equation for the magnetic field:

$$\frac{\partial \mathbf{B}}{\partial t} = \nabla \times (\mathbf{v} \times \mathbf{B}) + \frac{\eta}{\mu_o} \nabla^2 \mathbf{B} \quad (2.10)$$

The first term on the right hand side is the convection term and the second term is the diffusion term. For an ideal MHD plasma, $\eta = 0$, but the error in the numerical solution of the magnetic field differential equation is of order $\alpha \nabla^2 \mathbf{B}$. Thus the numerical error will allow diffusion to still occur. The effective resistivity associated with the numerical diffusion is $\alpha \mu_o$ or

$$\eta_{\text{num}} = \frac{\mu_o}{2} \Delta t v_o^2 \quad (2.11)$$

where Δt is the typical time step of the simulation and v_o is the typical Alfvén speed.

The magnetic field does need to diffuse through the Moon though. This is done by setting the resistivity in Equation 2.5 equal to zero everywhere except inside the object. The magnetic Reynolds number is the ratio of the convection term to the diffusion term

$$R_M = \frac{\mu_o v_o L_o}{\eta} \quad (2.12)$$

where L_o is the effective scale size. This ratio should be much greater than one for diffusion to be negligible and less than one for diffusion to dominate. For the resistivities set for the Moon and Mars in the simulations, the magnetic Reynolds number ranges between 0.4 for the Moon and just less than 1 for Mars.

As the numerical error leads to a numerical resistivity, an associated Reynolds number can be calculated. For the results presented in this thesis, R_{num} ranges from 1000 for the 3D simulations to over 50,000 for the 2D simulations. Thus convection dominates over numerically driven diffusion in the regions outside of the planet or moon.

A nested-box method is used for high resolution around the area of interest. The fluid equations are first solved on all grids independently. Then the values of the variables at points in the outer grid that overlap points in the inner grid, are replaced with the overlapping inner grid values. For internal grids, the boundary values are set by the outer grid where points overlap and interpolated values for the grid points where no overlap occurs. The multiple box method allows for high resolution in a small area of interest without a substantial increase in computation time or complexity of code.

2.2 Particle Simulations

Limited 2D particle simulations were used to test the validity of the initial 2D ideal MHD simulations. That the scale size of the smallest mini-magnetospheres approaches the ion gyroradius indicates that averaging over a gyroradius, as ideal MHD does, may give misleading results.

The particle simulations used a particle-in-a-cell code [76]. The Lorenz force equation takes the form

$$\frac{\partial \mathbf{v}}{\partial t} = \frac{q}{m} (\mathbf{E} + \mathbf{v} \times \mathbf{B}) \quad (2.13)$$

$$\frac{\partial \mathbf{r}}{\partial t} = \mathbf{v} \quad (2.14)$$

where \mathbf{v} and \mathbf{r} are the velocity and position of an individual particle, q and m are the particle charge and mass, and \mathbf{E} and \mathbf{B} are the electric and magnetic fields. The particle positions are accumulated on a grid to determine charge density and current density. The charge density is then used to solve Poisson's equation for the electric field. The current density and electric field are then used to solve Maxwell's equations for the magnetic field. All equations are solved in 2D spatially, but in 3D for velocity, magnetic field, electric field and current density. Thus plasma can only flow above and below the Moon, as it acts like an infinite cylinder. A more detailed discussion of the model can be found in *Winglee and Kellogg* [76].

2.3 Non-ideal MHD

The results from the 2D particle simulations indicate that non-ideal MHD behavior is important in the physics of mini-magnetospheres. *Winglee* [75] showed that when the Hall and pressure gradient terms are included in Ohm's Law for fluid simulations, the model can capture localized charge separation and non-ideal MHD behavior such as ion demagnetization.

Equations 2.1 - 2.4 remain the same but Ohm's Law, in dimensionless form, becomes

$$\mathbf{E} = -\mathbf{v} \times \mathbf{B} + \eta \mathbf{J} + \frac{c}{\omega_{pi} L \rho_m} (\mathbf{J} \times \mathbf{B} - \nabla P_e) \quad (2.15)$$

where \mathbf{E} is the electric field, \mathbf{B} is the magnetic field, \mathbf{J} is the current density, P_e is the electron pressure (and equal to half the total pressure, P), ρ_m is the density, η is resistivity, c is the speed of light, L is the scale size of the grid in the simulation, and ω_{pi} is the hydrogen ion plasma frequency. The ratio $\frac{c}{\omega_{pi}}$ is the ion inertial length. The resistivity (η) is set to zero outside of the Moon and the Hall and ∇P_e terms are only

evaluated outside of the Moon. For 2D simulations, the vector quantities are three component vectors, but the spatial derivatives are only taken in two dimensions.

The ratio $c/(\omega_{pi}L)$ is a measure of the strength of particle-like effects. The simulations can not be run with the ratio equal to the full value though, as it will cause instabilities. Thus the parameter must be tuned to the highest value for which the simulations remain stable. In the results shown in this thesis, the full value of $c/(\omega_{pi}L)$ is equal to 2.07, but was set to 0.10, with a value larger than 0.12 causing instability. The ratio was equal to 0.125 in the simulations run by *Winglee* [75].

2.4 Calculation of Magnetic Anomaly Source

In regions above the Lunar and Martian magnetic anomalies,

$$\nabla \times \mathbf{B} \sim 0 \quad (2.16)$$

since ionospheric currents are either negligible, in the case of the Moon, or produce magnetic fields small compared to the surface source, in the case of Mars. Equation 2.16 implies that

$$\mathbf{B} = -\nabla V \quad (2.17)$$

and

$$\nabla^2 V = 0 \quad (2.18)$$

where V is a scalar magnetic potential. A non-trivial solution to Equation 2.18 is sum of spherical harmonics.

The model for the real Martian magnetic field was created with a 90 term spherical harmonic expansion provide by *Cain et. al.* [5]. The data input for the model contained 110,000 3-component vector magnetic field observations, providing global coverage.

The magnitude of the anomalous fields at the Moon are small enough that magnetic field vector data above the surface (i.e. the location of Lunar Prospector) is limited and has large errors due to the small magnitude. Thus a spherical harmonic expansion of the total surface magnetic field is not available. Instead the anomalous regions are modeled with multiple dipoles. This also creates a model magnetic field with higher order moments.

Chapter 3

INITIAL 2D MHD LUNAR SIMULATIONS

Two dimensional magnetohydrodynamic simulations were run first to determine the possibility of creating mini-magnetospheres. 2D MHD simulations of the solar wind interaction with the magnetized regions on the surface of the Moon suggest “mini-magnetospheres” can form around the regions on the Moon when the magnetic anomaly field strength is above 10 nT at 100 km above the surface (for a surface field strength of 290 nT) and when the solar wind ion density is below 40 cm^{-3} , with typical observations placing anomalous magnetic field strengths around 2 nT at 100 km above the surface. The results suggest that not only can a bow shock and magnetopause form around the small anomalies, but their position and shape can change dramatically with changes in the solar wind conditions. A switch from southward to northward interplanetary magnetic field (IMF) causes the size of the mini-magnetosphere to increase by 90% and the magnetic field at various positions inside the bow shock to increase by a factor of 10. In addition to affecting the stand-off distance, changes in the IMF can also cause the mini-magnetosphere to go from very round to flat and elongated. The scale size of the mini-magnetospheres is 100 km for the range of typical solar wind conditions and the surface magnetic field strengths measured by Lunar Prospector. A stagnation point inside the shock region also exists for several solar wind conditions. Thus the 2D simulations for the Moon show that mini-magnetospheres can in fact form and that they are much more dynamical than planetary sized magnetospheres. But they also indicate that non-ideal MHD physics is needed to explain the behavior of mini-magnetospheres.

3.1 Initial Conditions

The 2D simulations solved Equations 2.1 - 2.6 with the momentum and magnetic field vectors constrained to have components only in the simulation plane, while the electric field and current had components only in and out of the simulation plane (Figure 3.1).

Three grids of 300 x 200 grid points were used with the spatial resolution equal to 34.8 km in the outer grid, 17.4 km in the middle grid and 8.7 km in the inner-most grid. C.P. Sonnet [68] placed the resistivity of the Lunar rock between 10^3 ohm · m and 10^5 ohm · m. The Lunar conductivity was set to 10^4 ohm · m. The numerical resistivity was approximately 0.15 ohm · m. For this simulations the magnetic Reynolds number was approximately 0.43 inside the Moon, while the Reynolds number associated with the numerical resistivity in the plasma was on the order of 56,000.

Simulations were run with the IMF set to 5 nT in the \hat{x} direction or 2.5 nT in the $-\hat{z}$ direction. At these field strengths, the IMF diffuses sufficiently fast through the Moon that there is no pile-up of IMF at the unmagnetized surface. For higher values, 3D effects need to be incorporated to allow flow of plasma and IMF around the flanks, and prevent an unphysical pile-up of IMF at the unmagnetized surface. Decreasing the conductivity of the Lunar surface increased the diffusion of the magnetic field through the surface, preventing pile-up of the IMF, as well as making the surface value more physical, but it also made the simulation unstable. MHD assumes infinity conductivity (zero resistivity) but can work for finite, but large conductivity. The conductivity of the Moon was set to the smallest value possible for which instability did not occur.

The average day-side ion density of the Lunar atmosphere was set at 10^{-1}cm^{-3} and the night-side density 10^{-2}cm^{-3} with an average molecular weight of 40 amu and scale height of about 100 kilometers [33, 27]. Ar^{40} constitutes the largest fraction of ions in the tenuous Lunar atmosphere, with only Neon becoming comparable during periods of extremely high solar flux. The model is a single species (proton) simulation, therefore the Lunar ionosphere had an effective number density of 4 ions/cm³ on the day side and 0.4 ions/cm³ on the night side. The ion temperature of the Lunar atmosphere is approximately 400K [33] with the temperature of the solar wind approximately $1.4 \times$

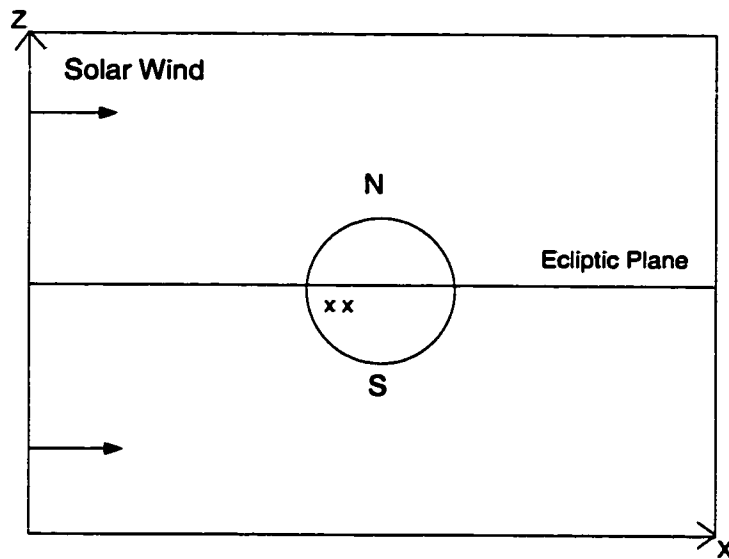


Figure 3.1: Key to Figures: All of the 2D and 2.5D plots follow this convention. The arrows on the left-hand side indicate the direction of the solar wind. The line in the center of the box indicates the location of the ecliptic plane, with the north and south poles of the object above and below the plane. The two small crosses inside the object indicate the approximate location of the line currents for a dipole field with the moment in the $\pm z$ direction. The vertical axis will be referred to as the z axis and the horizontal axis as the x axis.

10^5 K. Thus the Lunar ionosphere acts as a sink for particles in the unmagnetized regions. The results are independent of variation in the actual values, so long as the atmosphere acts as low pressure region. The pressure and density can not be set to zero though, as it would introduce division by zero into the numerical solutions.

Two line currents, oriented with opposing polarity, were used to create a dipole magnetic field at the equivalent of 25° S. The line currents, separated by 52.5 km, were placed in a plane parallel to the ecliptic plane, 26.1 and 78.3 km below the surface, producing a dipole-like field with its effective dipole moment vector pointing North or South (Figure 3.1). A tilted dipole was created by moving one or both of the line currents off of the ecliptic plane. The magnetic field from line currents were used because they have unequal magnetic field strengths at the pole and equator. A 2D dipole produces symmetric magnetic field strength. The magnitude of the magnetic field for a 3D dipole is dependent on latitude, but the 3D dipole formula can not be

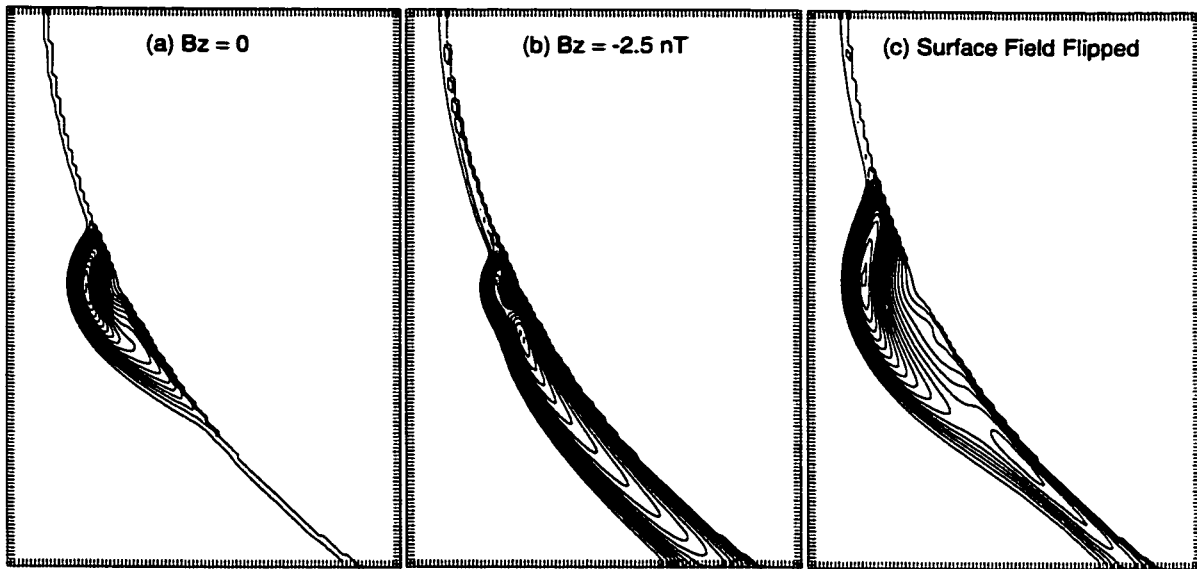


Figure 3.2: Pressure Contours for three different initial conditions with a dipole located at 25°S , measuring 30 nT at 100 km above the Lunar surface and 290 nT at the surface. The boxes correspond to a region 870.0 km by 1350.0 km , with the tick marks being units of 8.7 km . The solar wind is set to 10 ions/cm^3 with a speed of 400 km/s , and the surface pressure is held at a constant value of $5.5 \times 10^{-7}\text{ nPa}$. In case (a) the IMF is 5 nT parallel to the ecliptic plane with the surface field of the anomaly in the northward direction (dipole moment in $-\vec{z}$). The contour interval is 0.074 nPa . Case (b) and (c) are both for southward IMF of 2.5 nT . In case (b) the surface field points in the opposite direction as the IMF (dipole moment in $-\vec{z}$), whereas in case (c) the direction of the surface field was flipped to point in the same direction as the IMF, Southward (dipole moment in $+\vec{z}$). The contour intervals for (b) and (c) are 0.083 nPa and 0.089 nPa , respectively.

used with just one of the coordinates set to zero as that makes $\nabla \cdot \mathbf{B} \neq 0$. The strength of the field was set to 290 nT at the surface and the strength above the surface could be varied by the separation of the line currents. The maximum surface field was taken from the Lunar Prospector results since the large regions we are interested in would tend to average out the small pockets of much large field strength.

The initial conditions for each of the three cases focused on are listed in Figure 3.2. The orientation of the dipole moment, relative to the direction of the velocity of the solar wind, was also varied to determine its effect on the shape of the shock. The solar wind properties were initially set to a density of 10 protons/cm^3 , with an speed of 400

km/s in the \hat{x} direction.

3.2 Model Results

No large scale bow shock can be seen surrounding the entire Moon (Figure 3.2), as would be expected for a low density and low temperature object immersed in a hot solar wind. But a shock, or mini-magnetosphere can be seen around the magnetized region for several solar wind and anomaly configurations, three of which are shown in detail. In large scale magnetospheres, two distinct boundaries occur, the first being the bow shock where the supersonic solar wind is slowed to subsonic speeds and the second occurring at the magnetopause where the pressure balance occurs between the solar wind dynamic pressure and the object's magnetic pressure. At the Earth's magnetopause a large change in the density and pressure occurs. A bow shock can be seen for all the mini-magnetospheres in Figure 3.2, but the inner boundary is much more complicated.

The definition of a magnetopause in the mini-magnetosphere is much more difficult since the internal structure is so compressed. A strict definition of the boundary between open and closed field lines does not have any of the typical signatures. There are no large gradients in pressure and density in the vicinity of the magnetopause. Instead, the pressure and density gradients constitute nearly all of the mini-magnetosphere. Rather than having two signature currents, one at the bow shock and one at the magnetopause, the increase in the magnitude of the current is a single structure, although the sign of the current can change within that region. And within a region 10-20 km thick around the magnetopause, the pressure, density and temperature reach local maxima.

An expanded view of Case A is shown in Figure 3.3 where the solar wind has a density of 10 protons/cm³ and a speed of 400 km/s and an IMF of 5 nT in the ecliptic plane. The stand-off distance of the shock is approximately 130 km on the outer edge, above the orbital height of Lunar Prospector. On the horizontal plane through the dipole location, the pressure maximum occurs at approximately 79 km above the surface, and is 50 times the solar wind pressure, while the density reaches a maximum

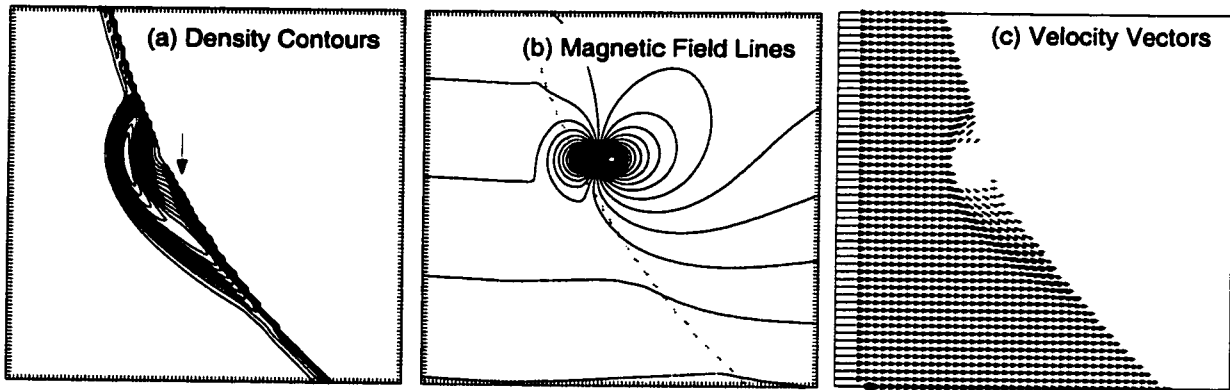


Figure 3.3: Case A: IMF in Ecliptic Plane. Magnified plots of density contours, magnetic field lines, and plasma flow for Case (a) in Figure 3.2. The IMF is 5 nT in the ecliptic plane. Each tick mark equals 8.7 km and the boxes contain a region 870 km by 870 km. The dotted line on the magnetic field line maps indicate the surface of the Moon. The contour interval for the density plot is 1.8 protons/cm³. In all density plots the surface is at an effective constant density of 4.0 protons/cm³ and the solar wind maintains a density of 10.0 protons/cm³.

of 3.6 times the solar wind density at the same position. This position is also where the magnetopause occurs, as it is a region of transition to closed field lines and a current is present.

For points above and below the horizontal plane through the location of the dipole, the maximum values of pressure, density and temperature decrease. The magnetic field at 100 km above the dipole is just under 30 nT. Thus it is less than what the surface field was set to initially at that position and indicates that the dipole field has been compressed. The solar wind plasma slows due to the presence of the surface magnetic field and is deflected around the anomaly. Some plasma flows toward the anomaly in two cusp-like regions that separate open and closed field lines just above the surface.

The pressure and density maximum values are below the expected range for a solar wind with the Mach number of 10. The Rankine-Hugoniot conditions for a finite Mach number in the upstream region state that the density increase across a shock is by a factor of 5.7 and the pressure increases by a factor of over 100 for γ (the ratio of specific heats) equal to 1.4 [56]. This assumes that the velocity normal to the shock inside the

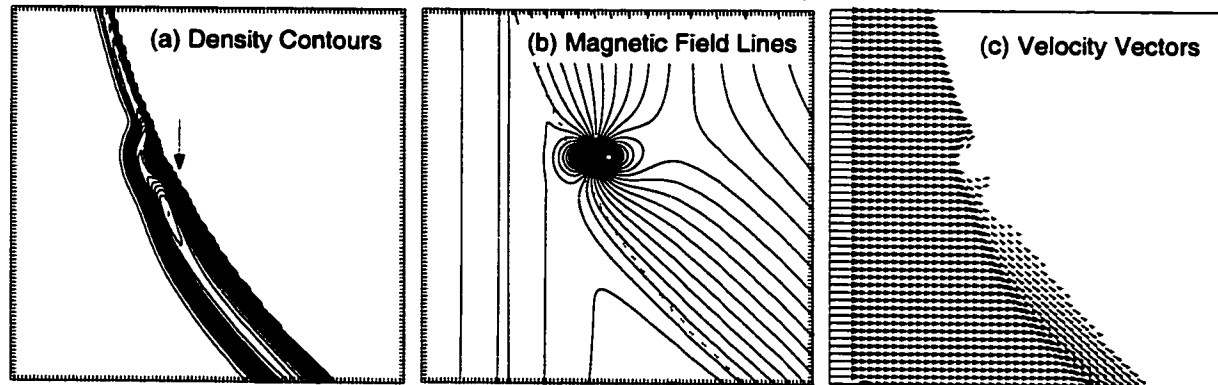


Figure 3.4: Case B: Southward IMF. All parameters the same as in Case A, except the IMF is 2.5 nT in the Southward direction. All figures plotted on the same scale as those in Figure 3.3. The contour interval for the density plot is 2.2 protons/cm^3 .

shock region is zero and in all the cases examined, the flow is essentially all tangential.

The Rankine-Hugoniot conditions are for perpendicular shocks that are detached from the object. An oblique shock has jumps in density and pressure across the shock that are lower than in a perpendicular shock. Also the close proximity of the shock to the cold surface of the Moon may cause the pressure increase to be smaller than expected for theory. For the cases analyzed, the maximum increase in density and pressure is correlated to the size of the shock, with larger jumps seen for larger shocks.

Case B (Figure 3.4) has southward IMF of 2.5 nT, and the same solar wind conditions and dipole field strength as above. The IMF and the dipole field at the surface of the Moon are in opposite directions, allowing for day-side reconnection to occur. A shock surface still forms around the magnetic anomaly, but the stand off distance is only just over 100 km above the surface. The shock surface is also not spherical, as in Case A; it is very elongated and has an indentation just below the plane containing the current elements that create the dipole. This indentation is in the same horizontal plane as a stagnation point. The elongation of the shock surface is due to the draping of the reconnected field lines, forming a mantle-like structure where the shocked plasma flows along the field lines around the Moon.

At the stagnation point, the pressure and density increase to their global maxima

but the temperature of the plasma does not. The maximum pressure and density occur approximately 150 km south of the dipole and 61 km above the surface, while the maximum in temperature occurs 44 km directly above the location of the dipole. At the stagnation point the density increases to 4.5 times the solar wind density and the pressure increases to just under 60 times the pressure of the solar wind. At the location of the maximum in temperature, the density only increase by a factor of 3 times the solar wind density, and the pressure by a factor of 40. As in Case A, these values are lower than predicted for a Mach number of 10.

The plasma being deflected down by a simple obstacle should just flow around the Moon. Instead, in the present case, it slows due to the reconnection of the IMF to the anomalous magnetic field, which forms kinked magnetic field lines. These kinked field lines appear to be causing the stagnation point, impeding the flow of plasma.

A substantial portion of the dipole field lines (Figure 3.4b) have reconnected to the IMF, eroding the surface field. As a result, the scale height of the magnetic field is seen to decrease such that the magnitude of the field at 100 km directly above the dipole is only 3 nT, with the magnetic field increasing to 30 nT at only 60 km above the surface, in the region around the dipole. The reconnected field lines allow an even more prominent flow of plasma into the cusp region for Case B, than occurred in Case A.

In Case C (Figure 3.5), the direction of the dipole moment of the anomalous field was flipped so that the field at the surface is in the same direction as the IMF. This is analogous to flipping the direction of the IMF to Northward in Case B (the magnitude of both the IMF and the dipole remained the same). The shock surface is much rounder and moves out to 190 km directly above the dipole. In the case of Earth's magnetosphere, when the IMF change from Southward to Northward, the sub-solar point moves out about $1 - 2R_E$, or about 10% its distance from the Earth. In the case of the mini-magnetosphere, the height of the bow shock above the Lunar surface changed by 90%.

A stagnation point below the dipole occurs in Case C also, but unlike Case B, the global maxima in pressure and density do not correspond to the location of the stag-

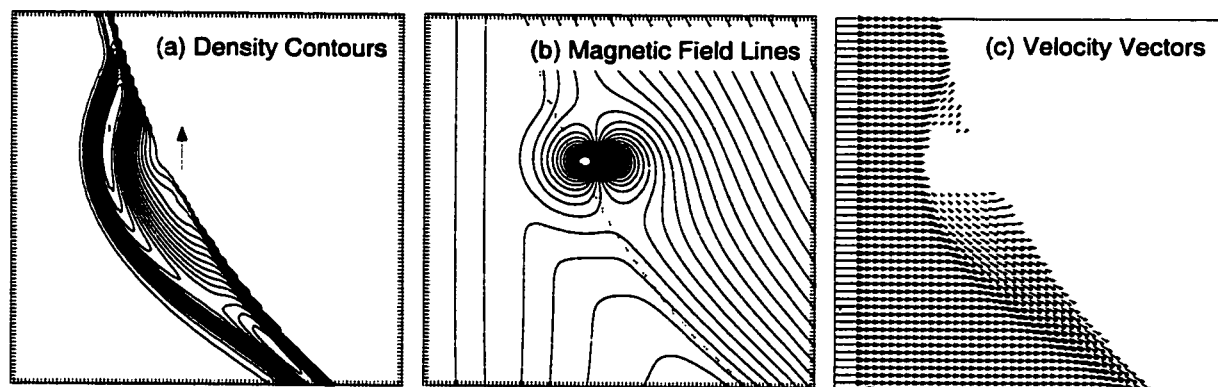


Figure 3.5: Case C: Northward IMF. All parameters the same as in Case B, except the dipole moment is flipped to the $+z$ direction, thus the field at the surface is in the same direction as the IMF. This is analogous to flipping the IMF from Southward to Northward, for the same surface field. All figures plotted on the same scale as those in Figure 3.3 and 3.4. The contour interval for the density plot is also 2.2 protons/cm^3 .

nation point. Rather they were at the same location as the maximum temperature and the magnetopause, directly above the dipole. The spherical shape is due to what looks similar to a closed magnetosphere configuration in the Earth's magnetosphere. The IMF drapes around the magnetic anomaly, with much less reconnection of the dipole field to the IMF than in Case B. The IMF piles up at the magnetopause, and the magnetic field line reconnection that does occur is in the interior of the Moon. As a result, the surface field is not nearly as eroded as it is in Case B. At 100 km above the dipole, the total magnetic field is approximately 50 nT, an order of magnitude increase from Case B. Even though the mini-magnetosphere looks closed, the plasma near the surface and below the dipole can still flow into the cusp.

The fall-off of the dipole field could be varied by changing the separation of the current elements generating the field. When the conditions in Case A were varied such that the dipole strength was equal to 150 nT at the surface and 30 nT at 100 km above the surface (all other parameters remaining the same), the stand-off distance of the shock moved out to approximately 200 km on the outer edge, an increase of about 50% from the size in Case A. The shape of the shock structure is the same as for Case A, the overall size just increases. The total magnetic field at 100 km above the

dipole is approximately 20 nT, indicating some compression or erosion has occurred. When the surface field strength was set to 290 nT at the surface and 10 nT at 100 km above the surface, the mini-magnetosphere nearly disappeared. A very small mini-magnetosphere formed, but the outer edge was only about 40 km above the surface.

When the ion density of the solar wind was decreased to $1/\text{cm}^3$, in Case A, the outer edge of the shock surface formed at 260 km above the surface, for an initial anomalous field of 30 nT at 100 km and 290 nT at the surface. This is a 100% increase over the height of the shock surface from when the density is $10/\text{cm}^3$ (all other parameters the same). For a low density solar wind, a stagnation point developed near the surface to the north of the anomalous region. Above the anomaly, the plasma is deflected into the inside surface shock, while below it is deflected down and around the Moon, and is not impeded by kinked field lines. A low density cavity also formed inside the shock region. The density reaches a maximum value of $4.5 \text{ ions}/\text{cm}^3$ at the magnetopause, and then decreases to approximately $2 \text{ ions}/\text{cm}^3$ in the region between the magnetopause and the surface of the Moon (which has an effective density of $4 \text{ ions}/\text{cm}^3$). A boundary in the pressure developed in the same location as well. This behavior is similar to that seen at the Earth's magnetopause.

The outer shock surface dropped to approximately 35 km above the surface and no inner surface was visible, when the solar wind ion density was increased to $40/\text{cm}^3$, for Case A with the surface field set to 150 nT and 30 nT at 100 km above the surface. When the velocity of the solar wind was decreased to 300 km/s, with the ion density remaining at $10/\text{cm}^3$, a stagnation point developed and the outer surface moved out to about 230 km, a 30% increase from the distance when the velocity of the solar wind plasma was 400 km/s.

When the conditions were the same as Case C, except the IMF has components equal to 2.5 nT in both the \vec{x} and $-\vec{z}$ directions, the mini-magnetosphere was nearly identical to the mini-magnetosphere in Case C. This is similar to the Earth's magnetosphere, which tends to be insensitive to changes in B_x . In the simulations, when B_x is increased from 0 to 2.5 nT, the only changes are in the configuration of the open field lines and the location of the stagnation point.

3.3 Discussion

The cases focused on show that mini-magnetospheres can form for typical solar wind conditions, and while similar to the Earth's magnetosphere there are substantial differences as well. The cases also highlight which parameters are the most important in determining the size and structure of a mini-magnetosphere. The direction and strength of the IMF has the single greatest effect on the structure of the mini-magnetosphere for fixed lunar magnetic fields. Simply changing the direction of the IMF from South to North has nearly as big an effect on the size of the mini-magnetosphere as increasing the dynamic pressure of the solar wind by a factor of four. But unlike increasing the dynamic pressure, flipping the direction of the IMF significantly changes the internal structure of the mini-magnetosphere as well. It caused the shock region to become very elongated, wrapping around the surface of the Moon.

But changing the direction of the IMF, respective to the effective dipole moment, only produced large changes in the shape of the mini-magnetosphere when there was a significant component of the surface field in the same direction as the IMF, and the fluid flow was perpendicular to the IMF and dipole moment. This can be seen by comparing the large differences in Case A and Case B (Figure 3.2). The dipole moment of the surface field and the direction of the IMF are perpendicular in Case A and parallel in Case B, resulting in mini-magnetospheres that have a significantly different size and structure. But when the angle between the dipole moment and the IMF rotated from perpendicular to anti-parallel (Case A to Case C), the size of the mini-magnetosphere increase but the shape remained about the same. And when the fluid flow, the IMF and the dipole moment were all parallel, the shape of the mini-magnetosphere was similar to those in Case A and Case C, with only the internal structure different. Varying the angle between the dipole moment vector and the IMF between 0 and 90° for IMF in the \vec{x} direction, did not cause the overall shape of the mini-magnetosphere to change dramatically, only the overall size and the location of the stagnation points inside the shock region changed. Thus the direction of the fluid flow relative to the IMF and surface field also contributes significantly to the shape of

the mini-magnetosphere.

Changes in the magnitude of the solar wind velocity and density effect the size of the mini-magnetosphere, but not nearly as dramatically as some changes in the IMF. Changing the surface field strength had the least effect on size and shape, while varying the magnitude of the field at 100 km, when the surface field remained fixed, had a large effect on the resulting size of the mini-magnetosphere.

The above cases also indicate that the density and pressure increases predicted by the Rankine-Hugoniot conditions are an extreme upper bound, and the relative increase in density and pressure across the bow shock correlates with the size of the mini-magnetosphere. The largest jumps are seen in Case C and for the conditions of Case A but with low solar wind density (1 ion/cm^3). The maximal increases in density and pressure are by a factor of about 4.5 and 65, respectively. The smallest increase is in Case B, which also has the smallest scale size. This suggests that the closer a mini-magnetosphere forms to the Lunar surface, the more the magnetospheric plasma can be absorbed by the surface, reducing the build-up of plasma. Thus the predicted values from the Rankine-Hugoniot conditions are never reached, even for stagnation points.

We can test the validity of the MHD results by looking at the the size of the proton gyroradius in the mini-magnetospheres. The proton gyroradius at 100 km above the surface varied between 5 and 25 km inside the shock of the mini-magnetosphere in Case C. In Case B (the smallest mini-magnetosphere), the proton gyroradius at half way between the surface of the Moon and the shock surface ranged between 25 and 75 km. This places the plasma scale size close to the size of the mini-magnetosphere in some regions inside and indicates that in Case B the MHD approximations are borderline in some regions.

Hood and Schubert [1980] showed that the charge separation that occurs at a magnetopause produces an electric field which reduces the necessary scale size for a magnetic anomaly to deflect the solar wind down to the geometric mean of the proton and electron gyroradii. For Case B, where the size of the proton gyroradius inside the mini-magnetosphere suggests the MHD approximation may be breaking down, the scale

size set by the geometric mean of the proton and electron gyroradii is $\sim 5 - 20$ km.

Hood and Schubert also showed that the length scale over which the magnetic field is nearly uniform is important for determining if a magnetic anomaly can deflect the solar wind. For a dipole-like field this scale length runs parallel to the dipole moment and is given by

$$L = B_z / \frac{\partial B_x}{\partial z} \quad (3.1)$$

for a dipole moment parallel to the z axis. For the solar wind conditions used in the simulation, with a field strength set to 290 nT at the surface and 30 nT at 100 km above the surface, $L \sim 176$ km. This size is significantly smaller than the lateral extent of the mini-magnetospheres presented above.

3.4 Characteristics of a Satellite Fly-by

Cuts can be taken through the data to mimic the trajectory of a satellite traveling at 100 km above the surface, just like Lunar Prospector (Figure 3.6). The maximum in density is encountered before the maximum in magnetic field. This is consistent with the measurements made by Lunar Prospector, where the increase in flux is seen before the increase in magnetic field. In the three cases detailed in Figures 3.2 - 3.5, the magnetic field begins to increase after the density. The simulations indicate that the contours of magnetic field magnitude follow the surface of the bow shock. This combined with the angle of the magnetic field lines suggests that the increase in magnetic field is due to both a combination of IMF pile-up and compression of the surface field. There is not a clear transition between the two cases as there is in the Earth's magnetosphere. The transition region between pure IMF and closed field lines is only between 35 km and 85 km wide, but it is approximately 35%-45% of the thickness of the mini-magnetosphere. In the Earth's magnetosphere the transition between open and closed field lines occurs primarily in the magnetosheath, which is over $2R_E$ wide at the subsolar point (for a review see [36]), but the thickness of the region constitutes only about 20% of the day-side magnetosphere.

During time interval when a shock region was reported over the Serenitatis an-

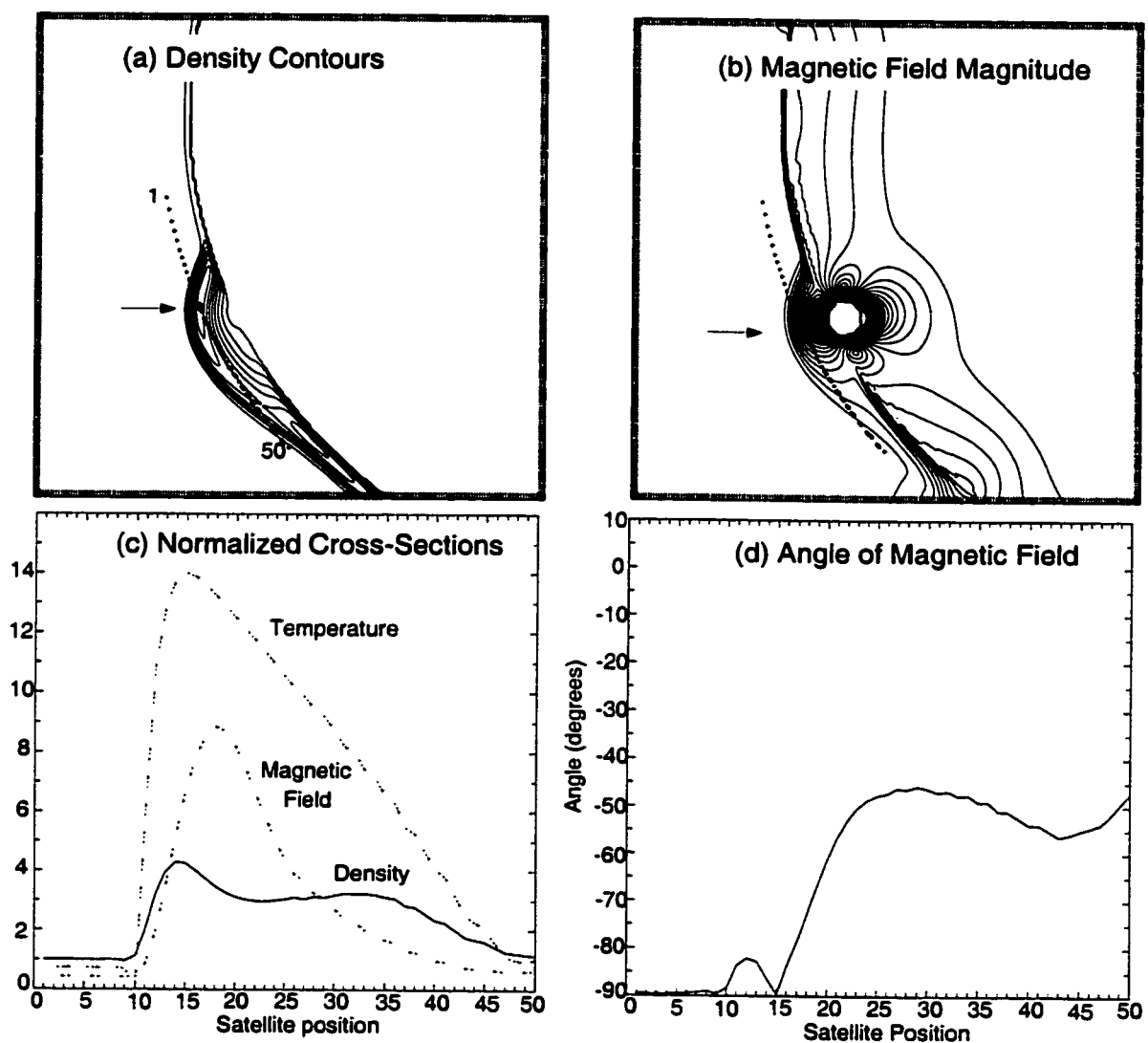


Figure 3.6: Cross-sectional cuts of density, temperature and magnetic field for a satellite orbiting at 100 km above the surface for the conditions in Case C. The spots on Figures (a)-(b) indicate the positions that the data was sampled to create Figures (c)-(d). The numbers on (a) indicate the satellite positions plotted in (c)-(d). The contour interval for the density is 4.6 protons/cm³, while the contour interval for the magnetic field is 6.1 nT, and both contain an area 1740 km by 1740 km, with the tick marks representing 8.7 km. The density, magnetic field magnitude, and temperature in (c) are all in normalized units. The solid curve is the density, the curve composed of two dashed lines is the magnitude of the magnetic field, and the curve made with three dashed lines is the temperature. The normalizing constant is 10 protons/cm³ for density, 5.79 nT for magnetic field, and 1.9×10^5 K for temperature. The angle of the magnetic field is measured relative to the ecliptic plane, with -90° being the Southward direction. The positions of the maxima in density and magnetic field in (c) are marked in (a) and (b) with horizontal arrows and an enlarged spot. The magnetic field (b) was zeroed at the center of the dipole region for plotting purposes.

tipode by LP [45], the solar wind ion density was approximately $10/\text{cm}^3$, while the solar wind speed slowly varied between 350 km/s and 400 km/s. During the pass when the dynamic pressure of the solar wind increased, the ion density increased to $40/\text{cm}^3$, while the average speed was just above 350 km/s. The simulations are consistent with the LP satellite, flying at an altitude near 100 km, first encountering the outer edge of a shock, where the pressure and density increase sharply, while the magnetic field increases more slowly. As the satellite approached a position directly above the magnetized region, it would have been traveling approximately tangential to the shock surface thus the pressure and density changed more slowly, while the magnitude of the magnetic field reached its maximum value. The pressure, density and magnetic field then all decreased as the satellite traveled back out of the shock surface. Symmetry of the measurements about the maximum will depend on the location of the anomaly. Since the shock surface over the Serenitatis antipode is asymmetric, measurements of flux and magnetic field would be as well. When the solar wind pressure increased to $40/\text{cm}^3$, as seen during the fourth orbit, the shock surface dropped so that only the outer edge would have been in the path of the satellite. Large scale reconnection of the anomalous magnetic field to the IMF is consistent with the Lunar Prospector measurement of only small rotations in the magnetic field in the regions of increased magnitude.

The results are not completely consistent with the magnetic field measured by LP though. Magnetometer measurements made above the Serenitatis antipode, when the anomalous region was in the wake and the Moon was in the solar wind vary between 2 and 15 nT at 100 km [Lin, *private communication* 1999]. These values are comparable to the IMF as measured by Wind, suggesting that the contribution due to the surface field is small compared to the IMF. For surface field strengths much less than 30 nT at 100 km, a shock would form in the simulations, but significantly closer than 100 km above the surface. Also, as LP traveled through the shock region, the increase in magnetic field was from 10 nT to 30 nT, not the factor of 9 increased predicted by our model.

Two possibilities could explain the discrepancies. The first is the the 2D nature

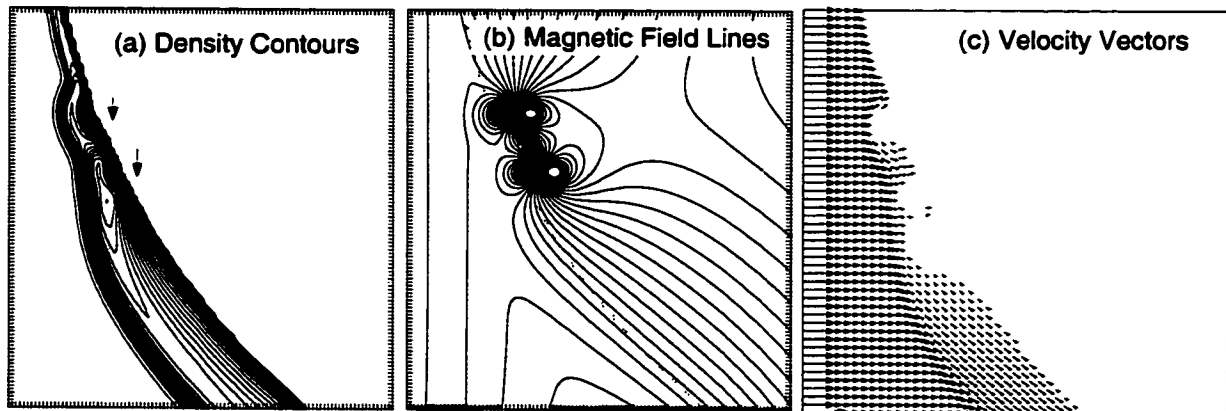


Figure 3.7: Two dipoles in anomalous region. All parameters are the same as in Case B (Figure 3.4), except the presence of a second identical dipole 5° above the original dipole. All figures plotted on the same scale as those in Figure 3.4. The contour interval for the density plot is 2.2 protons/cm^3 .

of the simulations. The cumulative effects of the crustal magnetic fields in the entire Serenitatis antipode most likely can not be accurately modeled with a simple dipole. The magnetized regions extend over hundreds of kilometers on a spherical surface, with plasma processes occurring relatively close to the source of the magnetic field. When a second dipole was added in the Case B described above (Figure 3.4), the height of the shock surface downstream of the anomalies moved out from 100 km above the surface to 190 km (Figure 3.7). This suggests that higher order moments and lateral structure play an important role in the scale size of the resulting mini-magnetosphere.

Chapter 4

2.5D PARTICLE AND MPD SIMULATIONS

The 2D MHD simulations of the solar wind interaction with the Lunar magnetic anomalies in Chapter 3 (and [25]) agreed with the analysis that LP encountered a “mini-magneto sphere” (a small scale magnetosphere) over the magnetic anomaly in the Serenitatis antipode. A mini-magnetosphere would form in the MHD simulations when the field strength of the magnetic anomaly was 290 nT at the surface and greater than 10 nT at 100 km above the surface, for solar wind velocity and density equal to 400 km/s and $10/\text{cm}^3$, respectively. The results also indicated that mini-magnetospheres are much more dynamic than planetary sized magnetospheres. Simply flipping the direction of the IMF caused the mini-magnetosphere to inflate and completely change shape. The distance between the outer shock surface and the surface increased from 100 km to 190 km, and the shock surface went from elongated along the Lunar surface to round with a smaller lateral extent. One limitation of the model was that the strength of the magnetic field at 100 km above the surface needed to be an order of magnitude larger than observed values in order for mini-magnetospheres to form at satellite altitudes.

The largest mini-magnetospheres that formed in the MHD simulations, with a scale size near 200 km, contained internal structures larger than a proton gyroradius. But the smallest mini-magnetospheres had a scale size smaller than 100 km and the size of the proton gyroradius became comparable to the size of the internal structure. This suggests that the smallest mini-magnetospheres in the simulations approached the limit where ideal MHD breaks down and particle simulations should be employed to help predict the behavior of the plasma inside the bow shock. It also indicates the need for an extended MHD model that incorporate small scale and non-ideal MHD effects into the fluid model.

This chapter presents the results from 2.5D particle and MPD simulations of the solar wind interacting with a magnetic anomaly on the surface of the Moon. The 2.5D particle simulations are used to verify that mini-magnetospheres will form around magnetic anomalies, and investigate the particle nature of the resulting mini-magnetospheres. The 2.5D MPD simulations investigate the changes in the characteristic quantities of the mini-magnetospheres when small scale, non-ideal MHD effects are incorporated into the fluid model. The results from both models can then be compared to look for similarities and differences.

2.5D particle simulations of the solar wind interaction with the magnetized regions on the surface of the Moon confirm the earlier 2D MHD result that mini-magnetospheres can form around the magnetic anomalies. A dipole buried 100 km below the surface with a field strength equal to 50 nT at the surface and 10 nT at 100 km above the surface held the solar wind off of the surface and caused a bow shock and a magnetopause to form. But the boundary separating the bow shock and magnetopause becomes ambiguous as the two structures merge due to the small scale size of the mini-magnetospheres. Acceleration of solar wind particles occurs at the shock. Inside the magnetopause, the Lunar electrons remained highly magnetized and exhibited fluid-like behavior. The Lunar ions, on the other hand, become demagnetized. Outside of the magnetopause, the solar wind ions and electrons exhibited fluid-like behavior.

Small scale and non-ideal MHD effects can be included into fluid simulations by adding Hall and pressure gradient terms in Ohm's Law, creating a magnetoplasma dynamics (MPD) model. The small scale effects allow for field-aligned currents and electric fields which look qualitatively similar to those in the particle simulations, but do not appear to change the overall shape of the mini-magnetosphere. The extra components of the electric field indicate the presence of charge separation at the shock surface, due to the momentum difference between ions and electrons, and the near the Lunar surface, due to non-ideal MHD behavior inside the mini-magnetosphere. The 2.5D MPD model can replicate the ion demagnetization seen in the 2.5D particle simulations.

4.1 Lunar Particle Simulations

Hood and Williams (1989) estimated the deflection of the solar ions wind by small anomalous regions (100-200 km in diameter) with surface field strengths greater than 1000 nT by following the trajectories of single particles. They then combined the results from an array of single particle trajectories to estimate how much the surface flux would be reduced by the presence of the magnetic anomalies. They modeled the anomalous regions with 9-15 buried dipoles that produced a total magnetic field strength of approximately 2 nT at 100 km above the surface. *Hood and Williams* [29] found significant deflection of the particles for surface field strengths greater than 1000 nT and almost no deflection for surface field strengths less than 800 nT. Their approach had the advantage that it was 3D. The disadvantage to their approach though was that it could not take collective effects into account and therefore was not a self-consistent, particle simulation. It could not predict the presence of shocks, heating or modification of the surface magnetic field.

To fully simulate the particle behavior near the magnetic anomalies, a multi-particle simulation must be done. Self-consistent particle simulations predict the paths of many particles as they interact with each other and the electric and magnetic fields. The particle interactions can also modify existing magnetic and electric fields, as charge and current densities evolve. The resolution of particle simulations though tends to be coarser than for fluid simulations due to the computationally intensive nature of the simulations and the smoothing needed to reduce noise.

4.1.1 Model Parameters

The particle simulations used a particle-in-a-cell code [76] to solve Equations 2.13 and 2.14. Short scale-length electrostatic quantities were solved on a 576×288 grid, with longer-wavelength electromagnetic quantities solved on a grid with half the resolution. The resolution of the simulation is such that the solar wind electron Debye length is equal to half a grid unit. The grid space separation was equal to 11.6 km for quantities solved in the finest resolution, but most data were smoothed to remove the effects of

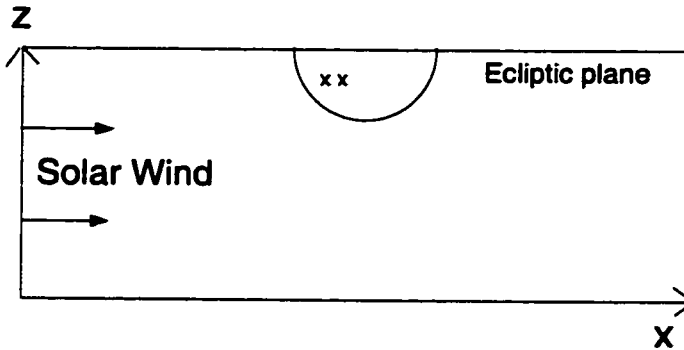


Figure 4.1: Key to Figures: All of the plots for the particle simulations follow this convention. The arrows on the left hand side indicate the direction of the solar wind. Symmetry about the ecliptic plane is assumed. The two small “x”s inside the object indicate the approximate location of the line currents for a dipole field with the moment in the $+z$ direction. The vertical axis will be referred to as the z axis and the horizontal axis as the x axis. The plots for the 2.5D MPD simulations look similar but symmetry about the ecliptic plane is not assumed.

noise before analysis, thereby reducing the resolution. The time step throughout the simulation is equal to $\frac{1}{8}$ of the electron plasma period. The largest frequency considered is on the order of or smaller than the plasma frequency.

The boundary conditions were assumed to be periodic at the top and bottom of the simulation box, with symmetry about the ecliptic plane (Figure 4.1). In the present case the direction away from the Sun is in the x direction and z is perpendicular to the ecliptic plane. The velocity in and out of the simulation plane (\vec{y}) is initially assumed to be zero. The magnetic field out of the simulations plane (\vec{B}_y) is the induced magnetic field created by currents in the simulation plane.

350,000 multi-charged particles were used to represent four distinct particle populations: solar wind ions and electrons, and Lunar ions and electrons. The solar wind was assumed to be composed of an equal number of electrons and H^+ ions, with a solar wind ion to electron mass ratio that was held constant at 64 for all simulations. The solar wind is continuously injected from the left hand side of the box with a number density of 6 particles cm^{-3} . The simulation must be halted before the solar wind reaches the right hand side boundary to prevent reflection effects.

The Lunar ionosphere consisted of an equal number of electrons and ions, where the ion species was varied. The Lunar ion to electron mass ratio was set to 64, 256 or 1024, approximating a surface ion species composed of H^+ , Ne^+ , or Ar^+ ions, respectively. In order for the simulation to run in a feasible amount of time, the real ion to electron mass ratios can not be used. In order to gain sufficient number statistics at the low Lunar number density, the mass of the Lunar ions and electrons relative to the solar wind mass, not the number density, was decreased. The solar wind electron to Lunar electron mass ratio was held constant at 70 for all simulations, while the solar wind ion to Lunar ion mass ratio varied between 4.4 and 70.

Argon constitutes the largest fraction of ions in the tenuous Lunar atmosphere, with Neon becoming comparable only during periods of extremely high solar flux [33, 27]. The average day-side ion density of the Lunar atmosphere is $10^{-1}cm^{-3}$ and a night-side density $10^{-2}cm^{-3}$ with a scale height of about 100 kilometers [*ibid*].

The IMF is set to zero for numerical simplicity. In order to evaluate the influence of the ion gyroradius on forming a mini-magnetosphere, the initial bulk speed of the solar wind was varied between 165 km/s and 1622 km/s, translating to a variation in the gyroradius between 23 km and 255 km. The thermal speed of the solar wind is small compared to the bulk speed and corresponds to a temperature range of 2.22 eV and 220 eV. The Lunar particles were initialized with no bulk speed and a thermal speed equal to a range of temperatures between 0.02 eV and 1.7 eV. The measured temperatures are less than 100 eV for electrons and less than 50 eV for ions in the solar wind [56] and 0.04 eV in the Lunar atmosphere [33].

The magnetic anomaly is modeled with a dipole buried approximately 100 km below the surface. The dipole is created using opposing current elements. The current elements are buried at such a large distance from the surface to ensure full grid resolution. To compensate, the magnetic field strength was reduced. The variation of the solar wind ion gyroradius results in a variation of the surface magnetic field strength between approximately 15 nT (for the fastest solar wind bulk speed) and 200 nT (for the slowest solar wind). For the baseline case of the solar wind bulk speed equal to 400 km/s, the magnetic field strength at the Lunar surface is approximately 50 nT and 10

nT at 100 km above the surface. After smoothing the density, the resolution becomes 104.4 km, comparable to the depth of the dipole. But at this time, it is difficult to go to finer resolution.

4.1.2 Particle Simulation Results

The particle simulations show that the magnetic anomalies can produce significant deflection of the solar wind for anomalous magnetic field measuring 50 nT at the surface and 10 nT at 100 km altitude, when the solar wind had a number density of approximately 6 cm^{-3} and bulk velocity of 400 km/s (Figure 4.2). The Lunar ion to electron mass ratio is equal to 1024, while the solar wind ion to Lunar ion mass ratio is equal to 4.375. The temperature of the Lunar ions and electrons is 0.02 eV, while the initial temperature of the solar wind ions and electrons is 2.22 eV.

The surface magnetic field is compressed by the solar wind but can still hold the solar wind particles off the surface, creating a boundary that resembles both a bow shock and a magnetopause. The inner edge of this surface forms 160 km above the surface (when measured radially from the surface) (Figures 4.2a and 4.2b), and forms a boundary that the solar wind does not cross. This boundary can be clearly seen as a bubble-like feature in the density plots for the solar wind ion and electron populations. Since there is a region where no solar wind particles cross into, the location of the magnetopause is not as ambiguous as in the MHD results. If the magnetopause is defined as the boundary where the solar wind is held off the surface by the anomalous magnetic field, the magnetopause forms at the inner edge of this shock surface. The solar wind ion population penetrates between 12 and 40 km further into the mini-magnetosphere than the electrons, at a variety of positions along the magnetopause. This boundary is also shock-like in that the solar wind electron and ion densities increase by a factor of approximately 3 to 5, as well as being a location of particle acceleration and heating.

The Lunar electrons form two high density regions, one directly above the surface magnetic anomaly, where the magnetic field is the strongest, and one in the downstream region where the anomalous magnetic field is approximately tangential to the surface (Figure 4.2c). Both regions of enhanced Lunar electron density correspond to

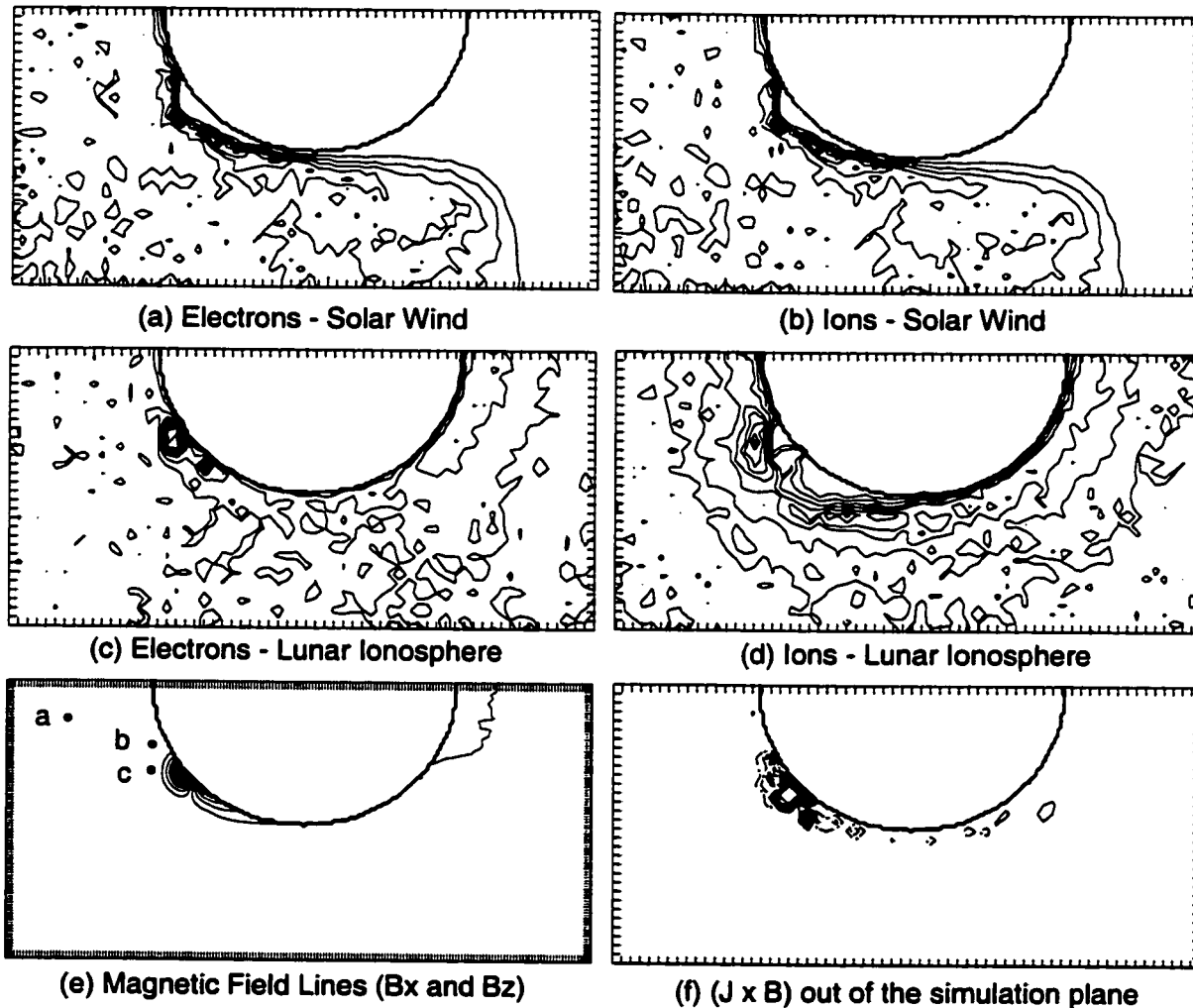


Figure 4.2: 2.5D particle simulations : nominal case: Smoothed density and magnetic field results from particle simulations. Plots (a) - (d) are the density contours for the four particle different populations. Plot (e) is the magnetic field lines for the components in the simulation plane and (f) the Hall component of the electric field in and out of the simulation plane. The contour interval in (a) is $1.1 \text{ electrons cm}^{-3}$, 1.1 ions cm^{-3} in (b), $0.05 \text{ electrons cm}^{-3}$ in (c), and $0.02 \text{ ions cm}^{-3}$ in (d). All densities are zero in the center of the Moon. The tick marks on the axes of the density plots equal 104.4 km (and 9 grid points) while the tick marks on the axes of the magnetic field line plot are 34.8 km apart. The three spots, and labels, in (e) refer to positions discussed in Figure 4.6. The thick curve in all the plots indicates the surface.

density voids in the Lunar ion population (Figure 4.2d). The region that separates the two enhanced Lunar electron density populations is aligned with a weak density enhancement of Lunar ions. This region of enhanced ions and depleted electrons is near the cusp but not totally aligned with it. A larger density enhancement in the Lunar ion population forms just outside the solar wind shock surface at the sub-solar point. Thus the Lunar particles, unlike the solar wind particles, do cross the shock region. The peak of the density enhancement in the Lunar electrons, above the anomaly, occurs in the middle of the solar wind shock surface. And the outer edge of the corresponding Lunar ion density void, coincides with the outer edge of the solar wind shock surface.

That the enhanced Lunar electron densities correspond to regions of high magnetic field indicates the electrons are frozen to the field and act like a fluid. And the fact that the ions, on the other hand, have density voids in regions of high magnetic field suggests that the Lunar ions become demagnetized and cease acting like a fluid.

One question to ask is why the ions leave the mini-magnetosphere when they become demagnetized and why aren't they pulled back by Coulomb force from electrons? Space charge fields develop as the solar wind ions and electrons meet the magnetopause. The Lunar ions and electrons respond to this electric field and are able to cross the magnetopause. But the movement of the Lunar electrons across the magnetopause is inhibited by the fact that they are frozen to the magnetic field. The solar wind ions, being the major charge carriers, in addition to having only a small velocity component perpendicular to the magnetic field, must maintain neutrality. Lunar ions and electrons try to short out the electric field and therefore are dragged about but their low density means the electric field is never eliminated.

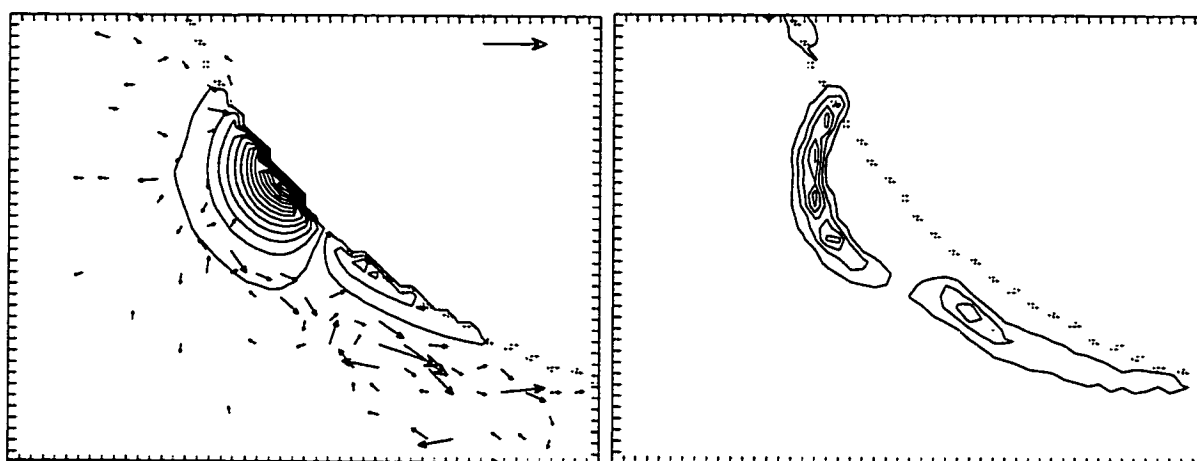
Signatures of a magnetopause are modified from those seen at the Earth. Instead of two separate density gradients being present at the bow shock and the magnetopause, the density enhancement in each population is a single structure. And instead of the maximum solar wind density being outside of the maximum magnetospheric density, the maximum in Lunar ion density, at the sub-solar point, is outside of the enhanced solar wind density and the maximum in the Lunar electron density is in the middle

of the solar wind shock. The small size of the mini-magnetosphere leads to a merging of boundaries. Clear separation of the bow shock and magnetopause do not exist as it does in large scale magnetospheres.

The high density region in the downstream Lunar electrons is reminiscent of the stagnation points seen in the previous MHD simulations (locations of high pressure and density but decreased temperature and velocity). The average Lunar electron number density directly above the anomaly is about a factor of 4.5 larger than the value in the solar wind but 6.5 larger in the stagnation region. At the stagnation point the kinetic energy of the electrons is about half the value in the enhanced region directly above the anomaly.

Even at the stagnation point, the mass density of the Lunar electron population is still two orders of magnitude smaller than the solar wind mass density in the shock surface and more than an order of magnitude smaller than the free streaming solar wind density. The velocity of the Lunar electrons is also 1-2 orders of magnitude smaller than the solar wind velocity. Thus the dynamic pressure of the Lunar electrons is small compared to the dynamic pressure of the solar wind. Inside the mini-magnetosphere, cavities with no Lunar ions form. And the density enhancements in the Lunar ion population only occur outside of the shock surface, both leading to similarly small Lunar ion dynamic pressures inside the shock. Thus the anomalous magnetic field is the only mechanism that can be responsible for holding the solar wind off the surface.

In the Earth's magnetosphere, two distinct current systems occur at the bow shock and magnetopause. In the mini-magnetosphere only one current system occurs inside the bow shock (Figure 4.3), but with no IMF, a bow shock current system would not form for any sort of magnetosphere. At the magnetopause current system, the maximum dawn-dusk electron current (J_y^e) forms 10-20 km outside of the maximum ion current (J_y^i). The peak ion current is deeper inside the magnetosphere than the peak electron current, as would be expected due to momentum differences and is seen in the Chapman-Ferraro currents at the Earth's magnetopause. The maxima in the dawn-dusk current forms at the boundary between the region of enhanced Lunar ion density



(a) Total Current in Simulation Plane (b) Total Current out of Simulation Plane

Figure 4.3: Total Current: Plots of (a) the flow of the total current in the simulation plane (J_x and J_z), with the magnetic field lines and (b) the magnitude of the total current in and out of the simulation plane (J_y^e) for the simulation presented in Figure 4.2. The arrow in the upper right hand corner of (a) corresponds to approximately 4000 nA/m² and the contour interval in (b) is approximately 8400 nA/m². The tick marks are 34.8 km and the plot contains an area 1740 km by 1392 km. The dotted curve indicates the surface of the Moon.

and the enhanced solar wind density surface.

Both ion and electron currents are closed by a current system downstream, above the stagnation point. The maximum density in the stagnation point of the Lunar electrons is about 80 km above the surface, with the peak in the associated current system about 150 km off the surface.

In the Earth's magnetosphere, the solar wind particles can be accelerated in the bow shock, but the majority of the flow is diverted around the flanks and heated in the magnetosheath, with the highest temperatures occurring at the subsolar point. In the mini-magnetosphere, boundaries are merged, and heating and acceleration regions form at both the subsolar point and in the downstream flank. Acceleration is seen as an increase in the bulk velocity (Figure 4.4 and Figure 4.5), whereas heating appears as spreading of the velocity distribution functions (Figure 4.6).

The heating and acceleration at the shock surface, directly above the anomaly at the subsolar point, is most prominent in the solar electron particle population. The

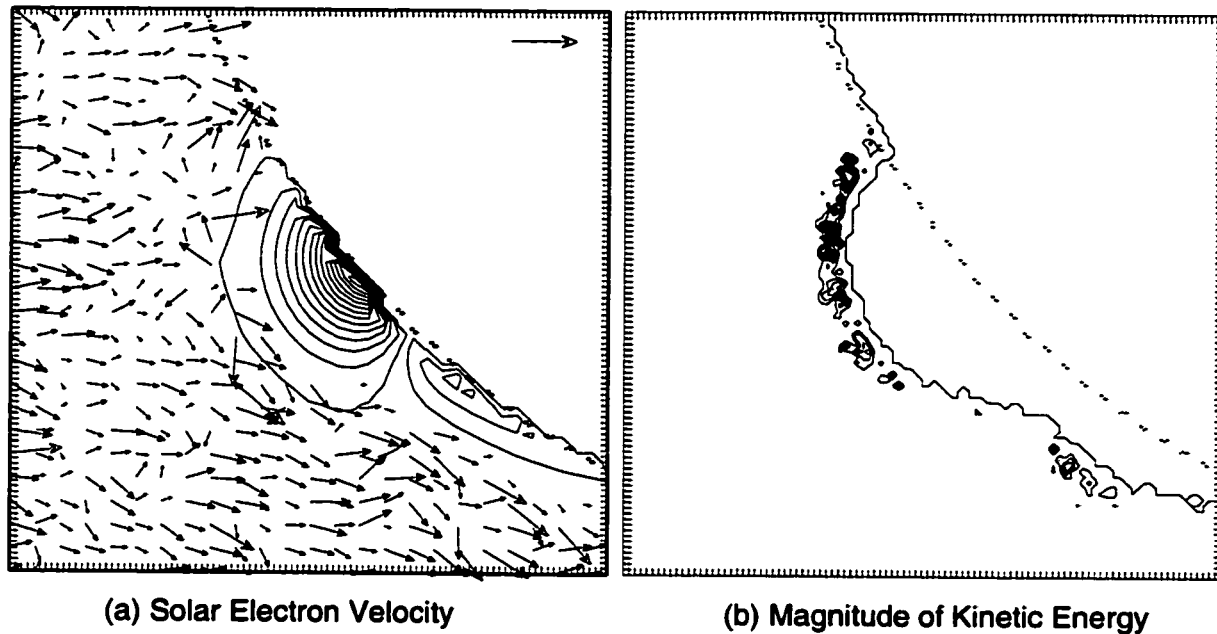


Figure 4.4: Electron Kinetic Energy and Velocity The velocity vectors for the bulk flow (a) and the magnitude of the the kinetic energy density (b) for the solar wind electrons for the simulation in Figure 4.2. The arrow in the upper right corner of (a) indicates a velocity vector with a magnitude of 1075 km/s. The contour interval in (b) is $2.25 \times 10^{-10} \text{Nm}^{-3}$ with the kinetic energy density in the Moon equal to zero. The tick marks on the axes equal 11.6 km in both plots and the boxes contain an area 1160 km by 1160 km. A dotted curve indicates the surface of the Moon.

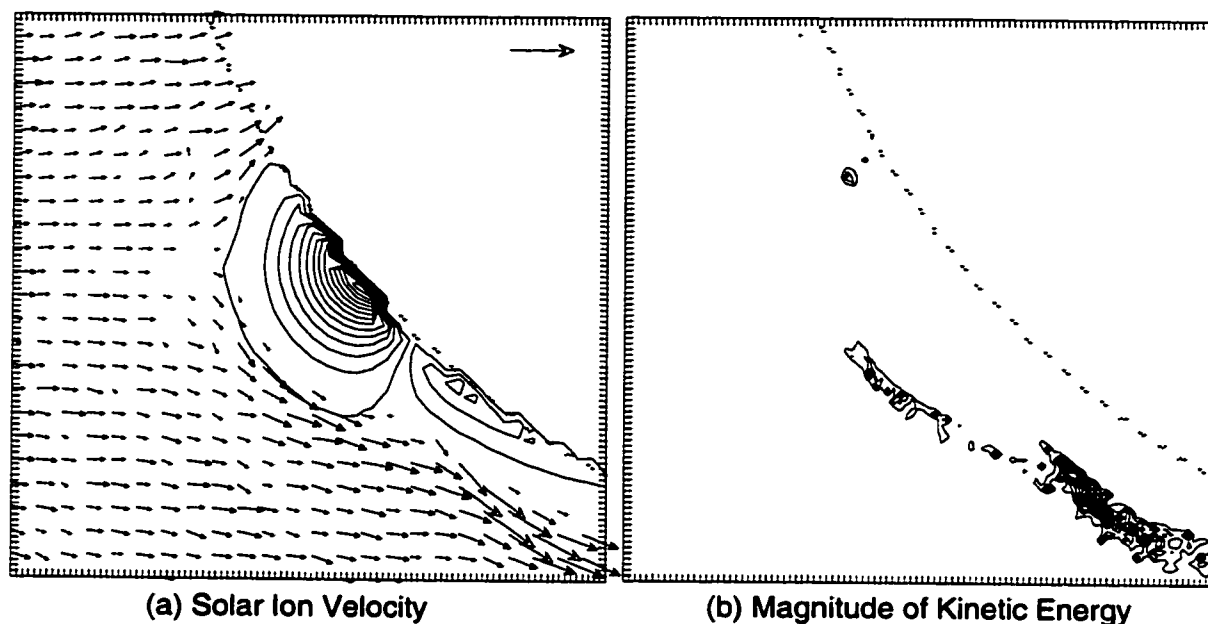


Figure 4.5: Ion Kinetic Energy and Velocity: The figure is of the same form as Figure 4.4 but for solar wind ions. The arrow in the upper right hand corner of (a) has a magnitude of 1231 km/s. The contour interval in (b) is equal to $5.0 \times 10^{-9} \text{Nm}^{-3}$.

kinetic energy of the solar electrons (Figure 4.4) increases by a factor of between 90 to over 200 times the value in the upstream solar wind, while the density increase by only a factor of 4 to 5. The acceleration and heating of solar ions occurs primarily in the downstream region, just above the stagnation point (Figure 4.5). In the downstream region the kinetic energy of the solar wind ions increases by a more than an order of magnitude, while the density increase by a factor of 3 to 5. The solar wind electrons are also moderately heated and accelerated in the the same downstream region as the ions, only further above the surface. The acceleration of the solar wind along the shock surface is not only seen in the increase in the bulk velocity, but also in the presence of both a solar wind ion and electron population traveling upstream.

The largest charge separation of the solar wind at the magnetopause occurs in the downstream region and is due to the electric field generated by the Lunar population. Near the surface there is a net negative charge due to the enhanced Lunar electron density and the density void in the Lunar ions. This electric field draws the solar ions

in further at the shock and repels the solar electrons slightly. The largest charge imbalance occurs at the stagnation point. This is an additional source of acceleration for the solar wind ions at the shock surface as well as separating charge more effectively than the momentum difference at the subsolar point.

The total electron distributions show that the bulk flow in the upstream region is slowed while the plasma is heated (Figure 4.6). Figure 4.6a is the 2D cuts of the electron velocity distribution near the edge of the simulation box, where the solar wind enters and is labeled as (a) in Figure 4.2e. Figure 4.6b is the velocity distributions from a position 83 km from the surface, and in front of the mini-magnetosphere, parallel to the the top edge of the mini-magnetosphere, where the shock attaches to the the Lunar surface. Figure 4.6c is from a point 248 km from the surface, at the outer edge of the solar wind shock surface and directly opposite the dipole. These points are labeled as (b) and (c), respectively, in Figure 4.2e. Each distribution is for the sum of electrons in a box 580 km (in x) by 348 km (in z) centered about the positions indicated in Figure 4.2e.

The distribution functions well in front of the mini-magnetosphere (Figure 4.6a) show an electron population with very little velocity in and out of the simulation plane, and a near Maxwellian distribution with the mean velocity in the simulation plane equal to 400 km/s. The narrow spread of the velocity out of the simulation plane at position (a) is due to the predominate presence of injected solar wind electrons. The solar wind particles are initialized with no velocity out of the simulation plane. The tail in the $-v_x$ direction indicates that the plasma is not completely undisturbed solar wind though, and includes a particle population traveling back upstream. Closer to the mini-magnetosphere, the velocity distributions show significant modification. Not only does the peak of the distributions in the simulation plane decrease to slightly less than 400 km/s in the upper Figure 4.6b and 200 km/s in the upper Figure 4.6c, the distributions become much broader, indicating heating of the plasma has occurred.

We can estimate the thermal speed in each direction by determining where the value of the distribution function has fallen to e^{-1} of the peak value. For the distributions in the simulation plane (upper Figures 4.6a - 4.6c), the thermal velocity in the z

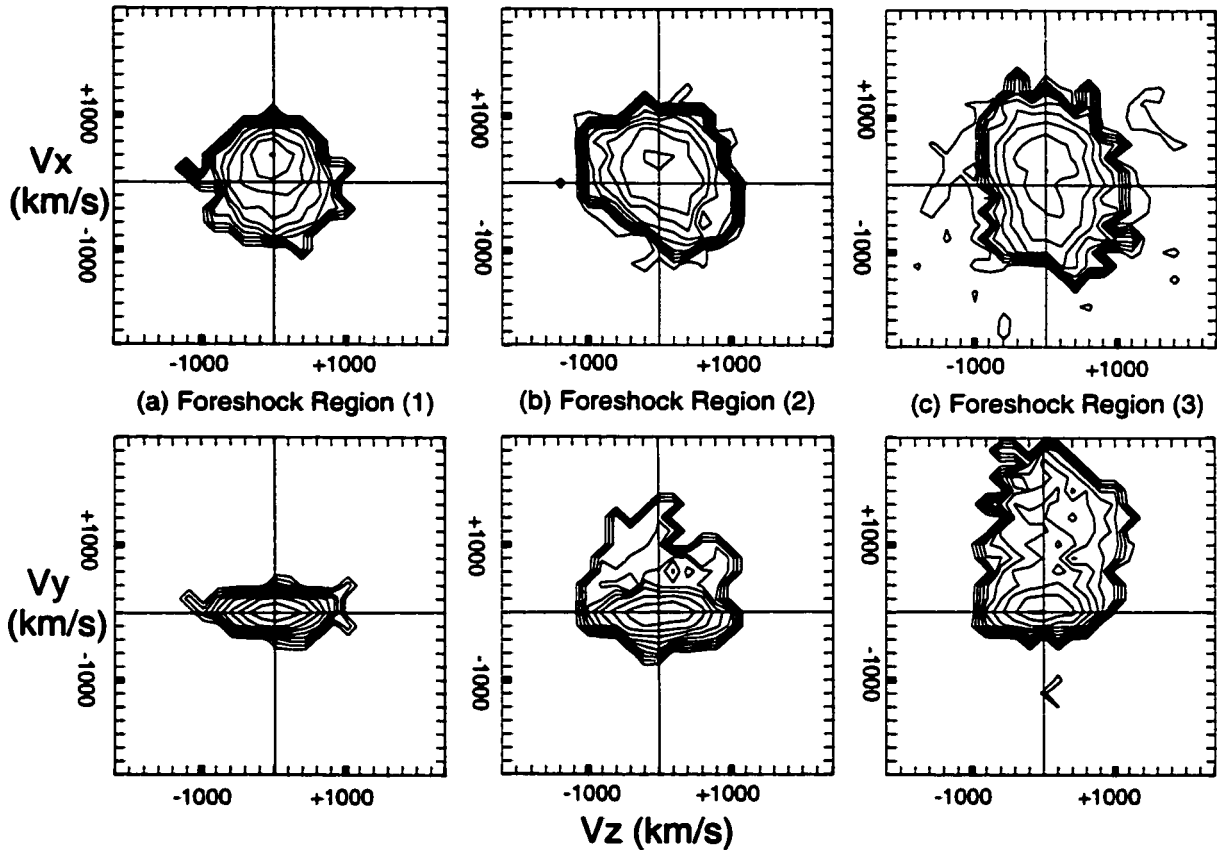


Figure 4.6: Velocity Distributions: The total electron velocity distributions for three regions outside of the mini-magnetosphere in Figure 4.2. Each distribution is for the sum of electrons in a box 580 km (in x) by 348 km (in z) centered about the positions indicated with a spot and a label in Figure 4.2e. Figure (a) is in the foreshock region, near the edge of the simulation box. The distribution in (b) is from a region approximately 83 km from the surface, in front of the upper edge of the shock region where the shock connects to the Moon just above the anomaly. Figure (c) is the distribution from approximately 248 km from the surface, in front of the shock region and directly opposite the anomalous region. The upper plots are the velocities in the simulation plane (v_x and v_z) and the lower plots contain the velocity out of the simulation plane (v_y and v_z). The tick marks on the axes equal 200 km/s, and the cross hairs indicate zero.

direction is between 400 - 500 km/s for all three regions. The thermal velocity in the x direction increase from about 200 km/s in the foreshock region 1, to 400 km/s in region 2, and 600 km/s in region 3.

The particle distributions containing the component of the velocity out of the plane (lower Figure 4.6b and c) show the electrons in the foreshock regions 2 and 3 acquire a velocity in the $+y$ direction. This is primarily due to the solar wind electron population. Position vs. velocity plots show that the solar wind electrons are anisotropically heated in the $+y$ direction in the upper half of the shock region and in the $-y$ direction in the lower half of the shock region.

The ion particle distributions show much less modification. The solar wind ions dominate the distributions with a mean velocity of 400 km/s and a thermal velocity on the order of 10 km/s. The ions acquire only a small velocity out of the simulation plane and velocity distribution does not show the same asymmetry that the electron population exhibits near the shock surface (lower Figure 4.6c).

The only modification in the ion distribution comes in the form of a secondary population. At position (a), the distribution shows a separate population traveling upstream with a velocity of about 250 km/s in the $-x$ direction and 150 km/s in the $+z$ direction, and a thermal velocity of approximately 70 km/s. The ion distribution at (b) is similar with a population traveling upstream with the same velocity in x , but about 250 km/s in the $+z$ direction. And the secondary population is warmer with a thermal velocity on the order of 100 km/s. At (c) the mean velocity of the secondary population in the z direction is zero, while the peak in the velocity distribution in x spreads between 200 and 400 km/s, with a thermal velocity on the order of 200 km/s. These results are all consistent with a plasma being heated at a shock and a portion of the population reflected back upstream.

When the bulk velocity of the solar wind was decreased by 58%, the size of the mini-magnetosphere nearly doubles (Figure 4.7). The initial thermal velocities in Figure 4.7 and Figure 4.2 are identical, but the bulk velocity of the solar wind was decreased from 400 km/s in Figure 4.2 to 165 km/s in Figure 4.7, translating to an increase in the surface magnetic field strength to approximately 200 nT. All other quantities, such

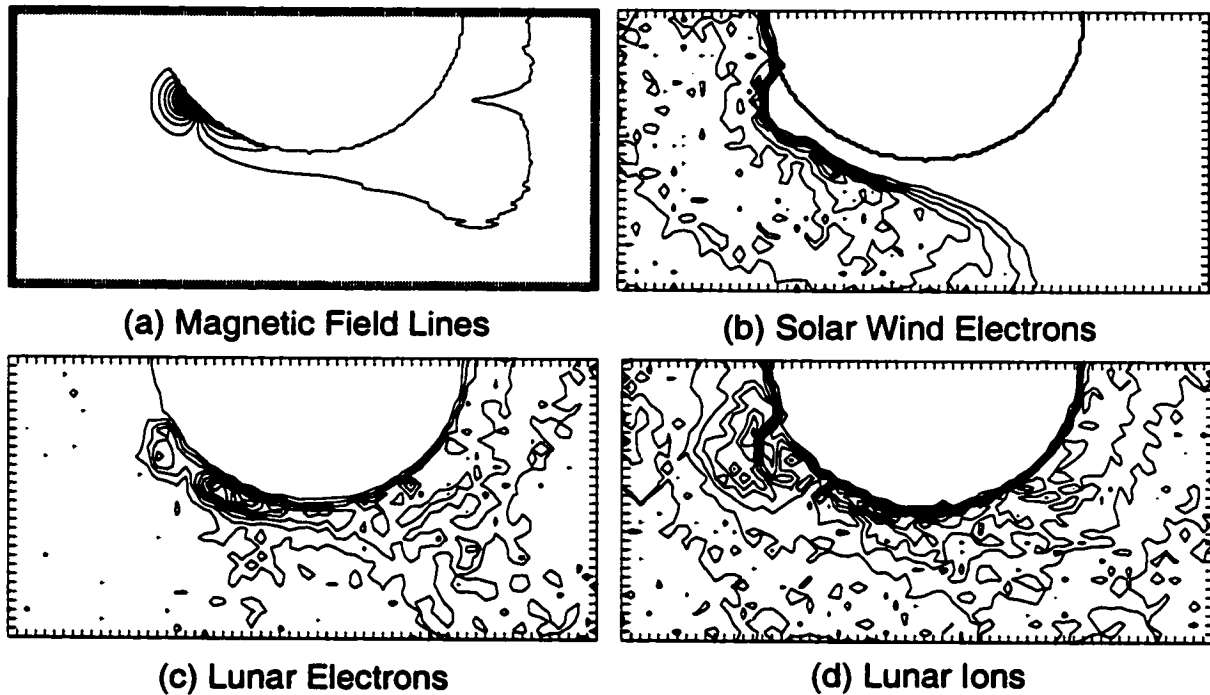


Figure 4.7: Effect of Decreased Solar Wind Velocity: Magnetic field lines and density contours for the simulations with decreased bulk velocity of the solar wind. The Lunar ion to electron mass ratio was set equal to 1024, while the bulk velocity of the solar wind was equal to 165 km/s. The particle temperatures are equal to those in Figure 4.2, at 0.02 eV for the Lunar electrons and ions, and 2.22 eV for the solar wind electrons and ions. The contour interval in (b) is 0.88 electrons cm^{-3} , 0.05 electrons cm^{-3} in (c), and 0.014 ions cm^{-3} in (d), with the densities in the center of the Moon equal to zero. The density plot for solar wind ions looks nearly identical to (b). All plots are of the same form as those in Figure 4.2.

as mass ratios, remain the same. The result is a mini-magnetosphere that is more than 100 % larger, with the magnetopause moving out from 160 km to approximately 400 km above the surface. A very large stagnation point develops downstream in the Lunar electron population, but there are no clear Lunar ion plasma voids corresponding to the enhanced electron density regions. The Lunar electron density enhancements are similar in shape to the case with the higher bulk speed, but about 10% smaller in magnitude.

The particle distributions show much less heating, particularly in the case of the electrons. The electron distributions containing the velocity component out of the simulation plane indicate the presence of anisotropic heating is similar to, but not as large as, the heating in the lower panels in Figure 4.6. And with the inflated shock surface (Figure 4.7b), position (b) in Figure 4.2 is now in the solar wind shock, while position (c) is inside the magnetopause. The thermal velocities for the cases in Figures 4.2 and 4.7 are similar in the foreshock region 1. At position (a), a particle population traveling upstream is still present but the tail of the distribution is much smaller. This is not due to fewer particles traveling upstream, but rather the particles traveling upstream have a smaller velocity. Inside the shock region (positions (b) and (c)), the mean velocity is zero, while the thermal velocity in the simulation plane is approximate 350 km/s at both positions.

When the thermal and bulk velocities were increased by an order of magnitude from the conditions in Figure 4.7, a shock-like structure still occurs but solar wind particles can penetrate all the way to the surface of the Moon. The bulk velocity translates to an ion gyroradius of 255 km and an anomalous magnetic field strength at the Lunar surface of 15 nT, too weak to hold off all of the solar wind. A shock-like structure is still present but significantly closer to the surface. Regions of enhanced Lunar electrons and depleted Lunar ions are still present though.

In all three simulations shown in Figure 4.8, the bulk velocity of the solar wind was equal to 1622 km/s. The initial temperature of the solar wind was set equal to 220 eV, while the temperature of the Lunar particles is 1.70 eV. The only difference in the three simulations in Figure 4.8 is the mass ratio of the Lunar ions to electrons, and

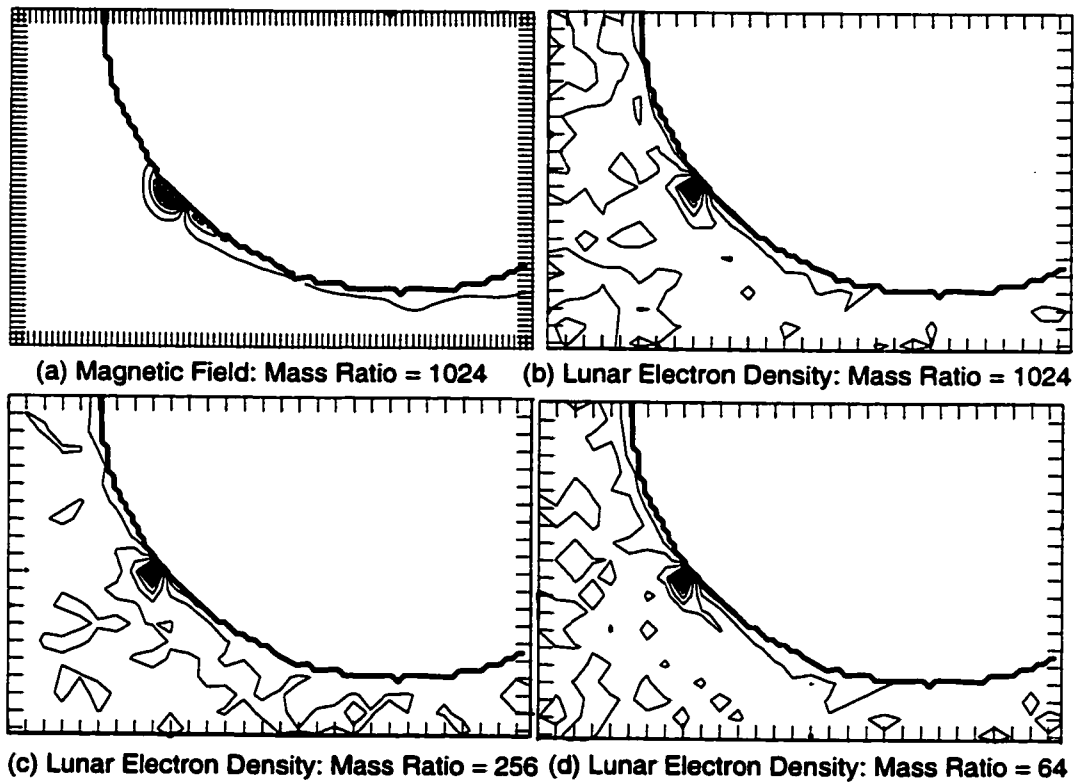


Figure 4.8: The Effect of mass ratios: Lunar electron densities for simulations with the Lunar ion to electron mass ratio equal to (b) 1024, (c) 256, and (d) 64 and magnetic field lines (a) for mass ratio equal to 1024. The bulk and thermal velocities are an order of magnitude larger than those in Figure 4.7. The bulk speed of the solar wind was equal to 1622 km/s. The temperature of the Lunar electrons and ions is 1.70 eV, while the temperature of the solar wind electrons and ions is 220 eV. The contour interval in both (b) and (d) is 0.05 electrons cm^{-3} , and 0.06 electrons cm^{-3} in (c). All plots contain an area of 2088 km by 3027.6 km and are of the same resolution as those in Figure 4.2. The thick curve has been added to indicate the surface.

consequently the solar wind ion to Lunar ion ratio.

The Lunar ion to electron mass ratio had little effect on the size and shape of the mini-magnetosphere, when all other variables were held constant. The mass ratio was set to 1024 in Figure 4.8b, 256 in Figure 4.8c, and 64 in Figure 4.8d to simulate 3 different ion populations, Argon, Neon and Hydrogen, respectively. Thus the solar wind ion to Lunar ion mass ratio is equal to 4.375 in Figure 4.8b, 17.5 in Figure 4.8c, and 70 in Figure 4.8d. The magnetic field lines in Figure 4.8a are for the simulation with a Lunar ion to electron mass ratio of 1024, but are nearly identical to the magnetic field in the simulations with the other 2 mass ratios.

The confinement of the Lunar electrons and a void in Lunar ions above the anomalous region is present in all three simulations, as in the first case (Figure 4.2) where the surface inside the mini-magnetosphere is completely shielded from the solar wind. No stagnation point is present though. A shock-like structure forms in the solar wind population above the anomaly. The solar wind density enhancement at the shock is about 40% that in Figure 4.2, while the Lunar electron density enhancement is slightly larger. The velocity distribution functions near the region show heating and acceleration signatures similar to those near the larger mini-magnetosphere in Figure 4.7.

4.2 *Non-ideal MHD Simulations*

MHD simulations can be extended to incorporate small scale dynamics like that seen in particle simulations. *Winglee* [75] showed that including a Hall term and a pressure gradient term in the Ohm's Law equation for the electric field reproduced surface plasma currents seen in particle simulations but not in ideal MHD simulations. The deviations from the ideal MHD regime in particle simulations could be accounted for by the Hall term. The localized charge separation that can also occur in particle simulations could be incorporated into MHD through a pressure gradient in Ohm's Law. This magnetoplasma dynamics (MPD) model includes electric fields generated by charge separation and accounts for deviations from ideal MHD, while remaining a fluid model. 2.5D simulations have the advantage over 2D simulations in that all three dimensions of the momentum, current and electric and magnetic field quantities are

present. But the 2.5D simulations are limited to 2 spatial dimensions. Thus plasma can only flow around the poles of the obstacle.

4.2.1 Model Parameters

The results from the particle simulations further accentuate the need to extend the ideal MHD model to incorporate small scale and non-ideal MHD effects, like those incorporated by *Winglee* [75]. Charge separation occurs in the Lunar particle populations and non-ideal MHD behavior is seen in a Hall component of the electric field which is non-zero and an ion population which becomes demagnetized.

Equations 2.1 - 2.4 are solved numerically. Accounting for regions of non-ideal MHD behavior and regions of localized non-neutrality simply means that Ohm's Law is of the (dimensionless) form:

$$\vec{E} = -\vec{v} \times \vec{B} + \eta \vec{J} + \frac{c}{\omega_{pi} L \rho} (\vec{J} \times \vec{B} - \nabla P_e) \quad (4.1)$$

\vec{E} is the electric field, \vec{B} is the magnetic field, \vec{J} is the current density, P_e is the electron pressure (and equal to half the total pressure, P), ρ is the density, η is resistivity, c is the speed of light, L is the scale size of the grid in the simulation, and ω_{pi} is the hydrogen ion plasma frequency. The ratio $\frac{c}{\omega_{pi}}$ is the ion inertial length. The resistivity (η) is set to zero outside of the Moon and the Hall and ∇P_e terms are only evaluated outside of the Moon. Like the 2.5D particle simulations, the vector quantities are three component vectors, but the spatial derivatives are only taken in two dimensions.

Sonnet [68] placed the Lunar resistivity between 10^3 ohm m and 10^5 ohm m. The Lunar resistivity in the simulations (η) is set to 10^4 ohm m. This allows the magnetic field to diffuse through the Moon and not cause an unphysical pile-up of the IMF at unmagnetized surfaces, while simultaneously not causing the simulation to go unstable (Chapter 3 and [25]). The corresponding Reynolds number inside the Moon is ~ 0.10 .

Numerical uncertainty leads to a numerical resistivity and can cause diffusion of the magnetic field even in regions where η is set to zero. The Reynolds number associated with the numerical resistivity is on the order of 50,000 in the solar wind, and an order of magnitude smaller in the mini-magnetosphere, indicating that diffusion of the

magnetic field outside of the Moon is negligible, and collisionless behavior dominates.

Since the particle motions are fundamentally small in MHD, the value of $c/(\omega_{pi}L)$ must be set to a fraction of its value. The full value, equal to 2.07, will cause the simulation to go unstable. For these MPD simulations, $c/(\omega_{pi}L)$ was set at a value of 0.10, with a value larger than 0.12 causing the code to go unstable. The larger the ratio is, the stronger the particle type effects. In the simulations by *Winglee* [75], $c/(\omega_{pi}L)$ was set equal to 0.125. Including the extra terms in Ohm's Law allows for currents and electric fields in the simulation plane, as well as magnetic fields and velocity in and out of the simulation plane. The remainder of the fluid model is explained in Chapter 2 and *Harnett and Winglee* [25].

The simulations with the modified Ohm's Law were run with the same initial conditions as the previous MHD simulations without the Hall and ∇P terms (Chapter 3 and [25]). The solar wind was assumed to be composed of H^+ ions with a density of 10 ions cm^{-3} and a velocity of 400 km/s. The Lunar density was assumed to be $0.1 \text{ Ar}^+ \text{ ions cm}^{-3}$ on the day side and 0.01 on the night side. The MPD simulations are a one ion population fluid code so an Ar^+ ion is treated as 40 H^+ ions.

The pressure and temperature of the solar wind are equal to 0.02 nPa and 12 eV. The IMF is set to 2.5 nT in the southward direction ($-\hat{z}$). Larger IMF strengths would not diffuse sufficiently fast through the Moon and would cause unphysical pile-up of the IMF at the unmagnetized surfaces (Chapter 2 and [25]). The anomalous dipole magnetic field was created with two opposing current elements placed just below the surface at 26.1 and 78.3 km below the surface, respectively. This creates an anomalous magnetic field strength equal to 30 nT at 100 km above the surface, when the surface field strength is set to 290 nT. Only the direction of the effective dipole moment was varied in the simulations.

4.2.2 Fluid Model Results

In Figure 4.9 the effective dipole moment of the anomalous region points in the northward ($+\hat{z}$) direction, thus the surface magnetic field points in the same direction as the IMF. The additional terms in Ohm's Law allow for additional currents and electric fields

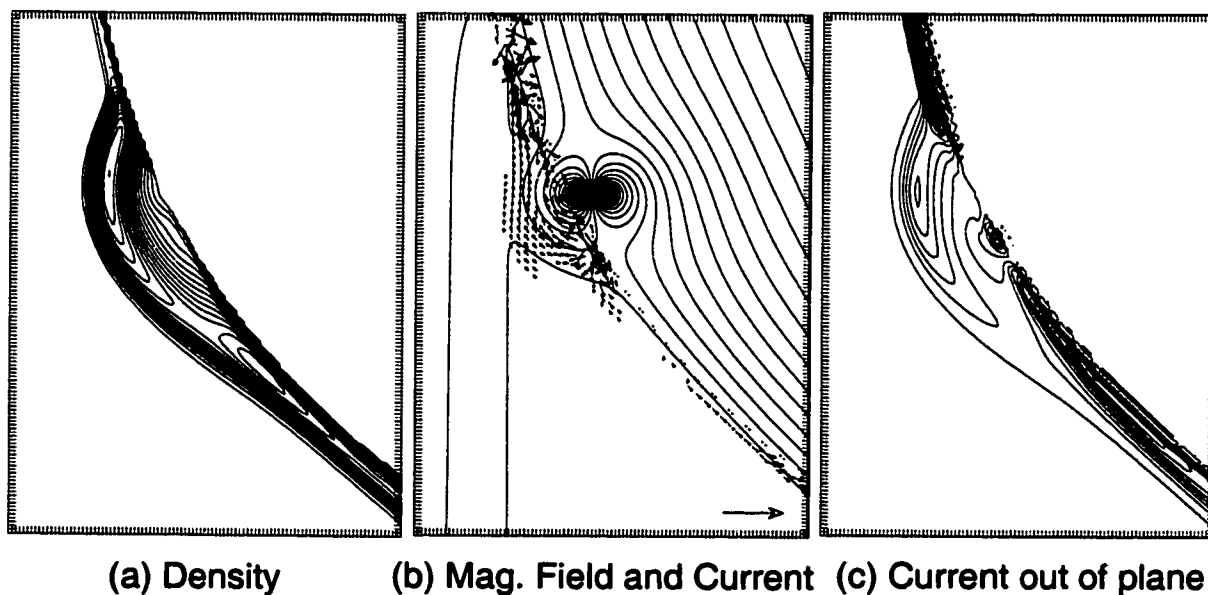


Figure 4.9: MPD simulation - IMF and dipole moment Parallel The (a) fluid density, (b) the magnetic field lines with the current density in the simulation plane and (c) the current density out of the simulation plane (c). The effective dipole moment is in the $+z$ direction, anti-parallel to the IMF. The tick marks on the axes are equal to 8.7 km and the boxes contain an area 870 km by 1218 km. The contour interval in the density plot is equal to 2.1 ions cm^{-3} , with the density in the solar wind equal to 10 ions cm^{-3} . The arrow in the lower right hand corner of (b) indicated a current density magnitude of 53.9 nA/m^2 . The contour interval in (c) is 129.7 nA/m^2 , with the current density in the solar wind approximately zero. The dotted line in plot (b) indicates the surface of the Moon.

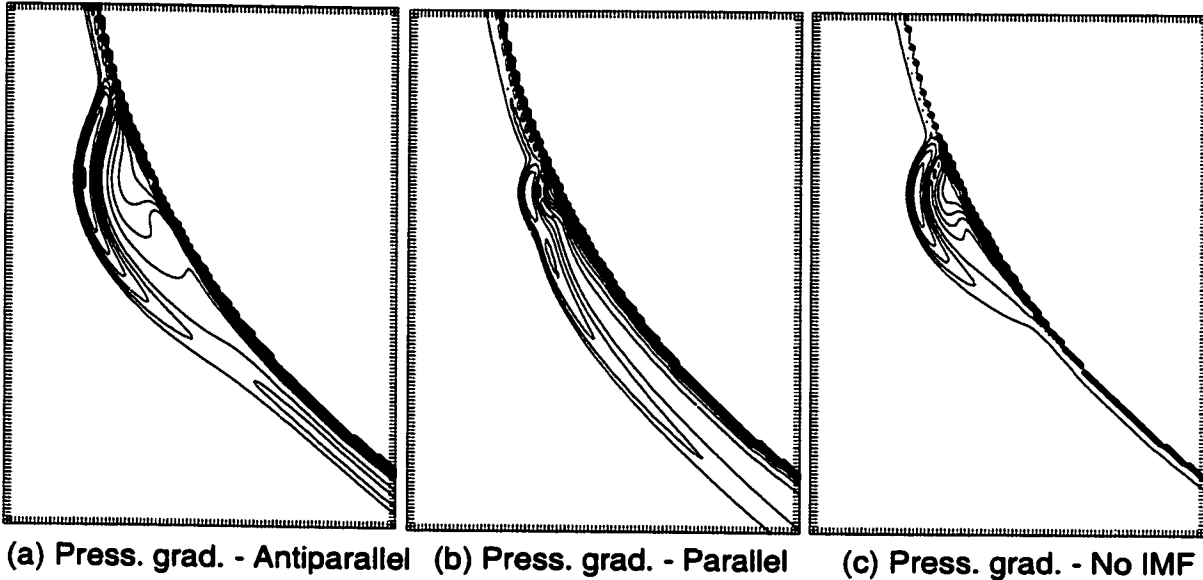
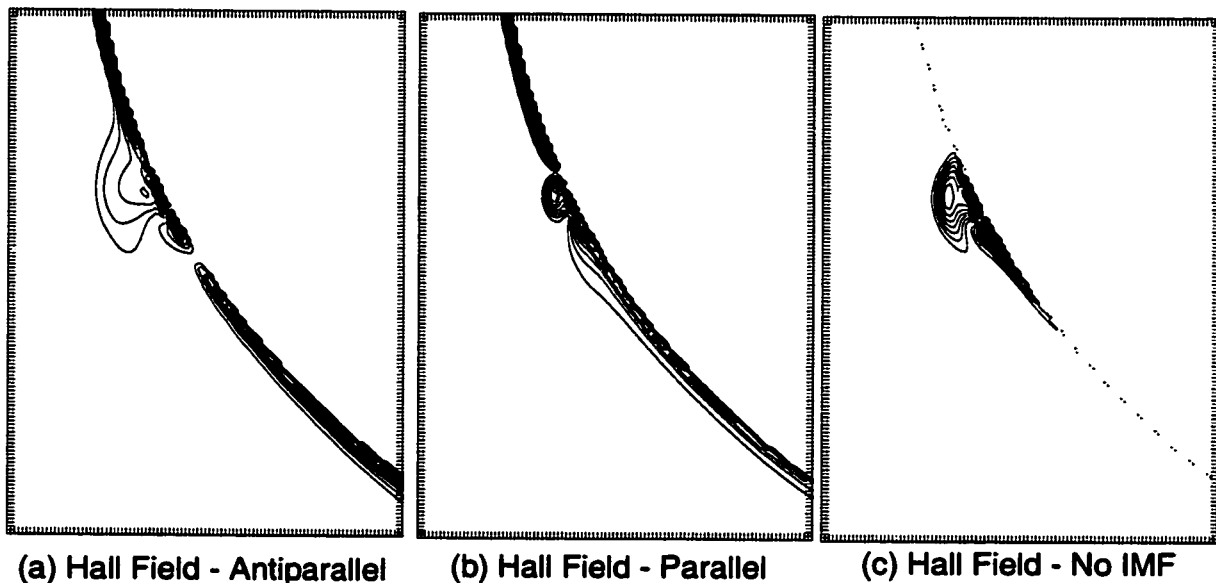


Figure 4.10: The magnitude of the pressure gradient (∇P) component of the electric field for the cases when (a) the dipole moment is anti-parallel to the IMF (Figure 4.9), (b) the dipole moment is parallel to the IMF (Figure 4.12), and (c) the IMF is zero (Figure 4.13). The contour interval in (a) is $64.4 \mu\text{V/m}$, $94.8 \mu\text{V/m}$ in (b) and $78.6 \mu\text{V/m}$ in (c). The boxes are of the same forms and size as in Figures 4.9, 4.12, and 4.13.

but cause no change in shape of the mini-magnetosphere. The internal structure of the density and pressure inside the mini-magnetosphere is altered slightly, with the maxima pressure, densities and temperatures reduced by about 10%. This is due to a slightly smaller time step in the simulations, which translates to a slight increase in numerical diffusion of the magnetic field in the plasma. With increased numerical diffusion of the magnetic field in the mini-magnetosphere, the plasma will not build up as much. The shape of the shock surface remains the same but due to the reduced internal pressure, density and temperature the shock height moves in about one grid point. The stagnation point occurs at the same location as in the the 2D MHD simulations, about 540 km downstream.

The current density (Figure 4.9b) in the simulation plane near the anomaly is field aligned in most regions. The magnitude of the current density in the simulation plane is about an order of magnitude smaller than the current out of the simulation plane in the shock region. Above the anomaly, the current density forms a circulation



(a) Hall Field - Antiparallel

(b) Hall Field - Parallel

(c) Hall Field - No IMF

Figure 4.11: The magnitude of Hall ($\vec{J} \times \vec{B}$) component of the electric field for the cases when (a) the dipole moment is anti-parallel to the IMF (Figure 4.9), (b) the dipole moment is parallel to the IMF (Figure 4.12), and (c) there IMF is zero (Figure 4.13). The contour interval in (a) is $77.4 \mu\text{V/m}$, $118.4 \mu\text{V/m}$ in (b) and $66.3 \mu\text{V/m}$ in (c). The boxes are of the same forms and size as in Figures 4.9, 4.12, and 4.13. The dotted line in (c) indicates the surface of the Moon.

pattern. The region that separates currents traveling in opposite directions is in the density gradient near the surface, inside of the density maxima and approximately 70 km above the surface when directly opposite the location of the dipole generating current elements. These plasma surface currents are created by the charge separation at the magnetopause. The electrons are stopped first by the anomalous magnetic field and move with the bulk flow down and around the anomaly, creating a current in the upward direction. The ions penetrate further into the mini-magnetosphere before being deflected down and around, creating a current in the downward direction.

The electric field in the simulation plane is significant only at the edge of the shock surface, where it points into the solar wind, and in the inner portion of the mini-magnetosphere directly opposite the buried dipole, where it points toward the surface. The electric field at the shock surface is primarily the result of a strong pressure gradient (Figure 4.10a), further indicating the presence of charge separation. Solar wind ions are able to penetrate further into the mini-magnetosphere, creating the electric field at the shock surface, pointing into the solar wind.

The electric field pointing toward the surface suggests an excess of electrons near the surface and/or a deficit of ions. The pressure gradient (Figures 4.10a) is significant in the region directly above the anomaly, but its effect on the electric field is reduced by a Hall field (Figure 4.11a) in the opposite direction. The charge separation in this region is the result of the non-ideal MHD behavior, seen in the non-zero Hall field (Figure 4.11a). The velocity of the plasma inside the shock, opposite the anomaly, is small. Therefore charge separation would not be the result of the momentum difference in the ions and electrons that leads to the charge separation at the shock surface. Also such mass effects would create an electric field in the opposite direction of the one present at the surface. Instead the non-ideal plasma behavior leads to a deficit of ions relative to the electron density. Since there is a relative deficit of ions where both the plasma density and magnetic field increase, it suggests the ions have become demagnetized, and are no longer frozen to the magnetic field as a fluid. That the Hall and pressure gradient terms are non-zero throughout the mini-magnetosphere, but cause little modification of the shape and size of the mini-magnetosphere indicates that the bulk

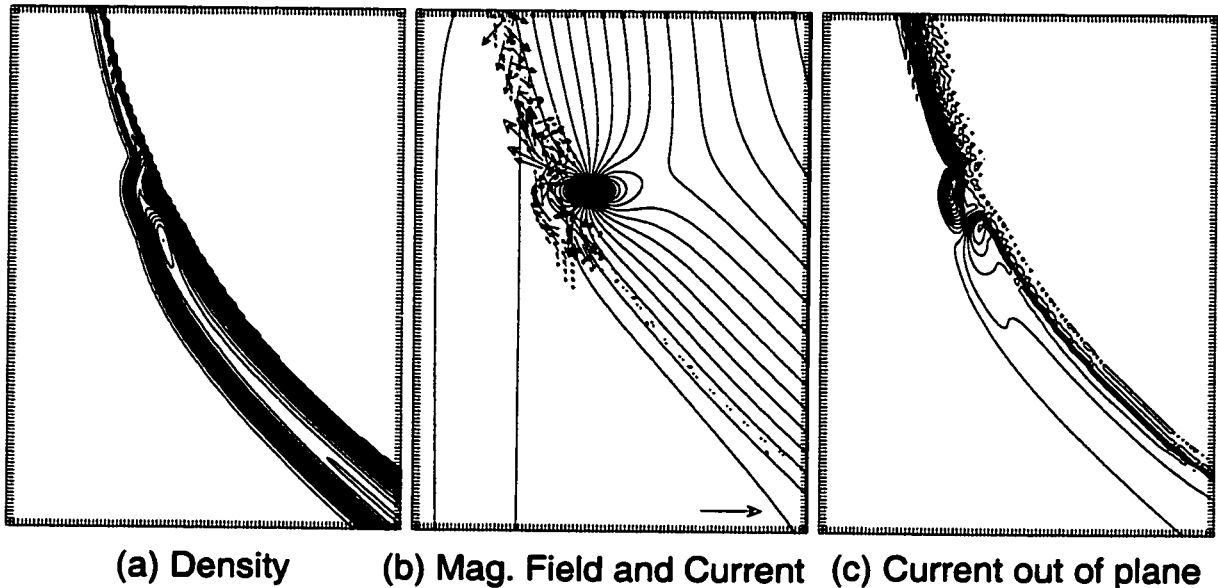


Figure 4.12: MPD simulation : IMF and dipole moment anti-parallel The effects of flipping the effective dipole moment from $+\hat{z}$ to $-\hat{z}$, now parallel to the IMF. The plots are of the same form and scale as in Figure 4.9. The contour interval in the density plot is equal to 2.0 ions cm^{-3} , with an interval of 171.8 nA/m^2 for the current density. The magnitude of the reference arrow in (b) is 65.1 nA/m^2 .

characteristics of the mini-magnetosphere are determined largely by fluid behavior.

When the direction of the effective dipole moment of the anomalous magnetic field is flipped (to $-\hat{z}$), the size and shape of the mini-magnetosphere changes dramatically due to interactions with the IMF (Figure 4.12), as was seen in the previous 2D MHD simulations. Near the anomaly, the pressure, density and temperature are again reduced by about 10% from the 2D simulation due to the smaller time step. As a result the shock height is one grid point lower directly above the anomaly.

The electric field in the simulation plane is occurs primarily at the shock surface. Only a weak electric field points toward the surface above the anomaly. This is due to the increase in the Hall term. Both the Hall term and space charge field (associated with the pressure gradient) in the region directly opposite the anomaly have increased from the case in Figure 4.9 but the Hall term increases by a larger percentage (the magnitude of the space charge field is double while the Hall term magnitude

is triple the corresponding terms for the case in Figure 4.9). Thus near the anomaly, both charge separation and non-ideal MHD behavior are more prevalent than in the previous case, even though the electric field is smaller.

The direction of the anomalous magnetic field at the surface is in the opposite direction as the IMF. This allows for wide scale reconnection. As a result there is fluid flow into the cusp-like regions. Large currents are associated with this flow into the cusp regions. The current density (Figure 4.12b) in the cusp regions are approximately 1.5 times larger than the largest currents seen in Figure 4.9b. The surface plasma currents opposite the anomaly in Figure 4.12b are approximately 2.5 times larger than the currents in the same location in Figure 4.9b but still about half the magnitude the cusps currents. Thus the circulation pattern in the charge density associated with charge separation at the magnetopause is present but occurs over a more compressed region, leading to larger current densities. The surface plasma current is still an order of magnitude smaller than the current density out of the simulation plane, due to the overall increase in the magnitude of the current near the anomaly.

The direction of the current relative to the fluid velocity in the cusps suggests that the large cusp currents are due to electron precipitation. The fluid flow is down to the surface while the current is out from the surface. Large currents out of the Earth's ionosphere can occur in the night-side auroral zone during an auroral event. These currents are associated with electron precipitation into the auroral zone and are typically associated with southward IMF. The large currents in the cusp of the mini-magnetosphere are only present in the configuration that is analogous to southward IMF configuration for the Earth (Figure 4.12).

It was noted previously (Chapter 3 and [25]) that the internal structure of this mini-magnetosphere (Figure 4.12) approached the size of the ion gyroradius. One might expect that the largest modification to the mini-magnetosphere by the non-ideal MHD terms would come in such a case. Directly above the anomaly the magnitude of the Hall field (Figure 4.11b) does have a maximum value approximately 3 times larger than that in the larger mini-magnetosphere (Figure 4.11a), but the Hall field is non-zero over a much smaller region due to the smaller size of the mini-magnetosphere.

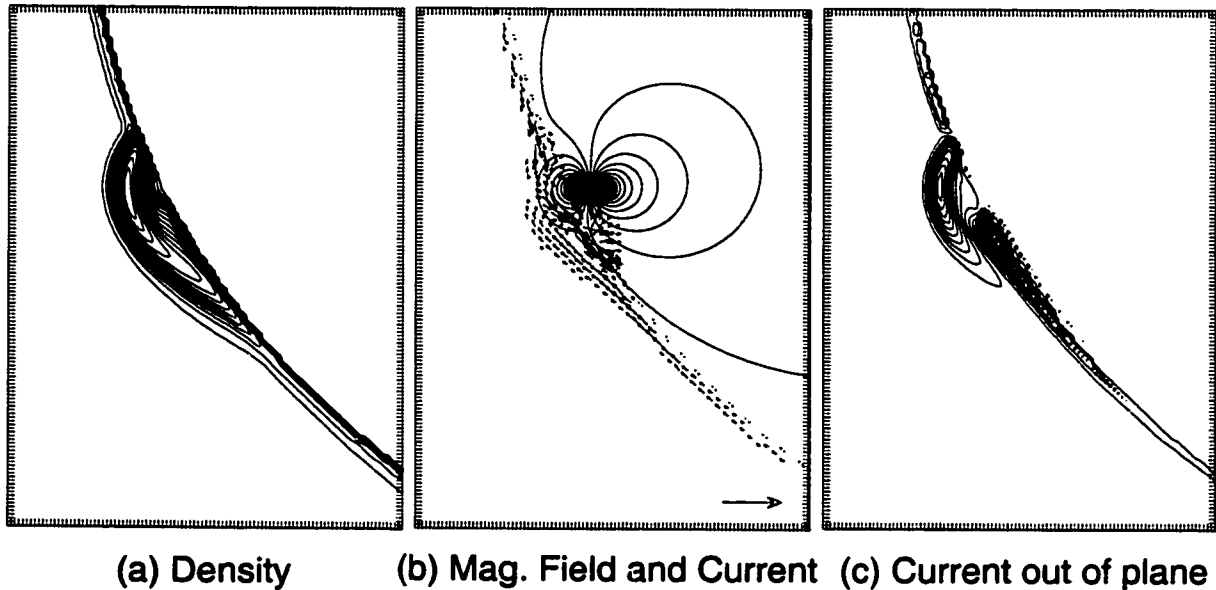


Figure 4.13: MPD simulation : no IMF The effects of no magnetic field in the solar wind. The plots are of the same form and scale as in Figure 4.9. The contour interval in the density plot is equal to 1.6 ions cm^{-3} and 114.1 nA/m^2 for the current density out the plane. The magnitude of the reference arrow in (b) is 91.3 nA/m^2 .

Thus while the non-ideal MHD effects are stronger, they occur over a much smaller area within the mini-magnetosphere leading to little change from the ideal MHD simulations.

To make a more compatible comparison between the MPD simulations and the particle simulations, the IMF needs to be set to zero in the MPD simulations (Figure 4.13). With no IMF, the mini-magnetosphere is very round and no stagnation point develops. The mini-magnetosphere is nearly identical to the mini-magnetosphere that formed in the ideal 2D MHD simulations (Figure 3.3 and [25]) when the IMF was set to 5 nT in the ecliptic plane and B_z was set to zero. The shock height directly opposite the buried dipole for both cases is 130 km even though the maxima pressure, density and temperature are approximately 5% smaller for the MPD simulation with no IMF due to the decreased time step.

The lack of B_z results in a smaller mini-magnetosphere, with less build-up of pressure and density. The maximum temperature is the same as the case in Figure 4.9,

but the maxima in pressure and density are smaller in the case with no IMF. With no IMF the magnetic field of the anomaly is compressed but fluid can flow around the anomaly unimpeded by IMF. This is evident in that no stagnation point forms when the IMF is zero. Reconnection of the IMF to the anomalous magnetic field can lead to regions of inhibited fluid flow and the development of stagnation points, increasing the pressure and density.

The magnitude of the Hall field (Figure 4.11c) directly opposite the anomaly is roughly 1.5 times larger than for the case in Figure 4.11a, but about half the value in Figure 4.11b. It is non-zero throughout a larger percentage of the mini-magnetosphere, since the Hall field is minimal in the flank/tail region of the mini-magnetosphere in Figures 4.9 and 4.12, as those regions are associated with solar wind flow. Thus the smaller the mini-magnetosphere, the more prevalent the non-ideal MHD behavior.

Substantial currents also form near the lower cusp-like region in the case with no IMF and are larger than those in the previous case (Figure 4.12), but the direction of the current is not the same. In the previous case, the large currents are directed out of the cusp. But in the case with no IMF, the large currents are tangent to the Lunar surface and in the direction of the bulk flow, suggesting they are associated with a compressed region of ion flow. The upward currents associated with the downward electron flow are comparable in magnitude to those in Figure 4.12b.

4.3 Comparison between particle and MPD simulations

The rounded shape of the mini-magnetosphere and magnetic field geometry is similar in the particle simulations and the MPD simulations where large scale reconnection to the IMF does not occur. And the topology of the Lunar electron density is very similar to the density topology in Figures 4.9 and 4.13. Both types of simulations have large density concentrations directly between the solar wind and the magnetic anomaly, and for some cases in the MPD simulations, in the downstream region as well. While a stagnation point is present in some of the particle simulations (where the IMF is zero), no stagnation point is present in the fluid simulations if B_z is zero. A stagnation point is present in the MPD simulations only when B_z is non-zero.

The cusps form a possible entry point for solar wind plasma to reach the surface. Flow into the cusp is seen in the fluid simulations, and in the southward IMF configuration electron precipitation into the cusps generates large currents. The velocity and density in the particle simulations, on the other hand, indicate there is no flow into the cusp by the solar wind for the strong magnetic field cases (Figures 4.2 and 4.7), as the solar wind ions and electrons are completely deflected by the magnetic anomaly.

The solar wind in the particle simulations is accelerated, as well as heated, as it encounters the shock region. These regions are most prominent at the subsolar point for the solar wind electron population and in the flank region for the solar wind ion population. The acceleration is evident as an increase in the bulk velocity. The effects of heating appear as spreading of the velocity distribution functions. The fluid in the MPD simulations is heated, but the bulk flow is never accelerated above the initial solar wind speed. This is inherent to MHD/MPD, as it can not predict the production of high energy tails in the velocity distribution.

An electric field, due to the pressure gradient, pointing into the solar wind at the shock surface in all of the MPD simulations indicates the presence of charge separation at the shock surface and that the ion population of the solar wind penetrates further into the mini-magnetosphere than the electrons. The solar wind in the particle simulations also exhibits a similar charge separation at the sub-solar point. Charge separation of the solar wind in the particle simulations also occurs in the downstream region, near the stagnation point.

Charge separation of the Lunar population in the particle simulations also occurs at the sub-solar point. This excess of electrons and deficit of ions seen in the Lunar population of the particle simulations creates an electric field similar to one in the MPD simulations. An electric field pointing toward the surface, due to a non-zero Hall field and a pressure gradient, indicates a deficit of ions relative to the electron density near the surface in the MPD simulations. Since the charge separation occurs where the momentum of the plasma is small, it must be due to non-ideal MHD behavior, rather than mass separation like that which occurs at the shock surface. Thus the MPD simulations can capture both the charge separation and ion demagnetization

that is seen in the particle simulations.

This region of enhanced electrons and a void of ions encompasses the entire mini-magnetosphere in the particle simulations. The magnitude of the Hall field in the MPD simulations is large near the surface directly above the magnetic anomaly, but small in the downstream region of mini-magnetosphere. The region of charge separation near the surface is large relative to the size of the mini-magnetosphere only in the case with no IMF, where the scale size of the mini-magnetosphere is small. Thus the ions in the MPD simulations only become demagnetized directly opposite the anomaly. This is due to not incorporating the full strength of the particle effects, seen in the reduced value of $c/(\omega_{pi}L)$ in Formula 4.1.

A circulation pattern in the current, due to momentum (thus charge) separation at the magnetopause, is seen in both the particle simulations (Figure 4.3a) and the MPD simulations (Figures 4.9b, 4.12b, and 4.13b) but is most prominent in the downstream in the particle simulations rather than above the anomaly as in the MPD simulations. In the particle simulations there is charge separation of the solar wind at the subsolar point but it is minor compared to the charge separation in the downstream region. Thus the largest currents in the simulation plane occur near in the downstream region.

Magnetopause currents form at the bow shock in both particle and MPD simulations. Additional currents out of the plane form in both types of simulations but not at the same location. In the MPD simulations, the downstream current forms around the cusp and near the surface (Figures 4.12c and 4.13c) while in the particle simulations, the additional current out of the plane is in the flank region past the cusp (Figure 4.3b), and above the stagnation point. This is due the lack of IMF in the particle simulations and the fact that the solar wind is completely held off the surface and deflected around the magnetic anomaly. In both cases the current is due to the electric field associated with the flow of solar wind ions across the Lunar magnetic field (i.e. $\mathbf{E} = -\mathbf{v}_{\text{solar}} \times \mathbf{B}_{\text{Moon}}$).

The currents in the MPD simulations are similar to the plasma surface currents seen at the Earth's magnetopause in simulations by *Winglee* [75]. In both cases, the surface currents are approximately an order of magnitude smaller than the magneto-

pause current in the dawn-dusk direction. Only one current system forms in the bow shock-magnetopause region in the MPD simulations, even with a non-zero IMF, rather than a separate current system at each boundary. Therefore the general appearance of the current is similar to the particle simulations where no IMF is present. This suggests that the current systems are compressed even in the conditions when a separate bow shock current might form. Like the MPD simulations, the current out of the plane in the particle simulations is an order of magnitude larger than that in the plane.

The Hall field out of the simulation plane in the particle simulations is non-zero throughout most of the mini-magnetosphere (Figure 4.2f). In the MPD simulations the component of the Hall field out of the simulation plane is non-zero only very near the anomaly. But the components in the simulation plane are non-zero throughout the mini-magnetosphere. Thus the non-ideal MHD regions in the MPD simulations (Figure 4.11) are comparable in size to those in the particle simulations, but the region of ion demagnetization is significantly smaller in the MPD simulations.

4.4 Summary

2.5D particle simulations confirm the earlier MHD result that magnetic anomalies on the surface of the Moon can hold off the solar wind and cause a mini-magnetosphere to form. The solar wind is slowed and heated as it encounters the mini-magnetosphere. Particle acceleration also occurs, but in the mini-magnetosphere, two separate acceleration regions form, one at the sub-solar point, primarily for electrons and the second in the downstream region, primarily for ions. The small size of mini-magnetospheres results in a merging of the internal boundaries. A clear difference between the bow shock and magnetopause is not present as it is in large scale magnetospheres.

Decreasing the bulk speed of the solar wind decreases the ion gyroradius, and translates to an increase in the magnitude of the magnetic field on the Lunar surface. This leads to inflation of the mini-magnetosphere. The converse happened when the solar wind bulk speed was increased. Varying the ion to electron mass ratio for the surface ionosphere, on the other hand, had little effect on the size and shape of the mini-magnetosphere.

Small scale and non-ideal MHD effects were included in the fluid simulations, through a modified Ohm's Law. The extra terms also include previously neglected currents and electric fields in the simulations plane. The mini-magnetospheres that formed in the MPD model are nearly identical in size and shape to those in the ideal MHD simulations. Magnetopause currents similar to those seen in the particle simulations are present but are not most prominent in the exact same place, due to differences in the extent of charge separation of the surface ions. Separate bow shock and magnetopause current system do not form in the MPD simulations when the IMF is non-zero, further indicating a merging of the internal boundaries has occurred.

The MPD simulations predict charge separation at the shock surface and near the surface, directly above the anomaly. The charge separation at the shock surface is due to the larger momentum of the ions and results in an electric field and surface plasma currents. The charge separation and non-zero Hall field near the surface are due to non-ideal MHD fluid behavior, implying a deficit of ions relative to the electron density near the surface because the ions have become demagnetized. Thus the magnetoplasma dynamics model (MPD) can predict the density distributions of the solar wind and the Lunar electrons, as well as the configuration of the magnetic field. And the behavior of the demagnetized Lunar ions can be inferred from the resulting electric fields and currents.

Chapter 5

2.5D SIMULATIONS OF MULTIPLE DIPOLE ANOMALIES

Initial 2D MHD simulations indicated that mini-magnetospheres can form around magnetic anomalies on the surface of the Moon, but required magnetic field strengths at 100 km above the surface an order of magnitude larger than in situ measurements. Modeling the lunar magnetic anomalies with multiple dipoles in 2.5D MHD simulations inflates the size of the mini-magnetospheres for only small increases in the magnitude of the total magnetic field. Multiple dipoles increase the lateral distance over which solar wind plasma is held off the surface. This extended magnetic field geometry inflates the mini-magnetosphere by inhibiting fluid flow within the shock region. With multiple dipoles, a mini-magnetosphere will form with magnetic field magnitudes smaller than the lower limit for a single dipole. These results indicate that the higher order moments of the anomalous magnetic fields play a significant role in deflecting the solar wind and determining the size and shape of the mini-magnetosphere.

5.1 Introduction

The initial 2D MHD simulations of the solar wind interaction with the lunar magnetic anomalies (Chapter 3 and [25]) indicated that the crustal magnetic fields can hold off the solar wind and form a “mini-magnetosphere” (a small scale magnetosphere). A mini-magnetosphere would form in the 2D MHD simulations when a dipole buried 50 km below the surface had a surface field strength of 290 nT at the surface and greater than 10 nT at 100 km above the surface, for solar wind velocity and density equal to 400 km s⁻¹ and 10 cm⁻³, respectively. When the velocity was 400 km/s and the magnetic anomaly was 290 nT at the surface and 30 nT at 100 km, a mini-magnetosphere formed for solar wind densities less than 40 cm⁻³.

One inconsistency arose from the comparison of the 2D MHD simulations and

observations of possible mini-magnetospheres made by Lunar Prospector [45]. The strength of the magnetic field at 100 km above the surface needed to be an order of magnitude larger than values observed by Lunar Prospector in order for mini-magnetospheres to form at satellite altitudes. Lunar Prospector found that in the lunar wake, the in-situ field strengths above the anomalies that had shock-like structures when facing into the solar wind, were on the order of a few nanotesla [(*Lin et al.*, private communication, 1999) and (*L.L. Hood*, private communication, 2001)]. In the initial simulations, the field strength at 100 km above the surface dipole had to be set to approximately 30 nT in order for a mini-magnetosphere to form at satellite altitudes.

The extra currents and electric fields that arose from extending the model to non-ideal MHD, incorporating small scale effects (Chapter 4 and [24]), did add extra features to the mini-magnetosphere and allow for a better understanding of the physical processes occurring, but they caused no inflation of the mini-magnetosphere. Some other mechanism is needed to cause a mini-magnetosphere to form at higher altitudes with smaller anomalous magnetic fields.

The larger than observed anomalous magnetic field strength required at 100 km may be due to modeling the anomalous magnetic field with a simple dipole. The outermost shock surfaced formed between 100 to 200 km above the surface with the lateral extent of the mini-magnetospheres approximately an order of magnitude larger. With plasma and magnetic field interactions occurring close to the source region of the anomalous magnetic field, a single dipole approximation is likely to breakdown. The strength of the higher order terms could be comparable to the strength of the dipole term when considering a more realistic model of the crustal magnetic field.

The results presented in this chapter show the effects of modeling anomalous magnetic fields as a collection of dipoles rather than a single dipole, and how a complex magnetic field geometry modifies the plasma dynamics. It is also an intermediate step necessary for creating realistic magnetic fields in 3D simulations. Different methods can be used to model the individual anomalies, such as multiple dipoles or spherical harmonics. A multiple dipole technique was used by *Hood and Williams* (1989) to

model anomalies on the Moon. In their simulations, 9-15 dipoles were used to create a source region approximately 200 km by 200 km with field strengths on the order of 1000 nT at the surface and 2 nT at 100 km above the surface.

5.2 Model parameters

The simulations with the multiple dipoles were run with the same initial conditions as previous simulations in Chapter 3 and Chapter 4 [25, 24]. The fluid equations 2.1 - 2.4 remain the same. while the electric field equation remains the same as 2.15. The resistivity (η) is set to zero outside of the Moon and the Hall and ∇P_e terms that account for non-ideal MHD behavior and regions of localized non-neutrality, are only evaluated outside of the Moon. The vector quantities are three component vectors, but the spatial derivatives are only taken in two dimensions.

The solar wind was assumed to be composed of H^+ ions with a density of 10 cm^{-3} and a velocity of 400 km s^{-1} . The lunar density was assumed to be $0.1 \text{ Ar}^+ \text{ cm}^{-3}$ on the day side and 0.01 on the night side [33, 27]. The ion density can not be set to zero at the lunar surface as it would introduce division by zero. The lunar density is low enough that the surface acts as a sink for undeflected solar wind. These 2.5D MHD simulations are a one ion species code so an Ar^+ ion is treated as 40 H^+ ions.

The pressure and temperature of the solar wind are equal to 0.02 nPa and 12 eV. The IMF was set to 2.5 nT in the southward direction ($-\hat{z}$), and the resistivity of the Moon was set to 10^4 ohm m to allow for sufficient diffusion of the IMF through the Moon and prevent unphysical pile-up at unmagnetized surfaces. *Sonnet* (1975) placed the resistivity of the lunar rock between 10^3 ohm m and 10^5 ohm m . The associated Reynolds number inside the Moon is then approximately 0.10, indicating that diffusion dominates that region. Numerical uncertainty can lead to numerical diffusion even in the region where η is set to zero. The Reynolds number associated with numerical diffusion is on the order of 10^4 , and the region is thus dominated by convection.

The dipole fields were created with two opposing current elements. The separation and depth of the current elements could be varied to change the characteristics of the surface field. The anomalous fields were assumed to be in the southern hemisphere at

a latitude around 25°S . In the initial 2D simulations, each of the dipoles that comprised the anomalous magnetic field were created with two opposing current elements placed at 26.1 and 78.3 km below the surface, respectively. This produced a magnetic field for a single dipole equal to 290 nT at the surface and 30 nT at 100 km. Additional dipoles can be added to increase the rate of fall-off of the magnetic field at high altitudes. The remainder of the MHD model is presented in Chapter 2 and 3 [25], with the discussion of the expansion to non-ideal MHD (MPD) discussed in Chapter 4 [24].

The simulations were run with either two or four dipoles present and with varying orientations for the dipole moments and field strengths. The dipole configurations are summarized in Table 5.1 for the cases with two dipoles and in Table 5.2 for the cases with four dipoles. The combination of multiple dipoles generates higher order magnetic moments. In the figures and tables the horizontal, or \vec{x} , axis is parallel to the ecliptic plane pointing away from the Sun. The vertical, or \vec{z} , axis is perpendicular to the ecliptic plane, with $+\vec{z}$ pointing in the direction of north. Radial vectors originate from the center of the Moon. The resolution of the simulations in the regions shown is 8.7 km.

5.3 Two Dipoles

When two dipoles, with dipole moments in the $+\vec{z}$ direction, are placed 150 km apart, the distance of the shock from the surface is nearly double the distance when only one of those dipoles is present (Figure 5.1a), while the general shape of the mini-magnetosphere remains the same. Directly opposite the lower dipole the shock surface forms 270 km above the surface, 42% higher than when the upper dipole was not present. In the downstream region the shock surface forms 225 km above the surface, an increase of 138% from when only one dipole is present. The lower dipole is at the same position as those in the single dipole simulations [25, 24].

The field strength is 91 nT at the surface half way between the two dipoles and 29.5 nT at 100 km above the midpoint. The magnitude of the magnetic field magnitude at

Figure	Depth (km)	Dipole Moment	Surface Field (nT)	Field at 100 km (nT)
5.1A	60.9	+z	231	35.7
	52.2	+z	313	33.3
5.1B	60.9	-z	231	35.7
	52.2	-z	313	33.3
5.1C	26.1	-z	216	8.58
	17.4	+z	575	14.6
5.1D	26.1	+z	216	8.58
	17.4	-z	575	14.6

Table 5.1: 2 dipoles: Dipole parameters for the results in Figure 5.1. The depth of the dipole is the depth of the midpoint between the two current elements that create the dipole field. The directions of the dipole moments ($\pm z$) are all parallel to the vertical axis and the IMF ($-z$). The dipoles are listed in decreasing z position and increasing x , thus the first dipole listed in each case is the dipole closest to the top of the simulation box, and conversely, the last dipole listed is closest to the bottom of the box. The magnetic field strengths are taken at points on a horizontal line through the dipole location.

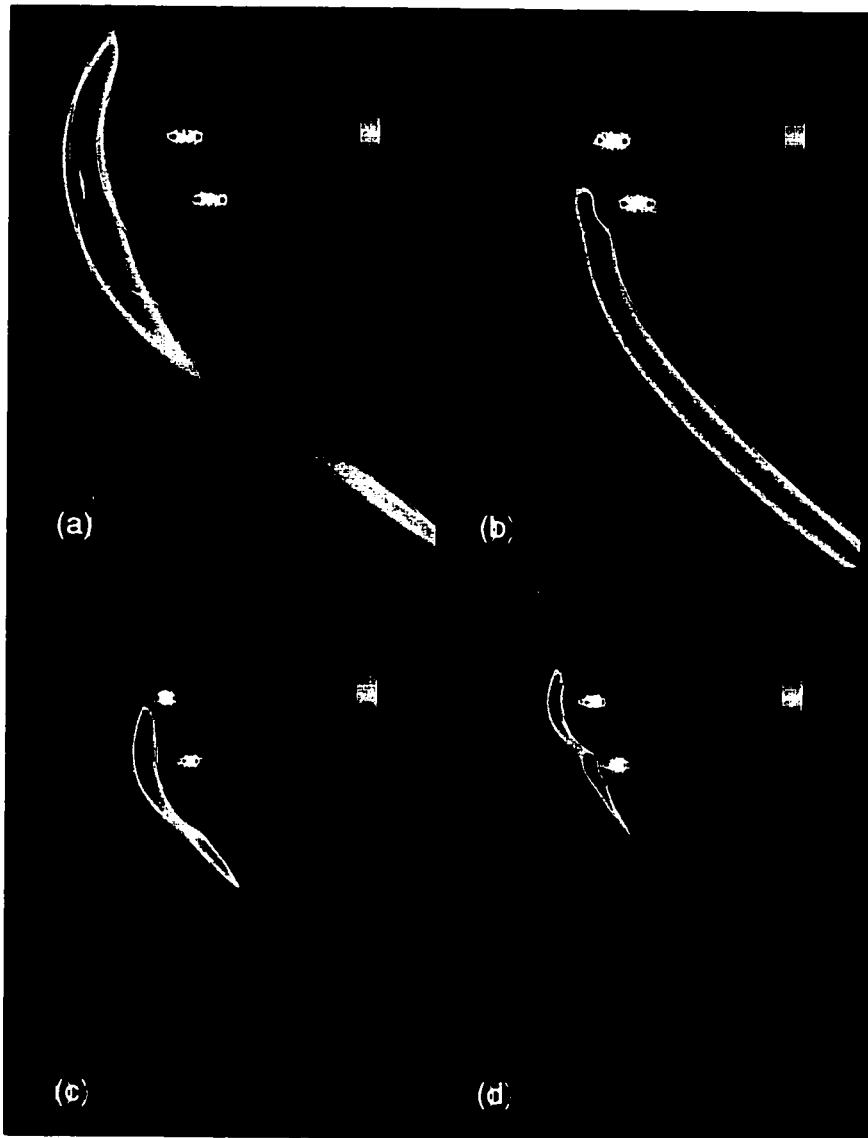


Figure 5.1: 2 dipoles: Density plots and magnetic field lines for four different cases with two dipoles. The orientation and strength of the dipole fields are defined in Table 5.1. The dipole moments are in the $+z$ direction producing a large magnetic field at 100 km in (a) then both dipoles are flipped to the $-z$ direction with the same magnitude in (b). In (c) the dipole moments are opposing directions, and then each dipole moment is flipped 180° in (d). The moon has a constant density of 4.0 cm^{-3} and the solar wind a density of 10.0 cm^{-3} . The boxes contain an area 870 km by 1218 km, with each tick mark equal to 5 grid points or 43.5 km. The density contours were smoothed slightly to reduce minor pixilation. The maximum value in the density corresponds to white on the color bar.

100 km above the lower dipole is 32 nT and 313 nT at the surface (Table 5.1), both only 10% larger than with the single dipole in the previous results. Therefore the fall-off of the magnetic field with altitude, relative to the surface field, is similar in both the single dipole and double dipole cases. The increased size of the mini-magnetosphere is not due to a substantial increase in the total field strength, but rather the increased lateral extent of the anomalous region.

The temperature of the plasma inside the mini-magnetosphere is comparable to the case with only one dipole. The presence of the second dipole inhibits fluid flow but does not increase the heating of the plasma. When the plasma is diverted around one of the dipoles, it can encounter another dipole which prevents the plasma from simply flowing around the surface of the Moon, causing the plasma to stagnate. Since the inhibited flow also inflates the mini-magnetosphere, the plasma is not compressed as much which results in less heating, as the pressure and density can not build up. The pressure and density in the region in between the two dipoles is comparable to the values in the region directly opposite a single dipole as the inflation of the mini-magnetosphere reduces the build up of pressure and density. The stagnation point forms further downstream in the simulation with 2 dipoles but the pressure and density at the stagnation point are also comparable to the values when only one dipole is present.

In Figure 5.1b, the two dipoles have the same location as in Figure 5.1a, the only difference is both dipole moments have been flipped 180° so that they are both pointing southward ($-\hat{z}$ direction). The anomalous surface field is now anti-parallel to the IMF. The magnitude of the total anomalous magnetic field remains the same as in Figure 5.1a. The overall shape of the shock is similar to when only one dipole of the same orientation is present. The shock forms 100 km above the upper dipole and 120 km above the lower dipole, comparable to the height the shock formed above a single dipole of the same orientation. Instead of inflating the mini-magnetosphere above the anomalous region the inhibited fluid flow causes the shock in the downstream region to flair out such that between 150 and 500 km downstream the shock surface is 40% higher than when only one dipole is present.

The density and pressure enhancements just directly opposite the upper dipole are similar to the values when only one dipole of the same orientation is present, while the enhancements opposite the lower dipole and are 50% larger than for a single dipole. The significant increase in the density and pressure opposite the lower dipole is due to the presence of stagnant plasma. The density and pressure opposite the lower dipole are almost identical to the values at the stagnation point for one dipole, with the maximum density and pressure at the stagnation point in Figure 5.1b only 10% and 20% larger, respectively, than at the center of the stagnation point with one dipole. The stagnation point in both cases is caused by kinks in the reconnected magnetic field. With an increased anomalous magnetic field region, erosion of the anomalous field by the IMF is reduced and, the inhibition of fluid flow by the total magnetic field is enhanced.

The tail flairs out due to the additional magnetic field in the flank region and the increased build-up of stagnant plasma. The enhanced stagnation point pushed the shock out directly below the anomalous region. That inflated shock surface is maintained further downstream by the enhanced anomalous field in the flank region. The polar magnetic field that drapes around the surface of the Moon is responsible for holding solar wind off the surface in the tail region and guiding it around the surface of the Moon. With the additional magnetic field in this region from the second dipole, there is a greater barrier between the solar wind and the lunar surface, causing the shock surface to form further from the surface.

With two dipoles present, the anomalous magnetic field strength can be reduced while still causing a mini-magnetosphere to form at or above 100 km from the surface. In Figure 5.1c the two dipoles have opposing orientations. The upper dipole moment points in the southward (-z) direction while the lower dipole moment points in the northward (+z) direction. They are also now closer to the surface and the strength of the field, relative to the surface field, falls off faster. The magnetic field is 20 nT at the surface half way between the 2 dipoles and 8.26 nT at 100 km above the midpoint. The field strength at 120 km above the lower dipole is 7.5 nT. These values are much closer to measured values, particularly at 100 km above the surface, and less than the

minimum magnetic field magnitude for which a shock would form with only one dipole present in the previous simulations [25].

The outer shock surface in Figure 5.1c at its maximum height above the surface is 140 km, when above the lower dipole. The upper dipole does little to hold plasma off the surface directly above its location, but it enhances the deflection of plasma by the lower dipole. The magnetic field from the upper dipole connects to the lower dipole field, expanding the lateral extent of field lines parallel to the IMF. Fluid below the upper dipole and above the lower dipole can not impact the surface because of the magnetic field running tangential to the surface. This holds the plasma off the surface in the region between the two dipoles, and inflates the size of the mini-magnetosphere.

When only the direction of the dipole moments in Figure 5.1c are flipped by 180° , the mini-magnetosphere changes shape and the height of the shock surface decreases (Figure 5.1d). The high point of the shock is 96 km above the surface. The dipole with a moment anti-parallel to the IMF is primarily responsible for deflecting the solar wind since the surface field will be parallel to the IMF. Thus the decrease in shock height is primarily due to the smaller surface field strength at the dipole in the $+\vec{z}$ direction (i.e. top dipole). But it is also due to how the two dipoles combine to deflect the plasma. The surface field at the lower dipole reconnects with the IMF, eroding the anomalous field and creating cusp-like structures that allow the plasma access to the surface. Most of the plasma that is deflected by the top dipole, travels downward where it can either interact with the plasma held off the surface by the lower dipole, creating the stagnation point, or impact the surface.

If the relative dipole field strengths in Figure 5.1d are reversed such that the surface field at the upper dipole is 400 nT and 100 nT at the lower dipole, but the dipole orientation remains the same, a shock forms 156 km above the upper dipole. The dipole with the moment in the $+\vec{z}$ direction remains the strongest dipole. The shock is round like the shock in Figure 5.1c, and no stagnation point forms above the lower dipole. The larger field strength at the upper dipole, relative to the lower dipole, means that the upper dipole deflects most of the plasma before it interacts with the lower dipole. Even with the smaller surface field, when compared with the cases in

Figures 5.1c and 5.1d, this case forms the highest shock height due to a slower fall-off of the field. The field strength at 100 km is approximately 18 nT, as opposed to 12 nT in cases 5.1c and 5.1d.

The slower fall-off in field strength leads to an increase in the lateral extent of the parallel surface field. In Figure 5.1c, the anomalous magnetic field is roughly parallel to the IMF for 222 km around the lower dipole. In Figure 5.1d, the lateral extent of parallel anomalous field around the upper dipole is only 187 km. The lateral extent is 226 km when the surface field in Figure 5.1d is 400 nT at the upper dipole and 100 nT at the lower dipole. It is this increase in lateral extent that causes inflation.

5.4 Four Dipoles

When four dipoles are present on the surface, alternating dipoles are needed to create an anomalous magnetic field that is on the order of 300 nT at the surface and less than 10 nT at 100 km. This indicates that higher order moments are necessary to accurately model the magnetic field in region of plasma interaction. The largest surface fields with the fastest fall-off are for dipoles with moments aligned mostly parallel to the surface.

In all of the four dipole simulations, the top dipole and the one second from the bottom are at the same location as the dipole pairs in the Figures 5.1c and 5.1d. The dipole field strengths and orientations are listed in Table 5.2.

The maximum shock height in Figure 5.2a is 144 km. The field configuration creates a mini-magnetosphere similar in size and shape to both the case with 2 alternating dipoles in Figure 5.1c and a single dipole with the moment anti-parallel to the direction of the IMF. But in the case of the single dipole, the field strength at 100 km was 3 times larger, while the maximum shock height was only 40 km higher. The dipole moments of the two inner dipoles are aligned, creating a cumulative field that is dipole in nature. The 2 dipoles on the outer edges reconnect in such a way as to enhance the lateral extent of the field from the 2 inner dipoles. The cusp-like structure

Figure	Dipole Moment	Surface Field (nT)	Field at 100 km (nT)
5.2A	-z	205	6.34
	+z	223	13.8
	+z	185	14.0
	-z	229	14.6
5.2B	-z	354	11.2
	+z	399	16.0
	-z	390	2.71
	+z	388	14.5
5.2C	-x	135	5.12
	+x	150	11.2
	+x	118	11.4
	-x	155	11.9
5.2D	+r	111	7.00
	-r	186	13.7
	-r	75	16.2
	+r	124	14.0

Table 5.2: 4 dipoles: Dipole parameters for the results in Figure 5.2. All the dipoles in 2A-2C are buried 26.1 km below the surface. The radial dipoles in 2D are buried between 28 and 43 km below the surface. The directions of the dipole moments are parallel to the horizontal axis and entry velocity of the solar wind (\vec{x}), parallel to the vertical axis (\vec{z}) and the IMF ($-\vec{z}$) or a radial vector originating at the center of the Moon (\vec{r}). The dipoles are listed in decreasing z position and increasing x , thus the first dipole listed in each case is the dipole closest to the top of the simulation box, and conversely, the last dipole listed is closest to the bottom of the box.

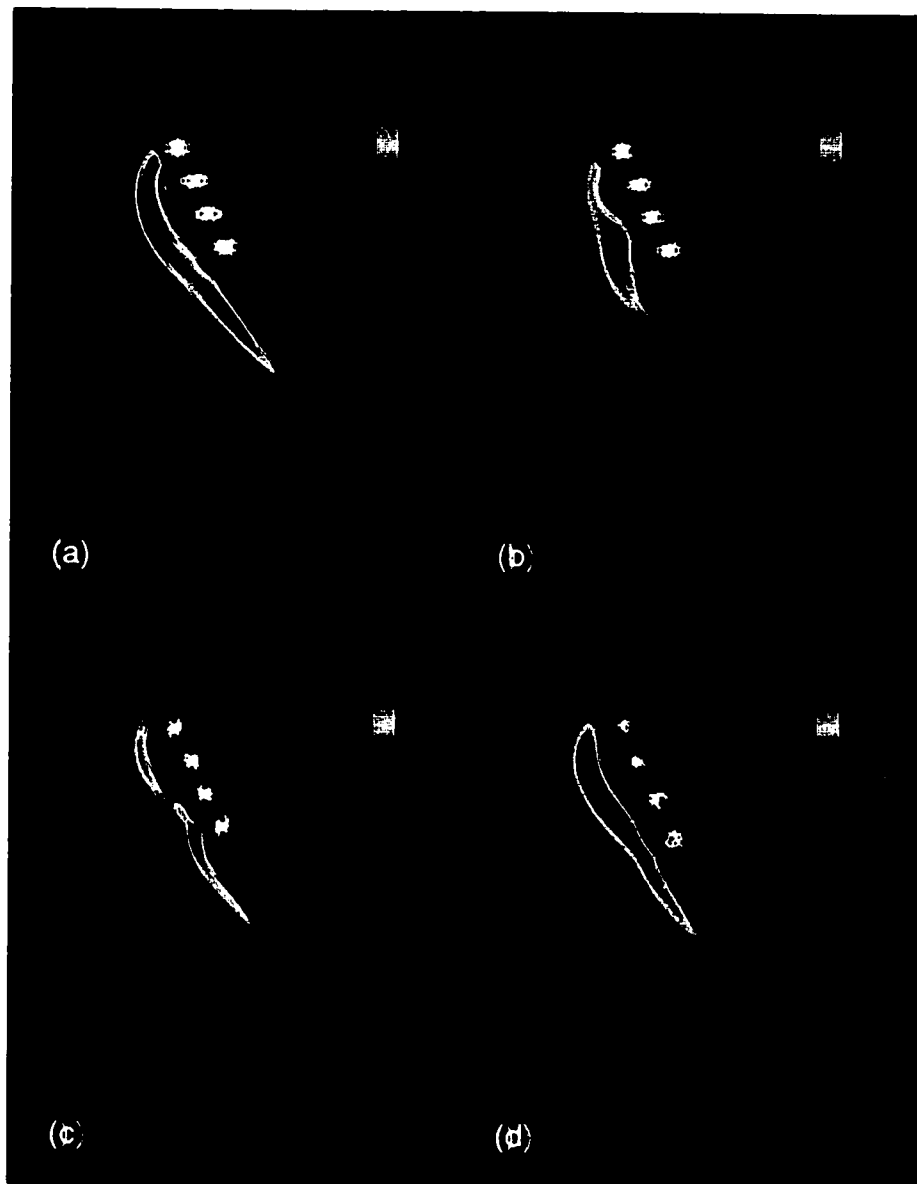


Figure 5.2: 4 dipoles: The figures are all of the same form as in Figure 5.1. The dipole configurations are defined in Table 5.2. The inner dipole moments in (a) are in the $+z$ direction while the outer dipoles in the $-z$ direction. Each dipole in (b) is 180° rotated from its neighboring dipoles. The middle dipoles in (c) are in the $+x$ direction while the outer dipole moments are in the $-x$ direction. The dipoles in (d) are radial, alternating between $+r$ and $-r$. The sharp kinks in the magnetic field lines in (d) are due to numerical uncertainties in calculating the magnetic field lines for dipoles not aligned with one of the axes.

that forms around the bottom dipole allows plasma access to the surface. Thus the pressure and density do not build up as much as in the surrounding areas.

When no dipole moments are in the same direction as the neighboring dipoles (Figure 5.2b), the resulting shock is similar to the case with dipole moments parallel to the IMF (Figure 5.1b). But unlike the case with the parallel dipoles, the tail in Figure 5.2b does not flair out. The maximum shock height is 157 km in a region downstream of all the dipoles.

The stagnation point in Figure 5.2b comes about from the interaction of the two dipoles oriented in the $+z$ direction. The top dipole reconnects with the dipole just below to increase the lateral scale, while dipole second from the top deflects the solar wind down toward the other dipoles. The bottom dipole deflects not only the solar wind but also the plasma directed downward by the upper dipoles, with some of the deflected plasma being directed upward where it stagnates and inflates the shock surface.

The stagnation point is not directly between the two dipoles in the $+z$ direction due to the orientation of the dipole between them. The orientation of the middle dipole is in the $-z$ direction leading to reconnection of the surface field to the IMF and allowing ambient plasma access to the surface, thereby reducing the build-up of pressure and density in that region.

When the alternating dipoles are perpendicular to the IMF, the shape and size of the shock surface (Figure 5.2c) is very similar to the shock in Figure 5.1d. The reason for this is the alignment of the anomalous field with respect to the IMF. The anomalous field between the top two dipoles is parallel to the IMF, just like the surface field for a dipole moment anti-parallel to the IMF (cf the upper dipole in Figure 5.1d). The anomalous field between the two lower dipoles is anti-parallel to the IMF, as it would be opposite a dipole moment parallel to the IMF. Thus the direction of the surface fields are similar in both Figure 5.1d and Figure 5.2c.

The maximum shock height (opposite the upper 2 dipoles) in Figure 5.2c is 96 km above the surface with a stagnation point forming downstream, just as in the case with two dipoles. But in the case with 4 dipoles, the stagnation point forms further downstream (192 km, instead of 140 km) and causes the formation of a second bump in the

shock surface due to larger density and pressure in the stagnation point.

Another difference is that the magnitude of the magnetic field in the case with 4 dipoles is significantly smaller than in Figure 5.1d, 2 - 4 times smaller at the surface and 20% - 40% smaller at 100 km above the surface. With two extra dipoles, the shock surface remains approximately the same size even though the magnitude of the magnetic field has been reduced. The field strength is smaller but the anomalous field is extended over a larger area leading to increased deflection of the solar wind, enhancing the shock region.

The maximum pressure and density at the stagnation point in Figure 5.2c are 20% larger than the values at the stagnation point in Figure 5.1d due to the magnetic field geometry above the lower dipoles. In Figure 5.1d, the magnetic field of the two dipoles, when combined, does elongate the magnetic field above the surface in the region between them. But when the upper dipole deflects the solar wind down into the bottom dipole, the solar wind can still impact the surface above the lower dipole due to the cusp-like regions that form. Thus plasma will build up, but not to the extent it would if the reconnected magnetic field completely blocked access to the surface. With a denser concentration of dipoles in Figure 5.2c, the solar wind that is deflected around the upper 3 dipoles has decreased access to the surface in the region between the bottom dipole and the one above it.

When the dipoles are in a radial direction (Figure 5.2d), similar to the horizontal orientation in Figure 5.2c, the maximum shock height is 135 km above the surface. The resulting magnetic field line geometry is similar to the horizontal orientation but the shock is 40 km higher for the radial dipoles. The shock around the radial dipoles is also 40 km higher than the shock in Figure 5.1d even though the magnitude of the magnetic field at the surface is considerably smaller in Figure 5.2d. The key difference is the slower fall-off of the total magnetic field with respect to the surface field for the radial dipoles (Table 5.2), leading to a total field strength at 100 km that is comparable to those in Figure 5.1d.

The size and shape of the shock surface is heavily controlled by both the fall-off of the anomalous field and the size of the anomalous region. Since the magnetic field

above the surface does not decrease with altitude as rapidly in Figure 5.2d as it does in Figure 5.2c, the plasma is deflected further above the surface, pushing the shock out. And the increase in size of the magnetized region from that in Figure 5.1d, leads to a larger region over which the solar wind is deflected, also inflating the shock height.

5.5 Summary

Mini-magnetospheres can be supported by magnetic anomalies near the lunar surface. Modeling the anomalous field with multiple dipoles leads to weaker fields above the surface but flow around the dipoles still leads to a bow shock forming well above the lunar surface. Inflation of the mini-magnetospheres is therefore not the result of an increase in the magnitude of the total field strength but rather an increase in the lateral extent over which the anomalous field occurs and the inhibited fluid flow that results. Plasma flowing around one dipole can encounter another dipole instead of freely flowing around the surface of the Moon or impacting the surface. As a result the plasma is slowed, causing stagnation and inflation. Thus mini-magnetospheres will form with smaller field strengths than previously estimated with only one dipole.

Modeling the anomalous region with alternating multiple dipoles not only creates a total field that falls off faster with altitude due to the presence of higher order moments, it also increases the lateral extent of the anomalous region. When the magnetic anomaly is modeled with four dipoles, the anomalous region is approximately 350 - 400 km in length. The large magnetic anomalies on the Moon are over 700 km in diameter [45].

These results indicate that the higher order moments of the anomalous magnetic field not only contribute to deflecting the solar wind, they are largely responsible for determining the shape of the resulting mini-magnetosphere. And configurations with the similar magnetic field magnitude can produce mini-magnetospheres with vastly different sizes and shapes, since the direction of the resulting magnetic field configuration relative to the IMF is as important as the interaction between individual dipole fields.

While reduced from the single dipole approximation, the anomalous magnetic fields

at 100 km above the surface in the multi-dipole simulations is still larger than the ~ 2 nT measured by Lunar Prospector [*L.L. Hood*, private communication, 2001]. The next step in the investigation will be to extend the model to a full 3D simulation. With all three spatial dimensions, a more realistic model of the extended anomalous regions can be incorporated into the simulations.

Chapter 6

3D MPD SIMULATIONS OF THE MOON

3D simulations allow for a more realistic treatment of the solar wind flow around an obstacle. Plasma can flow around the sides of the obstacle, not just over the poles or be absorbed by the surface, as in the 2D and 2.5D simulations. 3D simulations also allow for greater complexity of the anomalous magnetic field source region, as well as placement of the magnetic anomalies at locations other than facing directly into the solar wind.

3D fluid simulations of the solar wind interacting with a magnetized region on the Moon indicate that, like the 2D simulations, IMF configurations that allow for reconnection to the anomalous magnetic field will cause the greatest variability in the size and shape of the resulting mini-magnetosphere. For an anomaly created with a single dipole, the mini-magnetospheres are very similar in both size and shape to those that formed in the 2D simulations. 3D simulations suggest more erosion of the anomalous magnetic field through reconnection to the IMF, as well as inflation of the flank regions due to decreased solar wind impact. The 3D simulations also indicate that localized anomalies can have global effects on the wake region with the most modification occurring when the anomaly is comprised of multiple dipoles. Multiple dipole configurations result in complex bow shocks and magnetic field geometries that have symmetry neither in latitude nor longitude. And changes in the orientation of the dipole moments in the 3D multiple dipole simulations leads to greater variability in the shape of the resulting mini-magnetosphere in comparison to the multiple dipole 2D simulations.

6.1 Model and Initial Conditions

The 3D simulations numerically solve Equations 2.1 - 2.4 but now the derivatives are taken in all three dimensions. The electric field equation has the same form as in Equation 2.15 and the value of the ratio $c/(\omega_{pi}L)$ remains equal to 0.10, as in the 2.5D simulations in Chapter 4 and 5. The 3D simulations contain 4 nested grids. The resolution ranges between 205 km in the largest grid to 25.6 km in the smallest grid. The surface conditions are identical to the 2D simulations with the Lunar resistivity equal to 10^4 ohm m, and the density set to 0.1 Ar^+ ions cm^{-3} on the day side and 0.01 on the night side. The 3D simulations are still a single ion population fluid code so an Ar^+ ion is treated as 40 H^+ ions, thus the effective number density on the day side is 4.0 cm^{-3} , and 0.4 cm^{-3} on the night side.

The magnitude of the IMF was set to no more than 5 nT, with a single component in the IMF no larger than 3 nT. B_z is perpendicular to the ecliptic plane, B_y is in the ecliptic plane but perpendicular to the solar wind velocity, and B_x is parallel to the solar wind bulk velocity.

The magnetic Reynolds number associated with the numerical resistivity is on the order of 1000 outside of the Lunar surface, indicating that convection still dominates and numerical diffusion is minimal. The dipole field was generated using the 3D dipole formula for an arbitrary orientation. Additional dipoles were added to generate higher order terms, creating a total magnetic field that falls off faster than a single dipole, as well as creating more realistic magnetic field geometries that have some of the same complexity as Lunar Prospector measurements suggest.

6.2 Single Dipole Magnetic Field Simulations

When the IMF is in the southward direction and parallel to the anomalous magnetic field at the surface, the IMF drapes over the surface field creating a bubble that protects the surface. Figure 6.1 shows the ion density just above the surface and the magnetic field lines for both southward and northward IMF. Underneath the bubble created by the draping IMF (Figure 6.1a), the density is equal to 4.0 ions cm^{-3} , the

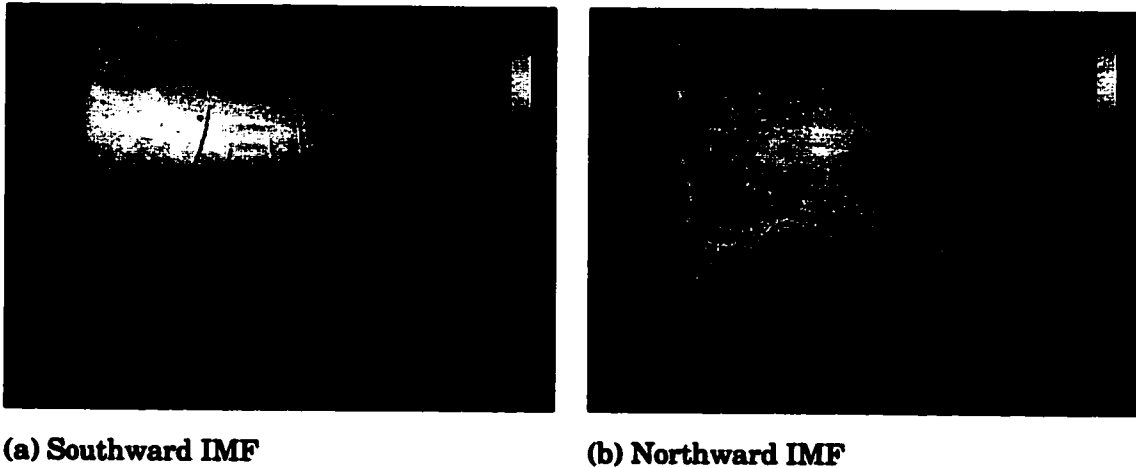
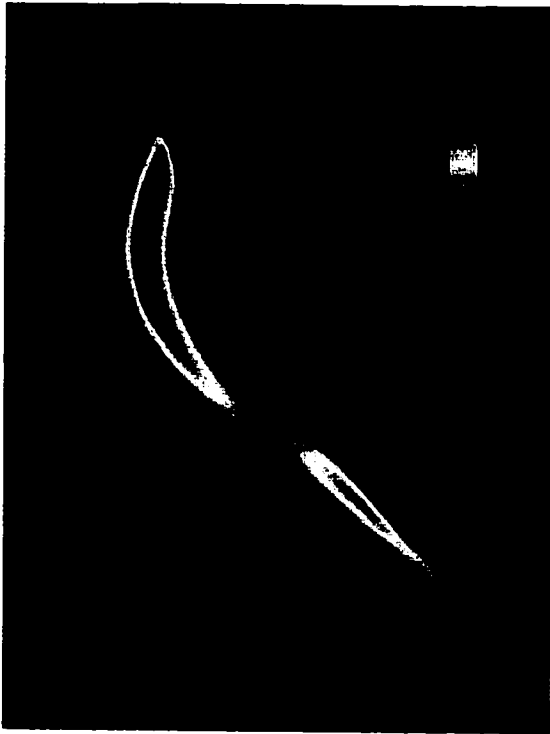


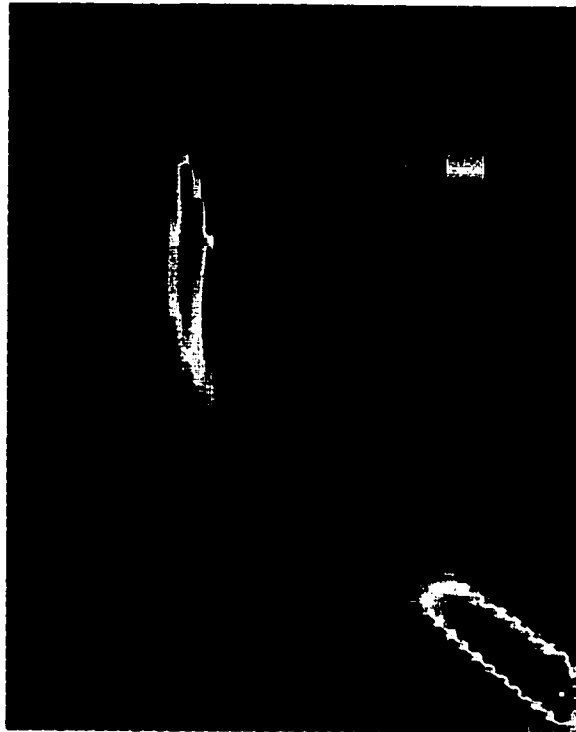
Figure 6.1: Near surface density and magnetic field lines for southward and northward IMF in the 3D simulation. The density is shown at 40 km above the surface. The moment of the buried dipole is in the $+z$ (pointing up) direction, thus the IMF and the anomalous field at the surface are parallel in (a) and anti-parallel in (b). Regions where the density is dark blue indicate regions that are protected from the solar wind.

same as the Lunar surface density. The draped magnetic field prevents solar wind access to portions of the surface. But the entire region is not completely protected. Reconnection at the bottom of the mini-magnetosphere creates a cusp-like region due to a neutral line in the total magnetic field that funnels solar wind to the surface. Enhanced solar wind impact also occurs where the draped IMF contacts the surface above the magnetic bubble.

When the anomalous magnetic field at the surface and the IMF are anti-parallel (Figure 6.1b), reconnection to the IMF erodes the anomalous magnetic field. But a region is still protected from the solar wind, the region that the solar wind is funneled into the previous case. In the Northward IMF case (Figure 6.1b), reconnection of the IMF to the anomalous magnetic field leads to only open field lines above the anomaly. The solar wind is directed toward the surface in this region, as seen by the parabolic shaped region of high density north of the draped magnetic field lines. This is where the bow shock contacts the surface. The mini-magnetopause is instead supported by the draped magnetic underneath the dipole.



(a) 2.5D simulation



(b) Cut through center of 3D simulation grid

Figure 6.2: 2D vs 3D - IMF and dipole moment anti-parallel: Density for the (a) 2.5D simulation and (b) through the center of the mini-magnetosphere in the 3D simulation, when the IMF and dipole moment are anti-parallel. The magnetic field line configuration for the resulting 3D mini-magnetosphere is shown in Figure 6.1a. The area shown in (a) is 1201 km by 1610 km, while (b) shows an area 1203 km by 1613 km. The resolution in (a) is 8.7 km and 25.6 km in (b). Both images have been smoothed slightly to reduce pixilation.

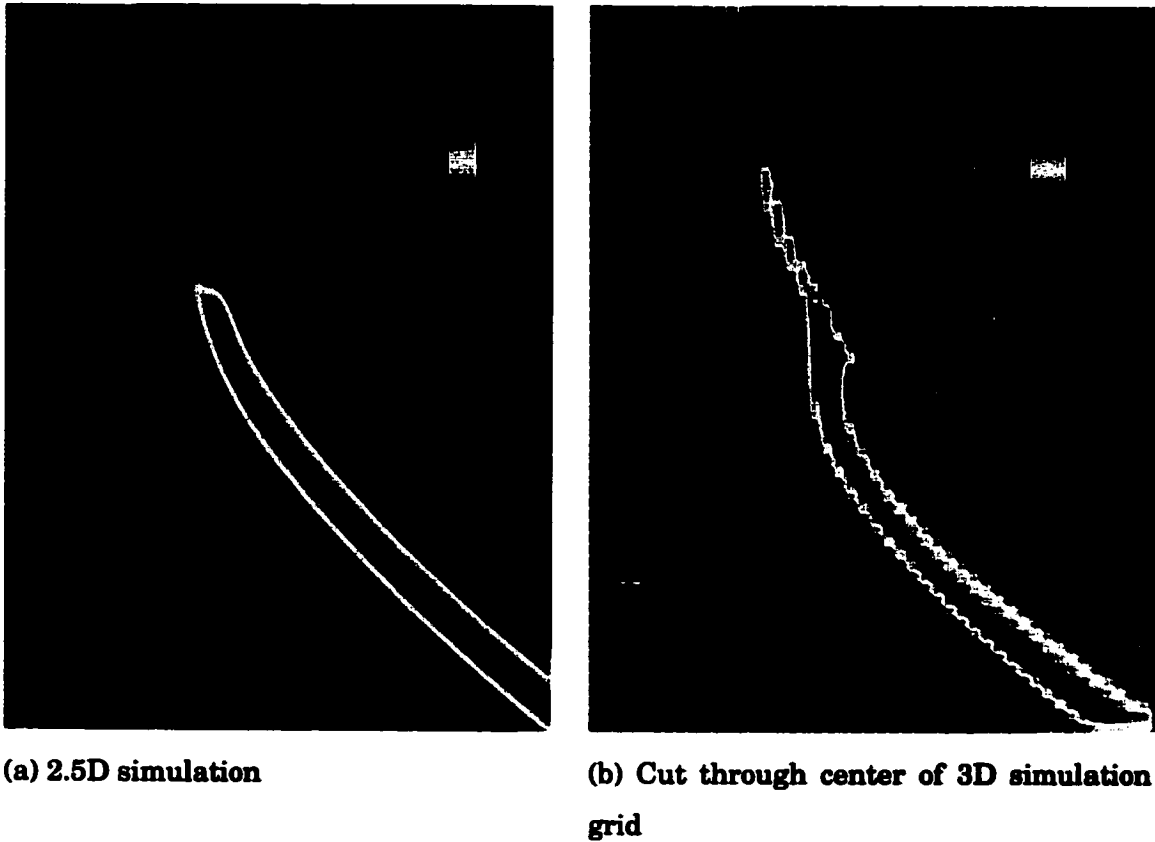


Figure 6.3: 2D vs 3D - IMF and dipole moment parallel: Density for the (a) 2.5D simulation and (b) through the center of the mini-magnetosphere in the 3D simulation, when the IMF and dipole moment are parallel. The magnetic field lines for the 3D case are shown in Figure 6.1b. Each figure is to the same scale and size as those in Figure 6.2.

Comparison of the results from the 2D simulations and cuts through the 3D simulations show that for similar initial conditions, the 2D and 3D simulations produce similar results. Figures 6.2 and 6.3 show the density for the 2.5D simulations and in the plane through the middle of the dipole for the 3D simulations. In Figure 6.2 the dipole moment is anti-parallel to the IMF and is identical to the case in Figure 6.1a, while in Figure 6.3, the IMF and dipole moment are parallel like in Figure 6.1b. In the 2D case in Figures 6.2a and 6.3a, the effective dipole moment is approximately 50 km below the surface, and identical in strength and position to the configuration in the simulation shown in Figure 4.9. The 3D dipole in Figures 6.2b and 6.3b is approximately 75 km below the surface. The anomalous magnetic field directly opposite the anomaly is on the order of 250 nT at the surface and 50 nT at 100 km above the surface.

The general shape of the mini-magnetospheres is the same for 2D and 3D simulations. When the IMF is in the same direction as the anomalous field at the surface, it drapes over the anomaly creating a rounded mini-magnetosphere (Figure 6.2). The stagnation point in the downstream region still forms in the 3D case, and is the location of the highest density, but not the largest pressure. In both the 2D and 3D case the shock forms approximately 200 km from the surface, with a peak density near 40 cm^{-3} . Downstream from the anomaly in the tail, the surface of the mini-magnetosphere forms further from the surface in the 3D simulations than in the 2D simulations.

The outer edge of the tail region forms further from the surface in the 3D simulations due to the fact that in 3D, plasma can flow around the flanks of the Moon. In the 2D simulations the solar wind is primarily deflected down around the shock surface and into the flank region, causing additional compression of the shock surface. As the solar wind encounters the 3D mini-magnetosphere and is deflected, it can go up or down, like in the 2D simulations, or it can go around the sides. As there are more routes for the solar wind to be deflected, it will not compress the tail regions as much, thus the shock surface in the tail will be inflated.

When the IMF and the surface field are anti-parallel, the surface field is eroded by

the the IMF. The 3D nature allows for even more erosion than the 2D case, as is seen by the absence of a bubble in the density above the anomaly in Figure 6.2, in addition to the lack of closed magnetic field lines directly above the dipole in Figure 6.1b. Instead a bubble forms where the magnetic field lines are perpendicular to the surface, below the cusp. In the tail region, the upper edge of the shock is approximately 275 km from the surface in the 3D case and 145 km in the 2D case. Like the previous case, the tail regions flairs out more from the surface in the 3D simulations due to the reduced solar wind flow into the flank region.

A $\pm B_y$ component to the IMF acts to erode the anomalous magnetic field when B_z is negative (southward IMF), resulting in a smaller magnetic field bubble and more solar wind access to the surface. But when B_z is positive (northward IMF), a B_y component reduces erosion of the anomalous field directly above the anomaly, while enhancing erosion in the tail. As a result, the draping of magnetic field in the flank region is reduced, increasing solar wind access, but more closed field lines are present directly above the dipole, creating a semi-protected region like that which appears in the southward IMF case. When only the B_x (in the same direction as the solar wind velocity) component of the IMF is non-zero, the size and shape of the mini-magnetosphere is very similar to when no IMF is present. This is identical to the behavior of the mini-magnetosphere in the 2D simulations, where the B_x component of the IMF was shown to have no effect on the mini-magnetosphere.

6.3 Global Effect for a Single Dipole

When the magnetic anomalies face into the solar wind, the resulting mini-magnetospheres create global effects which can be seen as modifications in the size of the wake. The wake region is shown for when no magnetic anomaly is present (Figure 6.4a) and when a buried dipole is present for southward (Figure 6.4b) and northward (Figure 6.4c) IMF. Figure 6.4d shows the wake when the anomaly is composed of three dipoles and will be discussed in the next section. The isosurfaces are for 4 different density levels, with the blue-green and purple surfaces below the solar wind density of 10 cm^{-3} , thus indicating the wake region.

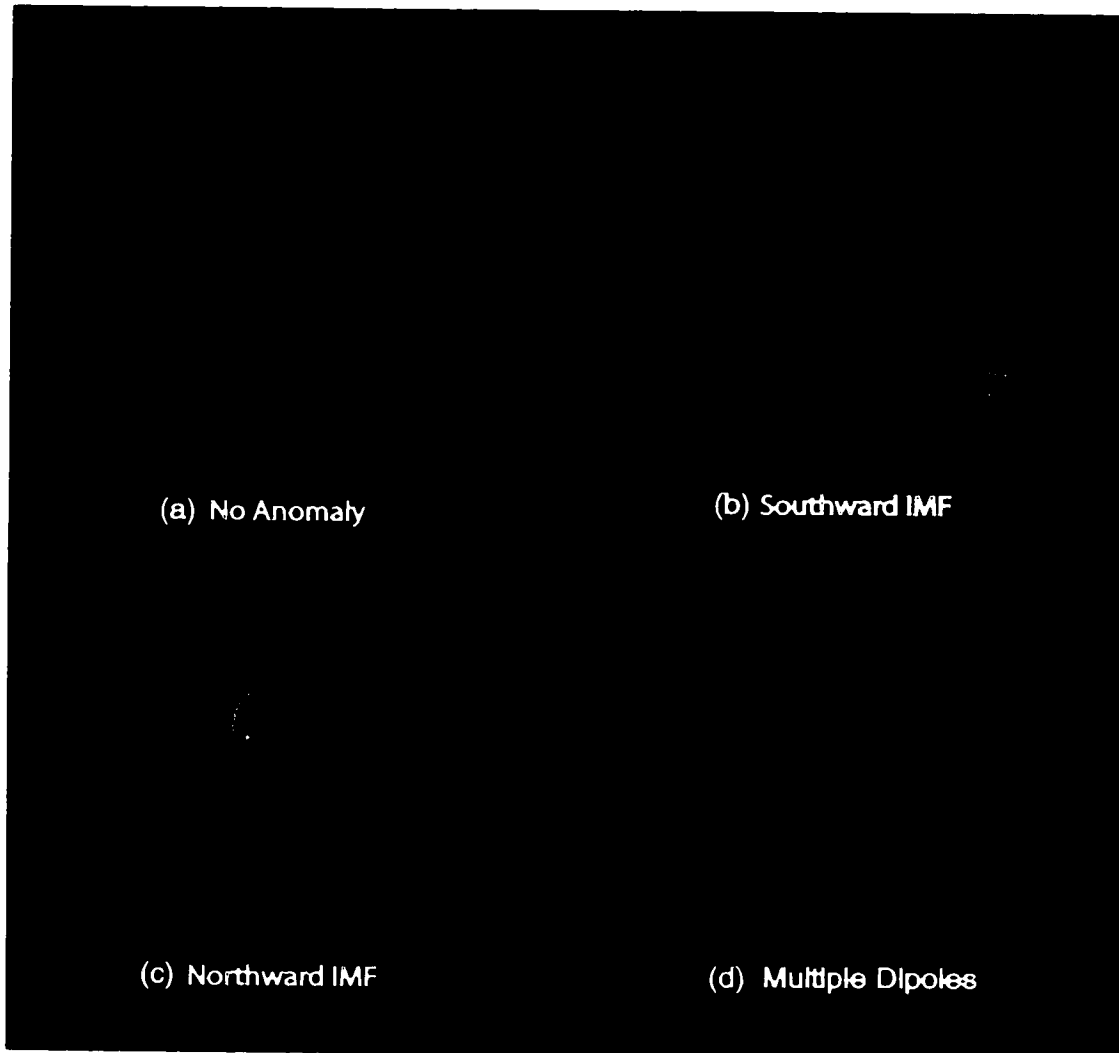


Figure 6.4: The wake region for four different cases. Density isosurfaces in the wake region from a mostly back view, when (a) no magnetic anomaly is present and the IMF is in the northward direction, (b) a single dipole is present with southward IMF, (c) a single dipole is present with northward IMF, and (d) three dipoles are present with northward IMF. The wake in (b) is for the same simulation as in Figure 6.1a while the wake shown in (c) for the simulation in Figure 6.1b. The simulation shown in (d) is the same as in Figure 6.5b. The isosurfaces are at 13 ions cm^{-3} (red), 11 ions cm^{-3} (yellow), 8 ions cm^{-3} (blue-green), 4 ions cm^{-3} (purple). The silver sphere represents the surface of the Moon.

In the previous section the tail of the mini-magnetospheres is shown to flair out more in the 3D simulations. This flaring can also be seen to cause global structures. In Figure 6.4c the yellow isosurface not only flairs out on both sides, it is also asymmetric in how much it flairs on each side. Both the yellow and blue-green isosurfaces are further from the center of the wake on the east side of the wake. The asymmetry is due to the convection electric field which points in the east (or -y) direction. The yellow isosurface flairs out more in both the east and west direction for southward IMF than for northward IMF because for southward IMF, the mini-magnetosphere presents a bigger obstacle for the IMF to run into and the orientation of the anomalous magnetic field is such that the IMF has to slide around the sides as opposed to reconnecting to the surface magnetic field.

The presence of a magnetic anomaly causes the wake to compress, regardless of the orientation of the IMF. This can be seen in the narrowing of the purple density isosurface in Figures 6.4b and 6.4c compared to when no anomaly is present (Figure 6.4a). The compression is most dramatic for northward IMF case, where at a position 5120 km downstream from the center of the Moon, the wake narrows by 350 km along the ecliptic and 460 km along the midnight meridian with respect to when no anomaly is present. In the southward IMF case, the wake narrows by 100 km along the ecliptic and 150 km along the meridian at the same position downstream.

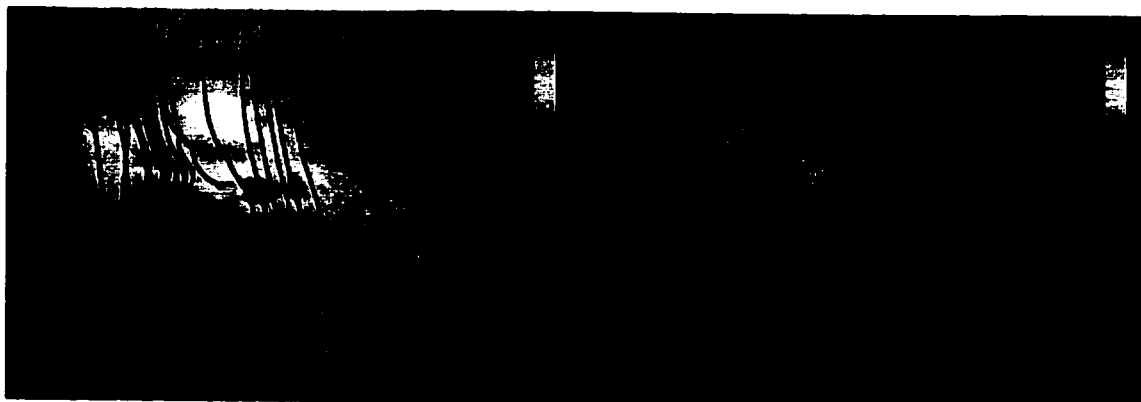
The wake is compressed for both cases with an anomaly due to the higher pressures and densities associated with the bow shock of the mini-magnetosphere. While the pressure and density in the tail region are not as high as directly opposite the anomaly, they are higher than the pressure and density adjacent to the wake when no anomaly is present. The bulk velocity of the plasma is also reduced downstream as the solar wind is slowed by the mini-magnetosphere, allowing the solar wind plasma to convect in further to the wake region. The reduced velocity also means that the IMF on the back side is bent back at a sharper angle. These bent field lines also define the location of the wake. The wake is not as compressed for the southward IMF case because the tail region flairs out more, i.e. the yellow isosurface is further from the center of the wake in Figure 6.4c. Thus the higher density and pressure regions will be further

from the center of the wake, resulting in less compression.

6.4 Multiple Dipole Magnetic Field Simulations

No global model for all the Lunar magnetic anomalies currently exists. This is due to both the strength of the anomalies and the amount of data available. At 100 km above the surface, the anomalous magnetic field is on the order of only a few nanotesla. This is comparable to the background magnetic field when the Moon is in tail region of the Earth's magnetosphere, thus the error associated with the vector magnetic field measurements is too large for the measurements to be useful as input for generating a global magnetic field model. Magnetic field measurements were made at lower altitudes as Lunar Prospector spiraled in for its impact into the Lunar surface and ambient anomalous magnetic fields were measured, but this data is limited in coverage [*L.L. Hood, private communication, 2001*]. The surface magnetic fields are large compared to the background noise but those measurements are only of magnetic field magnitude, not vector magnetic field, and thus can not be used either in generating a magnetic field model. Thus a more complex magnetic field geometry associated with true magnetic anomalies is approximated with multiple dipoles. The higher order moments associated with either a multiple dipole approach or a global magnetic field model were shown to be very important in determining the size and shape of a mini-magnetosphere in Chapter 5.

When the magnetic anomaly is modeled with more than two dipoles the resulting shock surfaces and magnetic field line configurations are much more complex than a single dipole. The anomaly in Figure 6.5a is created using three dipoles, two dipoles side by side with moments in the $-z$ direction and one above the other two with a moment in the $+z$ direction. This configuration contains the opposing dipole configuration that maintained the mini-magnetospheric size while reducing the total magnetic field in the 2D results in Figures 5.1c and 5.1d. The third dipole adds an increase in longitudinal scale size not possible in the 2D simulations. The largest magnetic field magnitude at 100 km is on the order of 50 nT, still an order of magnitude larger than measured values.



(a) 3 dipoles in z direction

(b) 3 dipoles in various orientations

Figure 6.5: 3 dipoles and Northward IMF: The magnetic field lines and density at 40 km above the surface for an anomaly modeled with (a) 3 dipoles in the z direction (two in the -z and one in the +z direction) and (b) 3 dipole in various orientations (one dipole in the +z direction, one in the -z, and the third in the -y direction). The anomalous magnetic field at the surface is on the order of 450 nT at the strongest regions and 50 nT opposite the anomalies at 100 km in (a) and 10 nT in (b). The IMF is in the northward direction.

The anomaly in Figure 6.5b is created with three dipoles in the exact same locations as in the previous case, but with the orientation and magnitude of one dipole altered. The upper dipole with a moment in the +z direction remains the same with the same relative strength. The right most dipole in the -z direction also remains the same. Just the left most dipole is rotated to the -y direction and the magnitude is reduced by half. This adds a variation to the configuration in Figure 6.5a that could not be added in the 2D simulations, namely a dipole moment in the $\pm y$ direction. Also the resulting magnetic field strength at 100 km in on the order of 10 nT, comparable to the magnitude measured by Lunar Prospector. The magnetized region at the surface is approximately 540 km wide by 460 km high in Figure 6.5a and 360 km wide by 310 km high in Figure 6.5b. Both anomalous regions are approximately a factor of two smaller than the anomalous regions at the Imbrium and Serenitatis antipodes.

Neither configuration completely protects the surface from the solar wind as seen for single dipole anomalies, but a mini-magnetosphere still forms, even for the reduced

magnetic field magnitude configuration. The shock surfaces are not symmetric and as such the semi-protected regions, where the density is less than the solar wind density, are not in the center of the anomaly. The region with the lowest surface density in Figure 6.5a is above the strongest dipole of the three. The moment of that dipole is anti-parallel to the IMF, and thus the anomalous field at the surface and the IMF are parallel the rounded magnetic field lines similar to the bubble seen for a single dipole in Figure 6.1a. An extended cusp region forms due to a parabolic shaped line where the magnetic fields from the two lower dipoles in the $-z$ direction meet the magnetic field from the upper dipole in the $+z$ direction. The magnetic field from all three dipoles is directed towards the surface along the entire line, instead of a single spot, allowing an extended region where the solar wind has access to the surface.

The magnetized region in Figure 6.5b is not protected from solar wind at all. The dipole that provided most of the protection in Figure 6.5a has been rotated and reduced. The anomalous magnetic field causes pileup of the solar wind but doesn't not deflect it away from the surface. The lower left dipole in the $+y$ direction twists the total magnetic field and leads the impact of the solar wind primarily on the upper left side. The total magnetic field is directed toward the surface along a diagonal line inbetween all three dipoles and increased access of solar wind occurs in the region, but cusp-like magnetic field lines do not form. The anomalous magnetic field directed toward the surface is comparable to the IMF thus the resulting magnetic field configuration is mostly tangential to the surface but kinked where the combined dipole fields are radial mostly radial.

Even though the solar wind is not completely deflected from the the surface by multiple dipole anomalies, it is still modified enough to create a mini-magnetosphere. The maximum height of the outer edge of the mini-magnetosphere is approximately 190 km in Figure 6.5a and 140 km in Figure 6.5b. The density and pressure enhancements at the mini-magnetosphere in Figure 6.5a are on the order of 3.4 and 65, respectively. The pressure and density of the plasma do not build up as much in the mini-magnetosphere in Figure 6.5b providing the solar wind increased access to the surface and reducing the altitude at which the shock surface forms from the sur-

face. The maximum density on the order of 2.6 times the solar wind density and the corresponding maximum pressure on the order of 50 times the solar wind pressure.

The multiple dipole mini-magnetospheres are not as effective at deflecting the solar wind in the anomalous region as the single dipole mini-magnetosphere, but they still have an effect on the size of the wake. When the wake diameter is measured at the same location, 5120 km downstream from the center of the Moon, as the single dipole cases, the wake diameter is 770 km narrower is for the case with 3 aligned dipoles in Figure 6.5a. For the simulation shown in Figure 6.5b, compression of the wake is the most dramatic, the diameter narrowing by nearly 1600 km and is shown in Figure 6.4d. The multiple dipole configurations reduce the size of the wake by increasing the longitudinal size of the mini-magnetosphere. This creates a larger obstacle for the solar wind, further slowing the solar wind and increasing the convection of the plasma into the wake region, reducing the size of the wake.

6.5 Discussion

The 3D single dipole simulations show that the 2D simulations do a good job of determining the size and shape of mini-magnetospheres when the anomalies face into the solar wind. The 3D simulations indicate that reconnection of the IMF to the anomalous magnetic field is more effective at eroding the surface field than predicted by the 2D simulations. But this does not necessary mean that the 3D simulations predict smaller mini-magnetospheres. The contrary is actually true, as deflection of the solar wind around the sides of the mini-magnetosphere is important in reducing the compression of the tail region. In the 3D simulations, less solar wind is deflected downward, thus the tail region of the shock surface is inflated relative to the results for the 2D simulations.

The magnetic field geometry at the surface is crucial for determining access of the solar wind. 3D multiple dipole simulation produce mini-magnetospheres with more variability in shape with respect to the mini-magnetospheres in the 2.5D multiple dipole simulations in Chapter 5 due to the added longitudinal degree of freedom. As a result, changes in the orientation of the dipoles used to create the anomalies cause

more change in the shape of the resulting mini-magnetosphere. In two cases shown, the dipoles creating the anomalous region are at identical locations, but the resulting mini-magnetospheres are completely different due to a change in a single dipole orientation and relative strength. An extended cusp can form in the region where the magnetic field of all the dipoles pointed toward the surface, but the nature of the cusp depends on the total magnetic field configuration. Increased access to the surface may occur in regions where the magnetic field is partially tangential to the surface.

Even though the magnetic anomalies are small in comparison to the size of the Moon, they can create large scale effects. All single dipole generated magnetic anomalies cause modification of the wake, but multiple dipole configurations have the largest impact on the size of the wake. The mini-magnetospheres slow the solar wind over an extended region and that region is largest for the multiple dipole configurations. This slow plasma can convect further into the wake region.

Even with 3 dipoles, the magnetic anomaly still does not truly capture the fundamental nature of the magnetic field geometry of the magnetic anomalies. High resolution magnetic field maps of the surface field and maps of the magnetic field magnitude at 100 km suggest that the source for Crisium antipode anomaly is fairly coherent [*L.L. Hood, private communication, 2001*]. Those same maps indicate that the Imbrium antipode anomaly is actually a collection of several sources, and as such the magnetic field in the region is very incoherent. Thus attempting to model the entire Imbrium antipode region with a collection of a few dipoles is not appropriate. The coherence of the Crisium antipode region though, does lend to approximating the magnetic field with the sum of a few dipoles. The multiple dipole simulations suggest that the deflection of the solar wind will occur at the Crisium antipode. But with such variability, making predictions about the behavior of the solar wind at the Lunar anomalies is difficult without a more accurate model of the magnetic anomalies. In the two multiple dipole cases with such different structure, neither case completely prevents solar wind access to regions of the surface. Thus, unless anomalous regions contain partially dipolar magnetic fields, the magnetic anomalies will reduce the space weathering of the surface, but not completely eliminate it.

Chapter 7

3D MPD SIMULATIONS OF MARS

2D MHD simulations for Mars never achieved steady-state. This is inherent to the 2D nature of the simulation. Since Mars has an atmosphere thick enough to stand-off the solar wind, the IMF can not readily diffuse through the planet, and instead must reconnect to a planetary magnetic field and/or slide around the flanks. This third degree of freedom that allows transport of plasma and magnetic field round the obstacle does not exist in a 2D simulation, and created an unphysical pile-up of plasma and magnetic field.

The 3D fluid simulations of the solar wind interaction with Mars presented here show agreement with measured locations for the bow shock and with the MPB location above the unmagnetized regions as calculated by *Vignes et al.* [72]. The simulations predict the formation of a magnetopause-like structure surrounding the strongest magnetic anomalies in the southern hemisphere. This mini-magnetopause forms inside the pre-existing bow shock, on the order of 40% higher in altitude than the magnetic pileup boundary. The pressure enhancement associated with the mini-magnetopause is strongest when the IMF is in the B_z direction, but still present for IMF in B_y and B_x . The anomalies can also increase the scale height of the atmosphere by inhibiting the impact by solar wind that compresses and erodes the atmosphere, creating a region protected from the solar wind. The simulations show that associated with the magnetic pile-up boundary is non-ideal MHD behavior by the ions, thus the non-ideal MHD portion of the model is required for understanding the physics of the inner magnetosphere.

The simulations also show that the magnetic anomalies create asymmetries in the density and pressure in the tail region. When the IMF is in the B_y direction, this modification of the plasma is the strongest when the anomalous region is located either

on the dawn side or the night side. The asymmetries are further enhanced when the density of the plasma at the planetary boundary on the night side is reduced relative to the day side density. The anomalous magnetic field modifies the fluid flow creating semi-protected regions with reduced density and pressure, and regions of enhanced density and pressure where the plasma is deflected to and stagnates.

7.1 Model

The 3D simulations numerically solve Equations 2.1 - 2.4, using the extended Ohm's Law (Equation 2.15). But Mars has a substantial atmosphere, thus the gravitational term becomes important and Equations 2.2 and 2.3 become:

$$\frac{\partial \mathbf{m}}{\partial t} + \nabla \cdot \left(\frac{\mathbf{m} \mathbf{m}}{\rho_m} \right) + \nabla P = \mathbf{J} \times \mathbf{B}^{\text{tot}} + \rho_m \mathbf{g}(\mathbf{r}) \quad (7.1)$$

$$\frac{\partial e}{\partial t} + \nabla \cdot \left(\frac{\mathbf{m}}{\rho_m} (e + P) \right) = \mathbf{E} \cdot \mathbf{J} + \mathbf{m} \cdot \mathbf{g}(\mathbf{r}) \quad (7.2)$$

where $\mathbf{g}(\mathbf{r})$ is the gravitational vector and equal to

$$\mathbf{g}(\mathbf{r}) = (-3.71 \frac{\text{m}}{\text{s}^2}) * \left(\frac{\mathbf{r}}{r} \right) \quad (7.3)$$

where \mathbf{r} is the distance vector from the center of the planet and r is the radius from the center of the planet. The other variables have their standard meaning as defined in Chapter 2. The ratio $c/(\omega_{pi}L)$ in the extended Ohm's Law is still equal to 0.10.

The resistivity of the surface is set to 10^3 ohm m, which is in the range of 10^3 to 10^5 ohm m set by *Tang et al.* [69] for Martian rocks and by *Sonnet* [68] for Lunar rocks. The non-zero resistivity allows for diffusion of magnetic field through the planetary surface, preventing any unphysical pile-up of magnetic field. The magnetic Reynold's number inside the planet is on the order of 1. As the IMF interacts with the Martian ionosphere and can slip around the sides before ever contacting the Martian surface, the IMF interaction inside of Mars is reduced compared to the IMF interaction inside the Moon. Therefore the diffusion of IMF through Mars is reduced relative to the diffusion of the IMF through the Moon. Thus the resistivity of Mars can be reduces while not causing unphysical pileup of the IMF and a non-steady state solution. The

Reynold's number associated with numerical resistivity is on the order of 200 in the solar wind and 2000 near the anomalies, thus diffusion is negligible outside of the planet.

The solar wind density is equal to 4 ions cm^{-3} , with a bulk speed of 400 km s^{-1} and the IMF equal to 1 nT. In the results shown below, the IMF has only one component equal to 1 nT; B_z is perpendicular to the ecliptic plane, B_y is in the ecliptic plane but perpendicular to the solar wind velocity, and B_x is parallel to the solar wind bulk velocity. Having only one component non-zero allows the tracking of which components of the IMF cause the greatest response by the plasma to the interaction of magnetic anomalies with the solar wind.

The Viking 1 lander measured O_2^+ to be the dominant ion species below about 325 km, with CO_2^+ dominating above 350 km. The density of O_2^+ at 300 km was measured to be approximately 200 cm^{-3} [22]. The planet boundary is defined as 300 km above the surface with a number density equal to $100 \text{ O}_2^+ \text{ cm}^{-3}$ and a temperature of 3000 K. The maximum O_2^+ density of 10^5 cm^{-3} occurs at 130 km from the surface [22]. As this model is a single ion species model, an O_2^+ ion is treated as 32 H^+ ions. There are also no mechanisms for loss at the planetary boundary, and setting the boundary at a lower altitude, and thus a higher density, did not produce a steady state solution.

The equations are solved on a nested grid system that allows for high resolution in a small area of interest. In all the results presented, 3 grids were centered about the equator and noon meridian. The resolution of the finest grid is equal to 108.7 km, and 434.9 km in the coarsest grid.

The model of the Martian magnetic field was provided by *Cain et al.* (2003). Maps of the magnetic field magnitude and radial component of the magnetic field at 400 km from the surface (and 100 km above the simulation boundary) are shown in Figure 7.1. It is in the radial component of the magnetic field that the lineations measured by Mars Global Surveyor (Figure 1.5) can be seen. The simulations were run with the strongest anomalies pointing into the solar wind, pointing down the tail, on the dawn or the dusk side.



Figure 7.1: The simulated Martian magnetic field at 400 km from the surface. The magnetic field magnitude is shown in (a) and the radial component of the model Martian magnetic field in (b) over the southern hemispheric portion of the planet with the strongest anomalies. The magnetic field is given in nanotesla. From the model provided by *Cain et al.* [5].

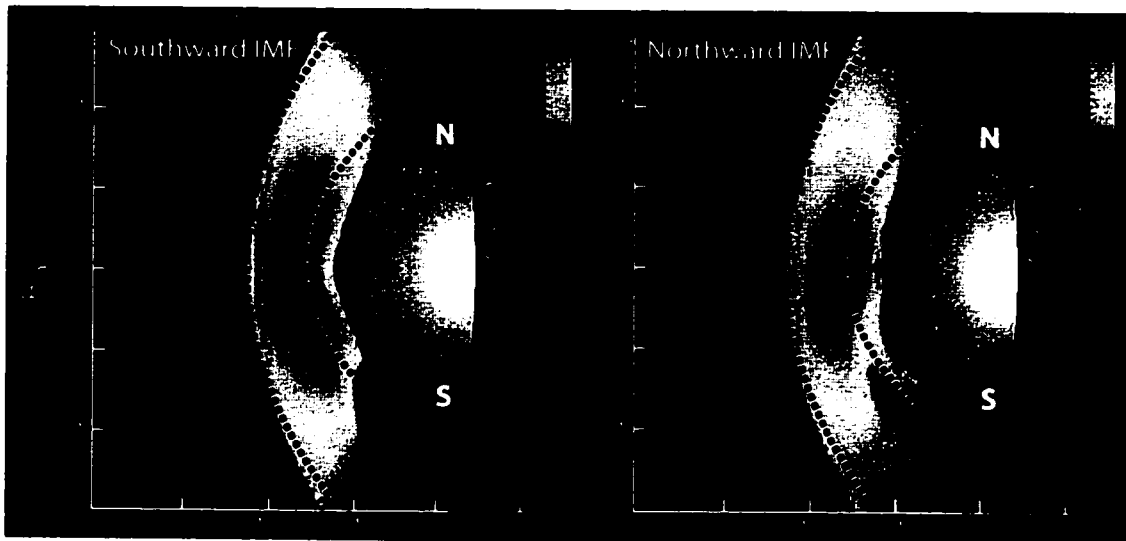


Figure 7.2: The pressure in the plane running through the noon meridian for both (a) southward and (a) northward IMF. The black contour lines are drawn at the values of 0.214, 0.353, and 0.470 nPa. The silver sphere represents the inner boundary of the simulations at an altitude of 300 km and has a radius equivalent to 3697 km. The plane shown contains an area 7285 km by 10330 km, with a grid resolution of 109 km. The black and white curves indicate the position of the bow shock and magnetic pileup boundary as calculated by *Vignes et al.* [72].

7.2 Northward vs. Southward IMF

A subsolar point of the bow shock forms at approximately $0.6R_M$ for the southward IMF case, and about 100 km (or one grid point) further out for northward IMF. Figure 7.2 shows the pressure in the noon-midnight meridian for both north and southward IMF, with the black and white curves indicating the position of the bow shock and magnetic pileup boundary (MPB) as calculated by *Vignes et al.* [72]. They used 450 bow shock crossings and 488 MPB crossings from Mars Global Surveyor to produce the fits. As such, the fits produce an average over a range of solar wind conditions, not the position for one particular solar wind condition. The average distance of the subsolar point of the bow shock for the fits to the data is $0.64 \pm 0.08R_M$ from the surface. In addition to the fact that the position from MGS is an average, the discrepancy between the measured and simulation bow shock shape could be due to both the lower density

used for the planetary boundary and the lack of loss mechanisms at the boundary.

For a solar wind Mach number of 10 and γ (the ratio of specific heats) equal to $\frac{5}{3}$, the theoretical density enhancement at a bow shock should be by a factor of 3.88 and 125 for the pressure enhancement [56]. At the subsolar point in the simulation results, the density and pressure enhancements are equal to 3.5 and 130 respectively for the southward IMF case and 3.45 and 125 respectively for the northward IMF case.

The fits by *Vignes et al.* [72] put the position of the magnetic pileup boundary at $0.29 \pm 0.04 R_M$ from the surface at the nose and is indicated by the inner black and white curve in Figure 7.2. The MPB can not be seen in the pressure plots. This is expected as the MPB is not a region of pressure balance. But a magnetopause-like pressure boundary can be seen in the southern hemisphere above the location of the magnetic anomalies.

The magnetic pileup boundary can be seen in the simulation magnetic and electric field components. A magnetic pileup boundary forms for any comet-like (thick atmosphere, no magnetic field) object in the solar wind. As the IMF runs into a high conductivity ionosphere, the magnetic field will not be able to diffuse through the ionosphere and will begin to pileup and slide around the sides of the obstacle. Figures 7.3 and 7.4 show the magnitude of the magnetic field and the electric field vectors in the noon meridian. The component of the electric field out the plane has been set to zero for clarity. The MPB can be seen as an increase in the magnetic field strength by an order of magnitude. The electric field in the northern hemisphere indicates that more than IMF pileup is occurring at the MPB.

Associated with the MPB is an electric field pointing away from the surface, in the same direction as the electric field at the bow shock. The electric field at the bow shock is due to solar wind ions penetrating further into the shock as a result of their larger momentum, thus creating an electric field pointing into the solar wind and is captured by the ∇P_e term in Equation 2.15. The direction of the electric field vectors indicates that at the MPB there is an excess of electrons or deficit of ions in comparison to the region just below. This could be the result of the ions traveling further into the atmosphere than the electrons, which would occur if the ions experience the same

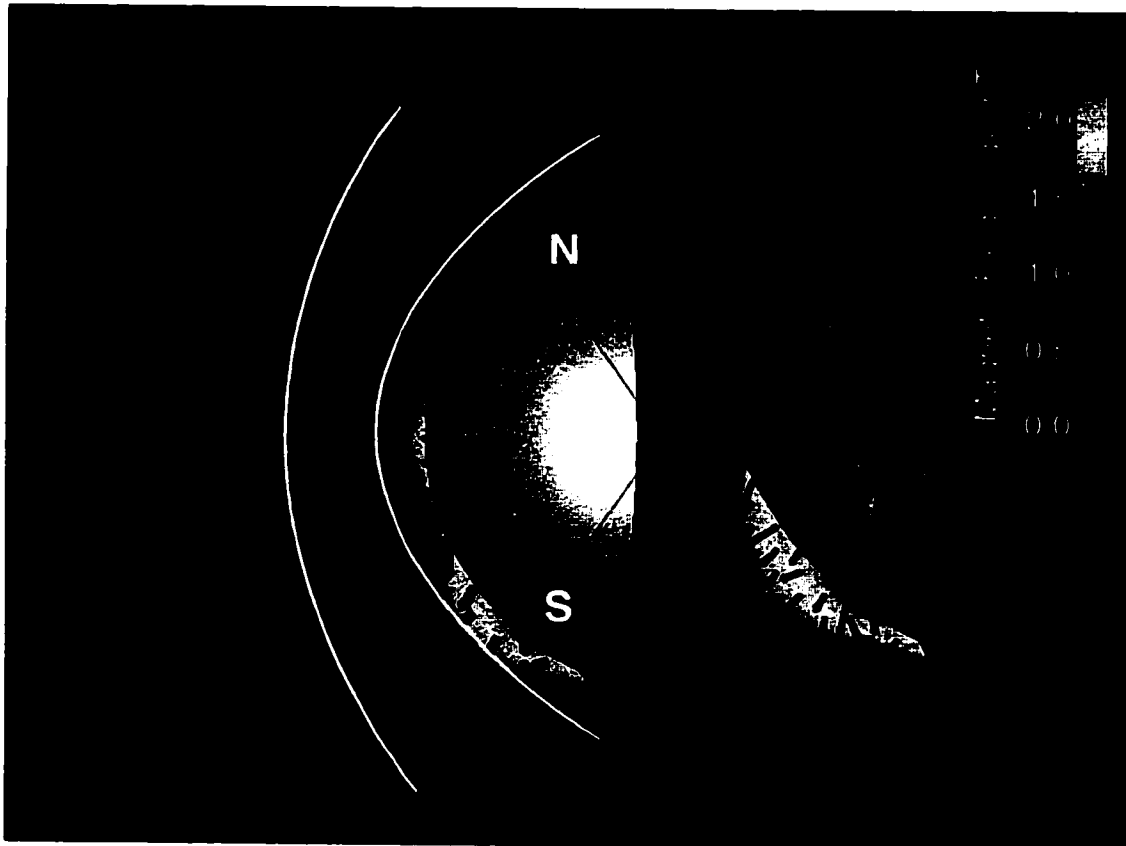


Figure 7.3: Electric and Magnetic Field - South IMF: The electric field vectors and the magnitude of the magnetic field in the plane running through the noon meridian for southward IMF. The component of the electric field out of the plane has been set to zero for clarity. The maximum electric field vector size is equal to 0.37 mV/m and vectors with a magnitude below 0.015 mV/m were set to zero. The plane showing the magnetic field encompasses an area 7285 km by 10330 km. The silver sphere represents the inner boundary of the simulations at an altitude of 300 km and has a radius equivalent to 3697 km. The white curves indicate the average positions of the bow shock and MPB as calculated by *Vignes et al.* [72].

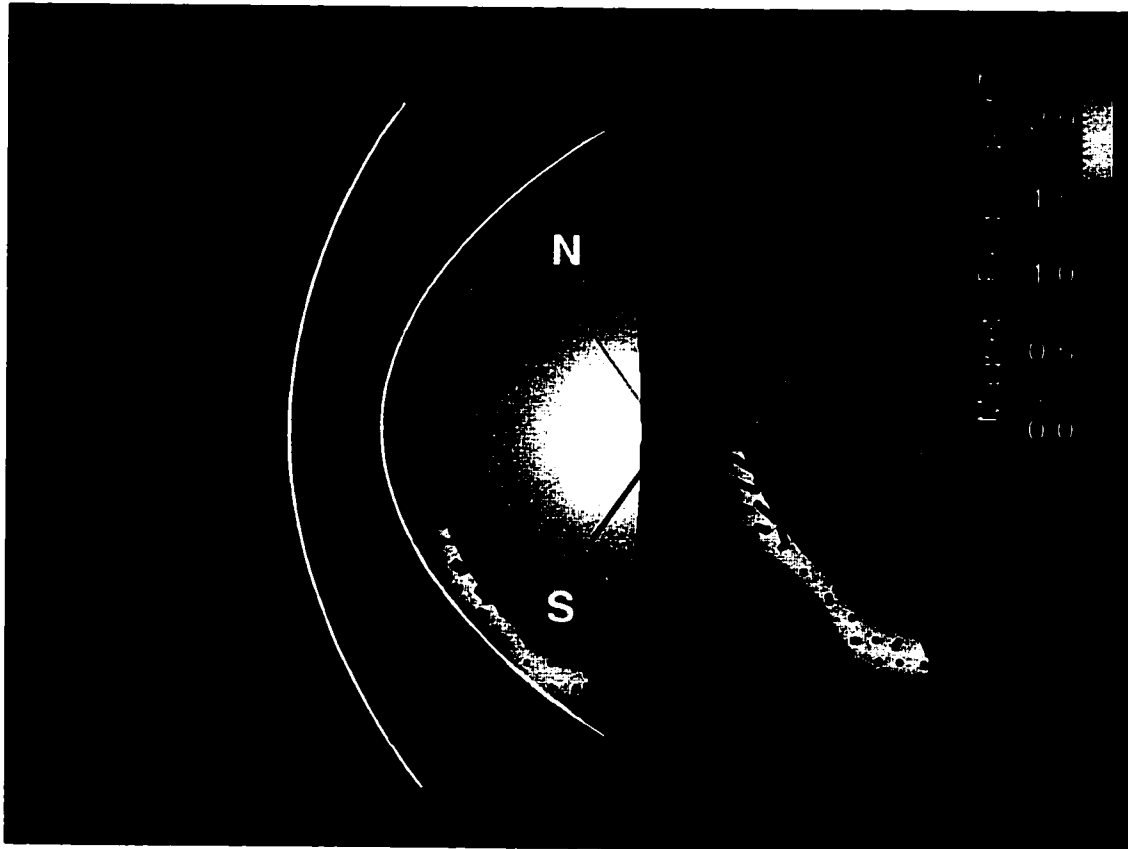


Figure 7.4: Electric and Magnetic Field - North IMF: The electric field vectors and the magnitude of the magnetic field in the plane running through the noon meridian for northward IMF. The maximum and minimum vector sizes are identical to those in Figure 7.3, as is the size of the area plotted.

momentum filtering that occurs at the bow shock, or the ions becoming demagnetized through a mechanism such as small angle scattering collisions that do not change the bulk trajectory of the solar wind.

The electric field helps determine which mechanism is occurring. The charge separation at the bow shock is the result of a pressure gradient, while demagnetization is the result of non-ideal MHD behavior. At the MPB, the Hall term ($\mathbf{J} \times \mathbf{B}$) in Equation 2.15 is responsible for the direction and magnitude of the electric field in the xz plane. The Hall term indicates the occurrence of non-ideal MHD behavior; the same was seen in the comparison between particle and fluid simulations for the Moon in Chapter 4.

The Hall term in the electric field acts as current diversion, but the $\frac{c}{\omega_{pi}L} \mathbf{B}$ in $\mathbf{J} \times \frac{c}{\omega_{pi}L} \mathbf{B}$ can also be thought of as an anomalous resistivity. The difference from the typical resistive term, $\eta \mathbf{J}$, is that the anomalous resistivity for the Hall term is orthogonal to the current. As the magnetic field piles up, the conductivity of the ionosphere is large so the magnetic field does not diffuse and the electrons will remain frozen to the magnetic field and will pile up as well. But the conductivity is not infinite, due to the anomalous resistivity associated with the Hall term, and the ions will travel further across the boundary. Resistivity comes about through collisions. Thus the large Hall term suggests that collisions become important at the MPB. Due to collision, the ions could become demagnetized and continue to penetrate further into the Martian ionosphere, unlike electrons that remain tied to the magnetic field, generating an electric field pointing away from the surface.

The mini-magnetopause that forms in the southern hemisphere can be seen in the pressure as well as the electric and magnetic field. The boundary forms around $0.4 R_M$, as measured radial out from the the strongest anomalies ($0.41 R_M$ for southward IMF and $0.38 R_M$ for northward IMF), about 40% higher than the MPB would form. At the magnetopause boundary, the Hall term is still larger than the pressure gradient term in the electric field equation, but now the pressure gradient is comparable in magnitude to the Hall term, unlike at the MPB where the pressure gradient term is small and mostly constant across the boundary.

The electric field vectors change direction going across the magnetopause boundary

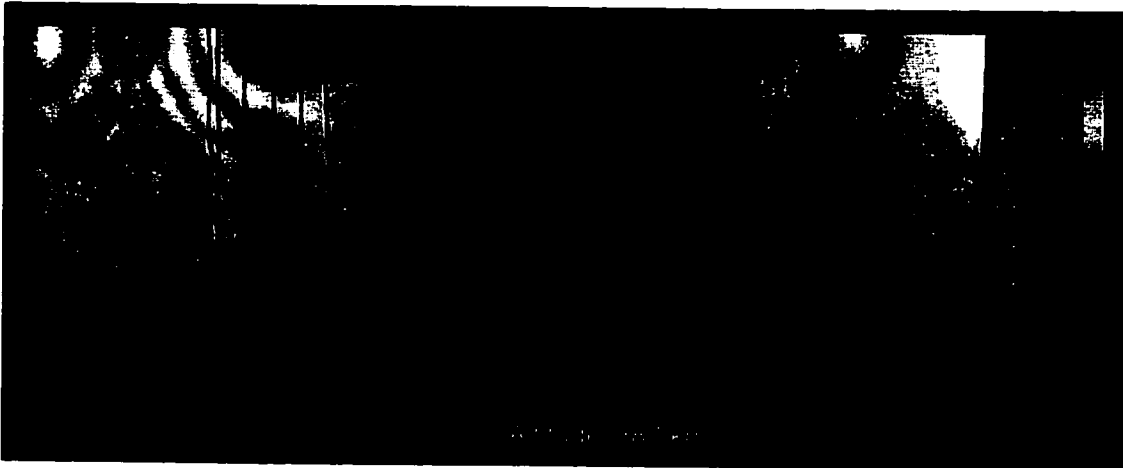


Figure 7.5: The effect of the anomalies on ionospheric scale height. The plasma density at a constant altitude of 387 km from the surface and the magnetic field lines as viewed from two different viewing angles for southward IMF. A higher density indicates a larger scale height for that region of the ionosphere.

(Figures 7.3 and 7.4). This is due to the change in dominance of the Hall and the pressure gradient terms. The Hall component of the electric field points away from the planet while the pressure gradient at the mini-magnetopause points both down and toward the planet. For southward IMF the pressure gradient term is non-zero throughout most of the region between the bow shock and the mini-magnetopause, while the hall component is only non-zero at the inner edge of the mini-magnetopause. The vectors flip direction as the Hall term becomes non-zero and larger than the pressure gradient.

The electric field vectors at the mini-magnetopause also change direction when IMF flips from southward to northward, as can be when comparing Figures 7.3 and 7.4. The Hall and pressure gradient components of the electric field still point in the same directions, but now the pressure gradient is stronger at the mini-magnetopause than for southward IMF. The magnetic field magnitude is also reduced at the outer edge of the mini-magnetopause due to reconnection of the IMF to the anomalous magnetic field.

Inside the magnetopause, the ionosphere is protected from the solar wind, leading

to a larger scale height. In Figure 7.5, the density at 387 km from the surface and magnetic field lines are shown for southward IMF. The density at the planetary boundary is constant and in all regions the density falls off with distance from the surface, but in the regions above the magnetic anomalies, the density is higher for a given radius, thus it falls off at a slower rate, translating into a larger scale height. The magnetic field in this region is tangential to the surface and dipolar-like. The magnetic anomalies inhibit the compression and erosion of the ionosphere. Using MGS data, *Mitchell et al.* [50] found that even over the weaker magnetic anomalies in the northern hemisphere, MGS had a higher probability of detecting only ionospheric plasma. But Figure 7.5 also shows that the anomalous magnetic field can also enhance solar wind access to the surface. The blue region indicates that the scale height is smaller than over the unmagnetized regions, thus the solar wind is being funneled into the that region by the anomalous magnetic field. This is due to a total magnetic field that is mostly radial. And comparing the northward and southward IMF cases shows that the regions that are protected from the solar wind for southward IMF configuration are not necessarily protected for northward IMF due to reconnection to of the anomalous magnetic field to the IMF.

The magnetic field lines in Figure 7.5 show that in some locations the dipolar structure of the magnetic field dominates. As the interaction region is well above the surface, due to the large ionospheric density, the higher order terms become less important than at the Moon, where the plasma interaction is close to the surface. Once the surface (ionospheric) density becomes comparable to the incident (solar wind) density, the interaction regions moves away from the surface and higher order terms become less important, but not unimportant.

When the strongest anomalies are pointed into the solar wind, the B_x component of the IMF plays no role in the formation of the mini-magnetospheres. The pressure and density of the plasma inside the bow shock is identical to when the IMF is equal to zero. The currents at the magnetopause are in the same direction as when no IMF is present but are magnitude of the vectors is larger when the IMF is in the B_x direction. The mini-magnetospheres at the Moon also show an insensitivity to B_x .

At Mars the parker spiral angle of the IMF is predominately in the $+B_y$ direction. When the simulations are run with the IMF set to 1 nT in the $+B_y$ direction, a mini-magnetopause forms around the southern magnetic anomalies, with the boundary layer forming around $0.38 R_M$ from the strongest anomalies. The pressure boundary is similar in shape to the case for southward IMF but the size is smaller. The region with the increased scale height in Figure 7.5 remains protected but the region with increased solar wind access for southward IMF, changes to having a slightly elevated scale height. While slightly different in shape when the IMF is in the $-B_y$ direction, the mini-magnetopause forms at the same height of $0.38 R_M$ and the protected regions are similar. Thus like the Earth, the B_z component of the IMF causes the greatest variability.

7.3 *Martian Magnetotail*

As Mars rotates with a 24.7 hour day, the anomalous regions will pass through different regions of the magnetosphere. Figures 7.6 and 7.7 show the percent change in density, with respect to when no anomaly is present, and streamlines of the plasma flow in the tail when the anomalous region is located on the night side (b), the dusk (c) or the dawn (d) sides. In all cases the IMF in the $+B_y$ direction. The density and change in density are shown in a plane parallel to the equatorial plane and intersecting the region of strongest magnetic field, as viewed from the south pole. The night side density at the planetary boundary is equal to the day side density. Figures 7.6a and 7.7a show the density and streamlines in the tail region when no anomaly is present. The percent change is calculated using the formula

$$\text{percent change} = \frac{(\text{with anomaly}) - (\text{no anomaly})}{\text{no anomaly}} \times 100 \quad (7.4)$$

When the southern anomaly is either partially or completely on the night side, the anomalous magnetic field creates a bubble that both reduces and increases the plasma density and pressure with respect to when no anomalous magnetic field is present. This plasma void around the anomalous region is most prominent in the pressure, but can still be seen in the density. As the plasma is reduced in the plasma void regions,

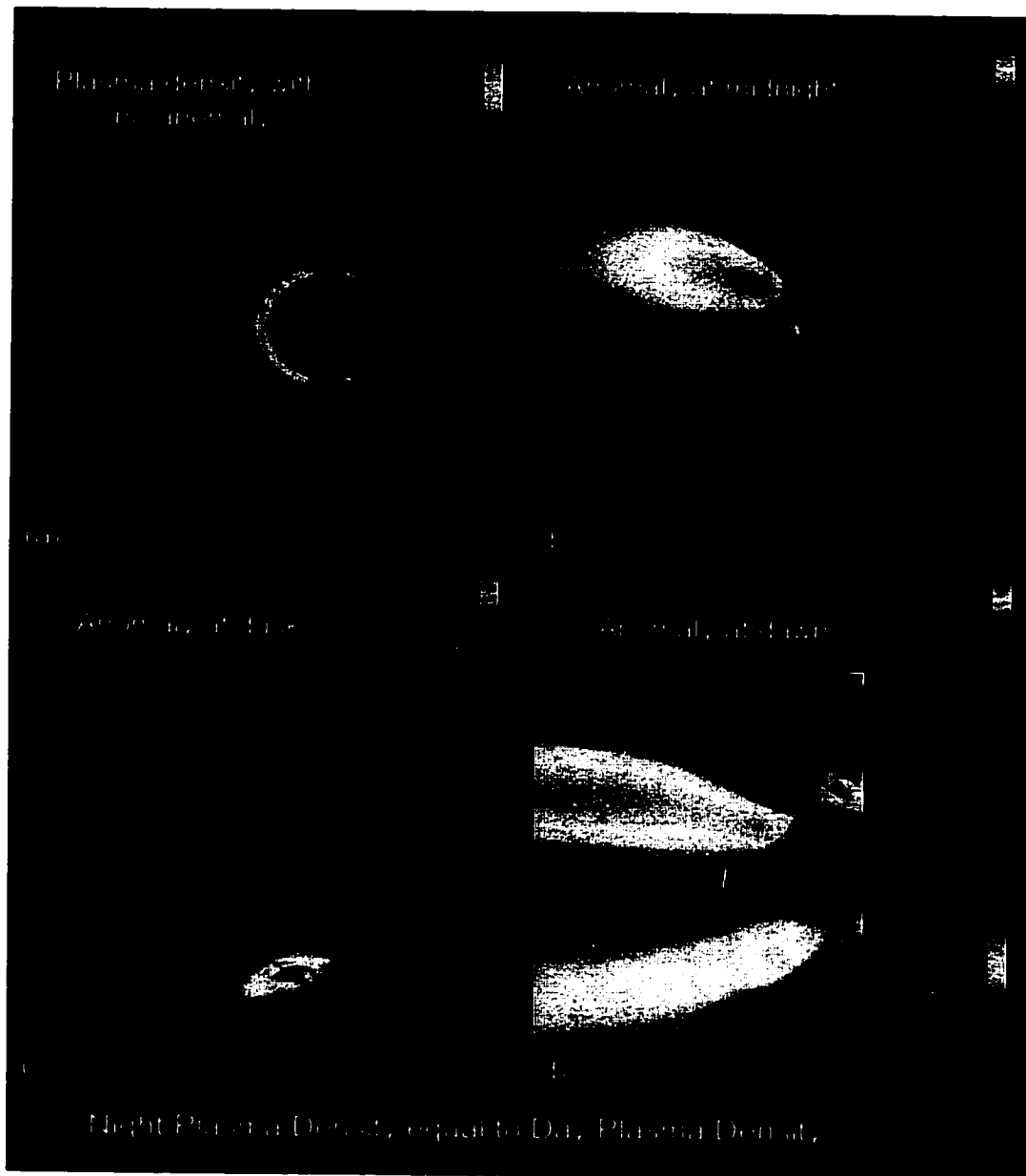


Figure 7.6: Nightside density percent difference: The density on the night side in a horizontal plane when (a) no anomaly is present and the percent change in the night side density relative to when no anomaly is present when the strongest anomalies are at (b) midnight, (c) dusk, and (d) dawn, as viewed from the south pole. The plane is parallel to the ecliptic plane but intersecting Mars at approximately 45° South. In all cases the IMF is equal to 1 nT in the $+B_y$ direction. The plane shows an area 15836 km by 19356 km inside the bow shock and magnetic field magnitude at the planetary boundary is mapped onto the sphere indicating Mars at an altitude of 300 km.

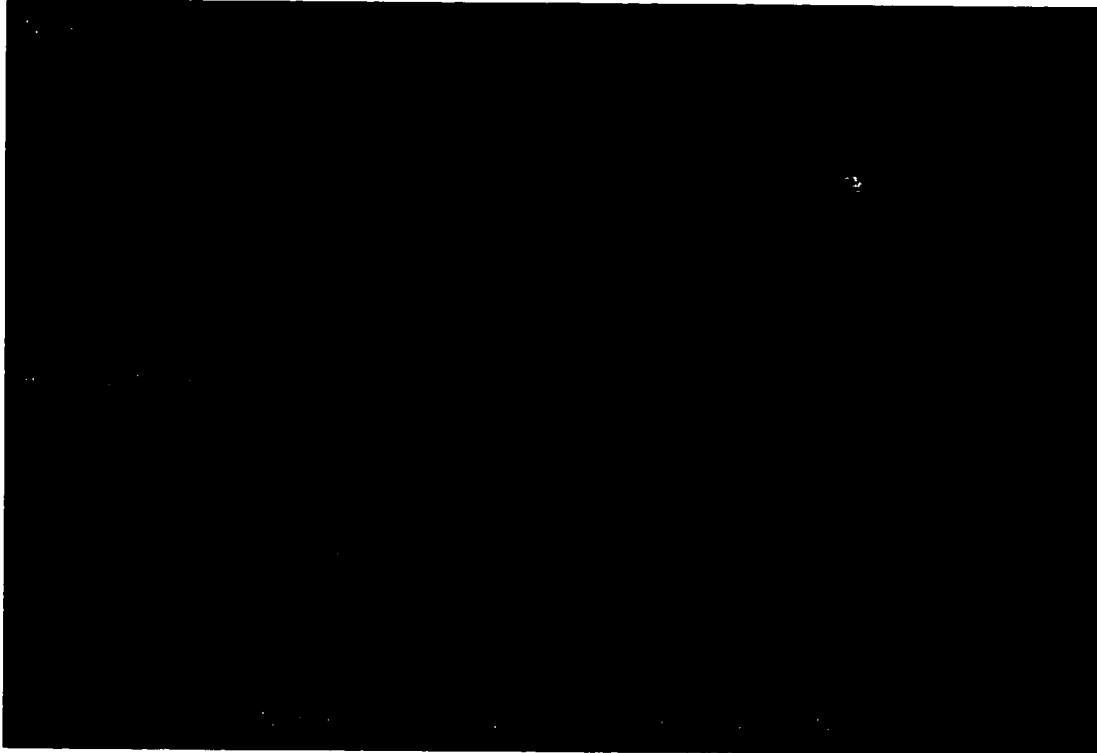


Figure 7.7: Streamlines around Mars for equal day and night side densities: Streamlines of the plasma flow around Mars as viewed from south pole for the night side density equals the day side density. The four cases shown are when (a) no anomalies are present, (b) the southern anomaly is on the night side, (c) the southern anomaly is in the dusk side and (d) the southern anomaly is on the dawn side. The orientation of the plots is identical to those in Figure 7.6. The streamlines over the south pole have are not shown for clarity.

associated with them are regions of high density and pressure.

The regions of low plasma pressure and density surrounded by regions of high density and pressure, are reminiscent of the flux spikes and plasma voids in MGS data (Figure 1.8 and *Mitchell et al.* [50]). A satellite traveling through the low pressure and density regions would measure a decrease in plasma flux while the magnetic field magnitude increases. The decrease of plasma in the simulation plasma voids is not nearly as strong as that shown in Figure 1.8, where the flux decreases by nearly two orders of magnitude from the nominal tail density. None of the simulation plasma voids show a decrease in density of even an order of magnitude smaller than the tail density when no anomaly is present. The scale size of both the measured and model plasma voids are comparable though. And the closed magnetic field lines in the plasma voids measured by MGS are seen at the simulation plasma voids as well.

The flux spikes measured by MGS had an energy spectrum similar to magnetosheath particles, and therefore plasma in the flux spikes would be much hotter than ionospheric plasma. The radial magnetic field geometry suggests the presence of field lines once connected to the solar wind. Neither of these characteristics are seen at the regions of enhanced plasma in the simulation. The plasma streamlines and temperature profiles indicate that the density and pressure enhancements are stagnation points. Also the flux spikes shown in Figure 1.8 have scale sizes on the order of 300 km, much smaller than the stagnation points.

With no solar UV flux, the night side ionospheric density is greatly reduced. *Mitchell et al.* [50] contend that when the anomalous magnetic field is on the night side it can prevent the refilling of ionospheric plasma, either from the day side ionosphere or the solar wind, into the mini-magnetosphere region. To approximate this, the night side ionospheric density and pressure were reduced by an order of magnitude, thus the density at the surface was set to 10 cm^{-3} . The resulting changes in density and plasma flow are shown in Figures 7.8 and 7.9. The figures are of the same form as for the case with no day-night asymmetry.

Reducing the night side density, further enhances the plasma voids around the southern magnetic anomalies. Now the plasma voids are more prominent in the den-

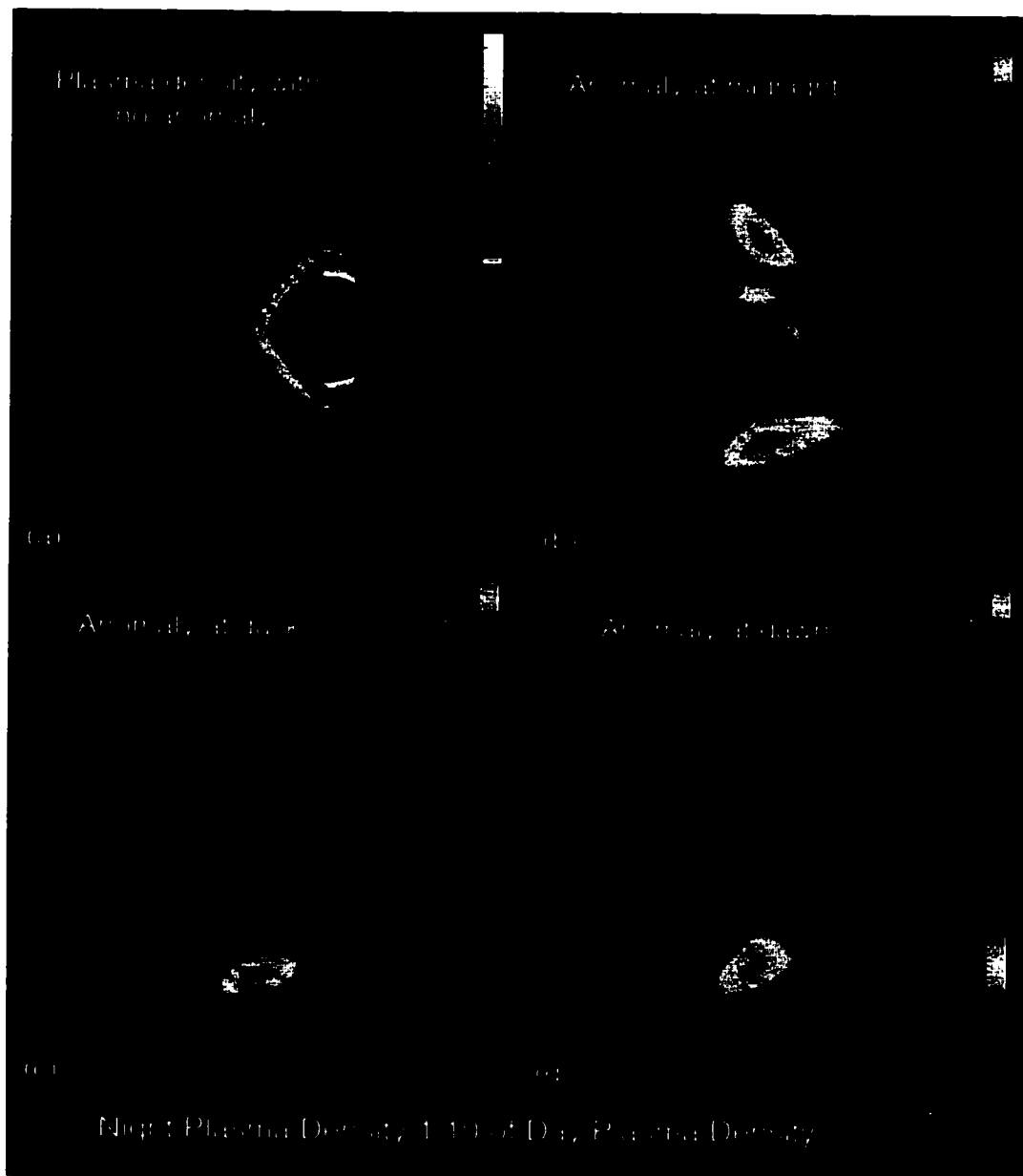


Figure 7.8: Night side Density - 1/10th reduction: The density on the night side in the same horizontal plane as in Figure 7.6 when (a) no anomaly is present and the percent change in the night side density from when no anomaly is present relative to when the strongest anomalies are at (b) midnight, (c) dusk, and (d) dawn. All initial conditions are the same as in Figure 7.6 except the night side density and pressure at the planetary boundary are $\frac{1}{10}$ th the day side density and pressure.



Figure 7.9: Streamlines around Mars for reduced night side densities: Streamlines of the plasma flow around Mars as viewed from south pole for the night side density equal to $\frac{1}{10}$ of the day side density. The four cases shown are when (a) no anomalies are present, (b) the southern anomaly is on the night side, (c) the southern anomaly is in the dusk side and (d) the southern anomaly is on the dawn side. The orientation of the plots is identical to those in Figure 7.6.

sity (Figure 7.8b) and the percent change in the pressure is up to 5 times larger. With the reduced night side density the plasma flow around the planet is not diverted as far from the planet at the terminator, instead staying closer to the planet as it travels back out the tail. This can be seen in the streamlines (Figure 7.9) pulling closer to the planet.

The reduced night side density also leads to increased reconnection of the IMF to the southern anomalous magnetic field when the anomaly is on the dawn and dusk sides. The IMF, which is held off the surface by the ionosphere can penetrate to a lower altitude due to the reduced density, allowing reconnection in regions that the IMF is excluded from for the equal density cases. The magnetic field lines when the southern anomaly is on the night side are similar in both equal and reduced night side density cases.

7.4 Conclusions

The positions of the bow shock and magnetic pileup boundary predicted by 3D simulations agree with the average positions measured by Mars Global Surveyor. The anomalous magnetic field in the southern hemisphere does not cause an asymmetric bow shock, which is also seen in MGS measurements. The simulations can not show the asymmetry in the bow shock caused by mass loading of pickup ions though, only with a full ion cyclotron treatment can that asymmetry be captured by the model. The magnetic anomalies at Mars create a magnetopause structure inside the pre-existing bow shock when the anomalies are pointed into the solar wind. Inside this mini-magnetopause, regions of the Martian ionosphere are protected from compression and erosion by the solar wind. But reconnection of the anomalous magnetic field to the IMF also creates regions where solar wind access to the Martian ionosphere is enhanced. The protection the magnetic anomalies offer is in the way of increasing the scale height of the atmosphere. As a result, these regions will also have reduced galactic cosmic radiation at the surface.

The simulations also indicate that non-ideal MHD plasma behavior occurs at both the MPB and the mini-magnetopause thus an ideal MHD Ohm's Law will not cap-

ture all of the physics occurring within the Martian magnetosphere. The electric field results suggest that collisional effect begin to modify the ion population at the MPB, as the IMF piles up at the MPB, the ions can penetrate further into the ionosphere through some sort of demagnetization process. The same thing occurs at the mini-magnetopause. Therefore in order to fully capture the physics occurring inside the Martian magnetosphere, non-ideal MHD terms must be included in Ohm's Law.

The magnetic anomalies cause asymmetries in the plasma in the tail regardless of their location on the surface. The tail plasma is disrupted most when the anomalies are on the night or dawn side. The asymmetries in the plasma density and pressure are caused by diversion of the night side plasma away from the magnetic anomalies and stagnation in the regions where the plasma is diverted to. These asymmetries are very similar to the flux spikes and plasma voids measured by Mars Global Surveyor [50].

Reducing the night side density by an order of magnitude enhances the plasma voids and stagnation points, but reducing the night side density and pressure by another factor of 5 does not cause much difference in the location or depth of the plasma voids or stagnation points. It is not clear from the simulation result though, if the plasma in the enhanced density regions is primarily from the planet or if it is of solar wind origin. The next step in the model will be include multiple species and rotation to track the dynamics of the ionospheric plasma.

Chapter 8

SUMMARY AND FUTURE SIMULATIONS

The work in the preceding chapters presents arguments that mini-magnetospheres can form around magnetic anomalies on the surface of planets or moons when no global magnetic field is present. The size and structure of the mini-magnetospheres are heavily influenced by both the ionospheric density the planetoid and the orientation of the IMF. Just changing the orientation of the IMF can lead to a doubling in the size of the mini-magnetosphere.

And as the mini-magnetospheres are small compared to planetary magnetospheres, such as at the Earth or Jupiter, particle type effects start to become important. As a result, accounting for non-ideal MHD effects in the simulations is necessary for understanding the physics involved. Non-ideal MHD terms in Ohm's law show that inside mini-magnetospheres at the Moon, the ions start to become demagnetized. And at Mars, the non-ideal MHD terms indicate that more than pileup of the IMF is occurring at the magnetic pileup boundary.

While the 3D single ion fluid simulations presented here made it possible to investigate the emerging field of mini-magnetosphere, they have limitations, which become most apparent in the Martian simulations. A single ion assumption works well for Lunar simulations where the ionosphere is negligible, but not as well for Mars which has a substantially thicker atmosphere. The peak ionospheric density of O_2^+ at Mars is only 10% smaller than the peak value at Earth. Accounting for multiple species in the Martian simulations will allow the model to account for the mass difference between the solar wind and ionospheric ions. This will lead to a more appropriate treatment of the ionosphere in the dynamics of the mini-magnetosphere and the physics near the magnetic pileup boundary. Multiple ion species may also modify the the plasma voids and enhancements seen in the tail region through the increased gravitational binding

of the ionosphere to the planet.

Ohm's law can also be further extended to capture gyrotropic effects that result from gradients in magnetic fields. Such effects have been shown to be important at the Earth, as they are needed in a simulation to capture the ring current and reconnection in the tail [74, 73]. The inclusion of neutrals will help determine what roll, if any, they play in the non-ideal MHD behavior near the magnetic pileup boundary. The role of neutrals at the MPB is currently under debate as the change in plasma population is easier to explain in the presence of a large neutral population (D. Crider, private communication, 2002). But complicating the issue is the fact that an MPB is present at the Earth's magnetopause where the neutral population is known to be too small to play a role in the formation of the MPB at the Earth. And an MPB should form under ideal MHD conditions as IMF runs into an ionosphere with high (but not infinite) conductivity.

8.1 *Martian magnetic pileup boundary*

Gyrotropic effects are expected to be significant at Mars. While the ion gyroradius for a solar wind proton ranges from 30% to 85% of the radius of Mars, ionospheric pick-up ions can have gyroradii larger than the planet radius. Gyrotropic effects can be seen in the asymmetric bow shock of the 3D hybrid simulations of Brecht [3], with the position of the bow shock at a solar zenith angle of 90° approximately 260% further from the planet than the bow shock at a solar zenith angle of -90° . Analyzing Phobos-2 data and 3D ideal MHD simulation results, Dubinin et al. [12] found that for quiet solar wind densities and velocities, and the IMF primarily in the ecliptic plane, the northern bow shock flared out compared to the position of the bow shock in the southern hemisphere but the flaring is not as pronounced as predicted by Brecht [3]. Dubinin et al. [12] note that including a population of heavy ions of ionospheric origin may reduce the flair seen by Brecht [3]. But the nature of the hybrid simulation by Brecht [3] is such that the ionosphere of Mars must be loaded gradually to keep the simulation time manageable. Hybrid simulations are also inherently noisy, thus limiting the ability to resolve small scale structures or signals in the electric fields that appear at the MPB.

The multi-fluid model is well suited for modeling Mars. It can incorporate the difference in mass between the solar wind ions and ionospheric ions. The simulations can then trace each species as it moves through the magnetosphere for non-steady state conditions, such as a change in solar wind conditions. The gyrotropic effects that can lead to an asymmetric bow shock can be accounted for in Ohm's law (Equation 8.1) by inclusion of the ∇B term.

$$\mathbf{E} = (-\mathbf{v} \times \mathbf{B}^{\text{tot}}) + \eta \mathbf{J} + \mathbf{J} \times \mathbf{B}^{\text{tot}} + \frac{1}{q_e n_e} (\nabla P_e + P_e \frac{\nabla B}{B}) \quad (8.1)$$

where all the variables have the same meaning as in Equation 2.15.

Inclusion of neutrals is also important at Mars. The neutral atmosphere of Mars extends out past the bow shock [32]. It has been suggested that the neutral hydrogen and oxygen corona is responsible for the far upstream deceleration of the solar wind [70, 32]. The atoms in the neutral corona are either photoionized or ionized within the bow shock [13]. When ionization by the bow shock, the new ions are also heated, adding to the heating processes inside the bow shock [13]. Dubinin et al. [13] propose that the atoms ionized while in the solar wind contribute to the large (greater than 30%, as opposed to the typical 1%) population of backstreaming protons relative to the solar wind number density. They theorized that this "overreflection" would lead to permanent hot diamagnetic cavities. Such hot diamagnetic cavities were seen by Mars Global Surveyor [55]. Oieroset et al. [55] ruled out that the structures were caused by the moons Phobos and Deimos, and instead proposed that these regions of turbulent magnetic field are due to a high temperature region generated when ions are reflected back up stream. But their results suggest that these regions are not as permanent as suggested by Dubinin et al. [13]. Of the approximately 250 bow shock crossings analyzed by Oieroset et al. [55], only 9 candidates for hot diamagnetic cavities were found.

The 3D multi-species MHD simulations of the solar wind interaction with Mars performed by Ma et al. [47] showed no changes in the position of the bow shock or ionopause when they included a hot oxygen corona. Including the anomalous magnetic field, did cause a dawn-dusk asymmetry in the region where the magnetic field was equal to 9 nT, their proxy for the location of the bow shock. While their model can

separately trace different ion populations, they assume all ions have the same velocity and temperature. Assuming a single ion velocity eliminates the ability to see physics generated by gravity or charge separation, such as polar outflows and ambipolar electric fields, effectively making their model a single ion species model. Their model also account for interactions with neutrals only through tuned source and loss terms in their momentum and energy equations, not through the inclusion of separate neutral fluids that interact by collisions.

The magnetic pile-up boundary (MPB) is also where mass loading of the plasma by exospheric ions begins [13, 10]. It also is a collisional boundary where solar wind ions undergo charge exchange with exospheric neutrals [10], resulting in demagnetization of solar wind ions as they are neutralized. Such demagnetization of ions can only be captured with the inclusion of the Hall ($\mathbf{J} \times \mathbf{B}$) term in Ohm's Law (equations 2.15 and 8.1). The MPB can be seen in the x-z components of the electric field in the northern hemisphere, but not the pressure (Figures 7.3 and 7.4).

Neither ideal MHD simulations, like those by Ma et al. [47], nor hybrid simulations like those by Brecht et al. [3] are able to capture all of the physics occurring at the MPB. The non-ideal nature of the boundary prevents study by ideal MHD models. And the noise in the electric field term inherent in hybrid simulations covers the signal associated with the non-ideal MHD plasma behavior. The resolution limits impose further constraints on the ability of hybrid models to effectively model the Martian magnetosphere. In the 3D simulations by Brecht [3], the ion inertial length in the solar wind was equal to 150 km, thus the finest grid resolution was slightly larger than 150 km. The finest resolution for the results shown in Figures 7.2 - 7.5 is 100 km. When simulations were run with the finest resolution equal to 200 km, the magnetopause structure shown was barely resolved. Thus the resolution limits of the 3D hybrid simulations make it difficult to resolve the mini-magnetopauses within the Martian magnetosphere.

8.2 Saturnian System

In the Saturnian magnetosphere, neutral particles dominate ions in terms of the number density by approximately 10 to 1 [57]. The sources of both neutrals and plasma are the rings and icy moons, the moon Titan and the Saturnian atmosphere. Analysis of Voyager 1 data determined there are two distinct populations of hydrogen atoms. One population is centered around Titan and azimuthally symmetric, creating a torus [65] with a peak density on the order of 20 atoms cm^{-3} [4, 61]. The second population extends radially from the surface of Saturn [65] with a density enhancement on the dusk side of Saturn due to radiation pressure effects near the orbit of Titan [66, 31]. From UV observations by Voyager, Shemansky and Hall [65] propose that the entire inner magnetosphere ($L < 25$) is filled with a background of atomic hydrogen at a density $\sim 10 \text{ atoms cm}^{-3}$.

OH atoms also occur in substantial numbers, modifying the characteristics of the magnetosphere. Shemansky and Hall [65] predict that without a large population of OH atoms, the electron temperature would be higher than observed. Their chemistry and energy model of Saturn shows that thermal electrons cool through collisions with OH atoms. Hubble telescope observations of the OH population [64, 48, 20] show a toroidal structure with a peak density of about $700 \text{ atoms cm}^{-3}$ at $4.5 R_s$. The OH density falls off both radial inward and outward to 5 atoms cm^{-3} at both $1.5 R_s$ and $11.5 R_s$. The density near the rings is approximately 30 atoms cm^{-3} . Jurac et al. [34] conducted simulations of sputtering rates from the icy moons and rings and the results were very similar to OH profiles measured with the Hubble telescope. The main sources of OH neutrals in their simulations were satellite sources, "regular" E ring sources, and an additional source near Enceladus' orbit that they theorize is the fragmented remains of a satellite, similar to the fragments found near the moons Tethys and Dione.

The Voyager satellites both measured a peak plasma density of approximately $5\text{-}10 \text{ ions cm}^{-3}$ at $5 R_s$, with a jump to $120 \text{ heavy ions cm}^{-3}$ at $2.7 R_s$ when Voyager 2 crossed the equator [57]. The heavy ions are assumed to be O^+ , but the detectors could not

distinguish between O^+ , OH^+ , H_2O^+ . The differences in the H^+ and O^+ densities in the Voyager 1 data is evidence for a ambipolar electric field [57]. Saturn's rapid rotation (10 hours, 39 minutes) leads to a strong centrifugal force on the corotating plasma and the formations of a disk of plasma near the equator. At the higher latitudes of the inbound portion of the Voyager 2 pass, the density of the 2 ion species is comparable, but in the low latitude of the outbound trajectory, O^+ dominates [57]. This ambipolar electric field is the result of the centrifugal force holding the heaviest ions to the equator and the lighter ions moving off the equator to maintain charge balance.

Both Voyager 1 and Voyager 2 detected plasma clouds at $L > 15$ [18] and Goertz [18] suggested that they were produced by a Kelvin-Helmholtz instability generated either through a velocity shear across the Titan wake or shear flow between plasma sheet flow and magnetosheath flow. Ip [30] suggests the plasma clouds could be the result of time variations in the solar wind convective electric field. Both theories could be tested with global 3D simulations of the Saturnian magnetosphere.

Single ion 3D ideal MHD simulations of the Saturnian magnetosphere have been conducted by Hansen et al. [22]. They found that the IMF controls the location and strength of dawn and dusk side stagnation points and the dissipation of the a density torus. Their model though is extremely limited in the physics that it can investigate. Being ideal MHD, and that is it can only traces one ion species, the model can neither trace the species differentiation that is so prevalent in the Saturnian magnetosphere, nor show the ambipolar electric fields generated by the species differentiation. Both effects were measured by the Voyager spacecrafts.

Voyager 1 measured a spike in electron density just as it flew past Titan at $20 R_s$ due to plasma streaming outward from Titan [57]. Voyager 2 did not, as it did not do a Titan fly-by. But when Voyager 2 encountered Saturn, the magnetosphere was compressed in comparison to the Voyager 1 encounter, and as a result the inner edge of the magnetopause was at $20 R_s$. This leads interesting questions on how the dynamics and mass loading of the Saturnian magnetosphere are altered when Titan is not inside the magnetopause. The mass loading may also fluctuate greatly during disturbed intervals when Titan possibly passes through the bow shock. The neutrals in the Ti-

tan atmosphere may experience increased ionization and heating due to interaction with the shocked plasma, similar to the ionization and heating that may generate the extended foot at the Martian bow shock.

Voyager 1 also measured an asymmetry in Titan's ionospheric wake, with higher densities measured on the Saturn-facing side of the moon [26, 19, 53]. Kopp and Ip [44] propose that this asymmetry is due to gyrotropic effects. An ambient magnetic field on the order of 5 nT and a thermal speed of 140 km/s for an N^+ ion, translates to a gyroradius of 4000 km, larger than Titan's radius. Pick-up ions will be accelerated radially outward by a corotationally driven convection electric field. Pick-up ions on the planet-side of Titan will be accelerated into the moon, while pick-up ions on the far side will be accelerated away from Titan. Such an effect can only be simulated with a model that can account from gyrotropic effects.

MHD models, such as the resistive MHD model used by Kopp and Ip [44], required an asymmetric surface density at the Titan boundary to produce the asymmetric wake. Kabin et al. [35] on the other hand propose that the asymmetry wake is due to either an induced or an intrinsic magnetic field at Titan. Their ideal MHD simulations set a value of $10^{11} Tm^3$ on the dipole moment, 1-2 orders of magnitude smaller than the dipole moments of Jupiter's moons, Ganymede and Io [62]. Simulations with the multi-fluid model described above could test both hypotheses with the same model.

The Hansen et al. ideal MHD model [21] can not investigate the gyrotropic effects that seem to dominate the plasma behavior near Titan. And the ideal MHD 3D multi-species simulations of Titan's interaction with Saturnian magnetospheric plasma by Nagy et al. [51] has the same problems. The Nagy et al. model is also identical to the model used for the Martian simulations by Ma et al. [47]. Thus the model [51] sets the velocity and temperature of the different ion species equal thereby eliminating any physics generated by having different species present, and reducing the physics down to a single ion species.

Hybrid simulations can see gyrotropic and mass differentiation though, albeit for a limited area of interest. Brecht et al. [2] conducted 3D hybrid simulations of the Saturnian plasma interaction with Titan, using a model similar to the one used for the

Martian simulations [3]. They found that the gyrotropic effects due to the pickup ions is sufficient to generate an asymmetric wake region. When they used a symmetrically loaded ionosphere on Titan, the wake was offset towards the direction of the convective electric field from the incident plasma flow direction, creating diamagnetic currents in the wake as the result of multiple ion species. The wake region became wider when the mass of the ionospheric species was increased. An asymmetric mass loading of the ionosphere produced even larger rotation of wake structures. Still the simulations were unable to replicate the magnetic field vectors seen by Voyager 1 during the Titan flyby.

8.3 The Jovian Moons

The ideas and plasma properties associated with the mini-magnetospheres around crustal magnetizations can be applied to the Jovian system as well. Measurements made by the Galileo satellite indicate that Ganymede, and possibly Io, possess an intrinsic global magnetic field [43, 40, 39, 9]. Ganymede and Io also possess an induced magnetic field, along with Europa and Callisto [42, 40, 37, 9]. In the case of Ganymede and Europa, these induced magnetic fields are thought to indicate the presence of a subsurface ocean [41, 77].

The optical measurements made at Europa indicate that the surface is covered with irregular pockets of high conductivity, briny material. These regions of localized high conductivity could modify the interaction with the Jovian magnetic field leading to structures similar to mini-magnetospheres.

And the magma erupting from volcanoes on Io solidifies in a high magnetic field. The Jovian magnetic field is on the order of 3000 nT in the vicinity of Io. If the magma cools into ferromagnetic rock, this field could be captured by the rock when solidifying, producing magnetic anomalies. These anomalies could then interact with the ambient plasma, either in the Io torus or generated by a nearby volcano to create mini-magnetospheres that may have an intermittent internal plasma source. And all of this is contained within the Jovian magnetosphere, leading to possibly feedback between the global magnetosphere and the local mini-magnetosphere.

An added bonus to the simulations of the magnetic fields at Europa and Ganymede, would be the inference of the properties of the underlying water layer. If the resulting induced magnetic fields are highly dependent on the thickness and depth of the liquid water layer, existing magnetic field data could be used as a passive probe of the subsurface structure.

BIBLIOGRAPHY

- [1] M.H. Acuna et al. Global distribution of crustal magnetization discovered by the Mars global surveyor MAG/ER experiment. *Science*, 284:790–793, 1999.
- [2] S.H. Brecht et al. Simulations of the Saturnian magnetospheric interaction with Titan. *J. Geophys. Res.*, 105:13119–13130, 2000.
- [3] S.H. Brecht. Hybrid simulations of the magnetic topology of Mars. *J. Geophys. Res.*, 102:4743–4750, 1997.
- [4] A.L. Broadfott et al. Extreme ultraviolet observations from Voyager 1 encounter with Saturn. *Science*, 212:206–211, 1981.
- [5] J.C. Cain et al. An $n = 90$ internal potential function of the Martian crustal magnetic field. *J. Geophys. Res.*, 108:10.1029/2000JE001487, 2003
- [6] P.A. Cloutier et al. Venus-like interaction of the solar wind with Mars. *Geophys. Res. Lett.*, 26(17):2685–2688, 1999.
- [7] J.E.P. Connerney et al. The global magnetic field of Mars and implications for crustal evolution. *Geophys. Res. Lett.*, 28(21):4015–4018, 2001.
- [8] J.E.P. Connerney et al. Magnetic lineations in the ancient crust of Mars. *Science*, 284:794–798, 1999.
- [9] J.F. Cooper et al. Energetic ion and electron irradiation of the icy Galilean satellites. *Icarus*, 149:133–159, 2001.
- [10] D.H. Crider et al. Observations of the latitude dependence of the location of the Martian magnetic pileup boundary. *Geophys. Res. Lett.*, 29(8):10.1029/2001GL013860, 2002.

- [11] D.H. Crider et al. Evidence of electron impact ionization in the magnetic pileup boundary of Mars. *Geophys. Res. Lett.*, 27(1):45–48, 2000.
- [12] E. Dubinin et al. The IMF control of the Martian bow shock and the plasma flow in the magnetosheath. predictions of 3-d simulations and observations. *Earth Planets Space*, 50:873, 1998.
- [13] E. Dubinin and R. Lundin. Some features of the Martian bow shock. *Adv. Space Res.*, 15(8/9):423–431, 1995.
- [14] E. Dubinin and R. Lundin. Mass-loading near Mars. *Adv. Space Res.*, 16(4):75–79, 1995.
- [15] P. Dyal et al. Magnetism and the interior of the Moon. *Rev. Geophysics and Space Phys.*, 12:568–591, 1974.
- [16] J.L. Fox et al. The Martian thermosphere/ionosphere at high and low solar activities. *Adv. Space Res.*, 17(11):203–218, 1996.
- [17] J.W. Freeman Jr. Energetic ion bursts on the nightside of the Moon. *J. of Geophy.*, 77:239–243, 1972.
- [18] C.K. Goertz. Detached plasma clouds in Saturn's front side magnetosphere. *Geophys. Res. Lett.*, 10:455–458, 1983.
- [19] D.A. Gurnett et al. The structure of Titan's wake from plasma wave observations. *J. Geophys. Res.*, 87:1383–1394, 1982.
- [20] D.T. Hall et al. Florescent hydroxyl emissions from Saturn's ring atmosphere. *Science.*, 272:516–518, 1996.
- [21] K.C. Hansen et al. A 3D global MHD simulation of Saturn's magnetosphere. *J. Geophys. Res.*, 26(10):1681–1690, 2000.

- [22] W.B. Hanson et al. The Martian ionosphere as observed by the Viking retarding potential analysers. *J. Geophys. Res.*, 82:4351–4363, 1977.
- [23] E.M. Harnett and R.M. Winglee. 2.5D fluid simulations of the solar wind interacting with multiple dipoles on the surface of the Moon. *J. Geophys. Res.*, 108:10.1029/2002JA009617, 2003
- [24] E.M. Harnett and R.M. Winglee. 2.5D particle and MHD simulations of mini-magnetospheres at the Moon. *J. Geophys. Res.*, 107:10.1029/2002JA009241, 2002.
- [25] E.M. Harnett and R.M. Winglee. Two dimensional MHD simulation of the solar wind interaction with magnetic field anomalies on the surface of the Moon. *J. Geophys. Res.*, 105:24,997–25,007, 2000.
- [26] R.E. Hartle et al. Titan's ion exosphere observed from Voyager 1. *J. Geophys. Res.*, 87:1395–1403, 1982.
- [27] R.R. Hodges. The Lunar atmosphere. *Icarus*, 21:415–426, 1974.
- [28] L.L. Hood and G. Schubert. Lunar magnetic anomalies and surface optical properties. *Science*, 208:49–51, 1980.
- [29] L.L. Hood and C.R. Williams. The lunar swirls: Distribution and possible origins. *Proc. 19th Lunar Planet. Conf.*, pages 99–113, 1989.
- [30] W-H Ip. Thermal plasma composition in Saturn's magnetosphere. *Planet. Space Sci.*, 48:775–783, 2000.
- [31] W-H Ip. On neutral cloud distributions in the Saturnian magnetosphere. *Icarus*, 126:42–57, 1997.
- [32] W-H Ip. Neutral particle environment of Mars: The exosphere-plasma interaction effects. *Adv. Space Res.*, 12(9):205–211, 1992.

- [33] F.S. Johnson. The Lunar atmosphere. *Rev. Geophys. and Space Science*, 9(3):813–823, 1971.
- [34] S. Jurac et al. Saturn's E ring and production of the neutral torus. *Icarus*, 149:384–396, 2001.
- [35] K. Kabin et al. Titan's magnetic wake: Atmospheric or magnetospheric interaction. *J. Geophys. Res.*, 105:10761–10770, 2000.
- [36] M-K. Kallenrode. *Space Physics*. Springer-Verlag, 1998.
- [37] K.K. Khurana et al. Induced magnetic fields as evidence for subsurface oceans in Europa and Callisto. *Nature*, 395:777–780, 1998.
- [38] K.L. Thomas-Keptra et al. Elongated prismatic magnetite crystals in ALH 84001 carbonate globules: potential Martian magnetofossils. *Geochimica et Cosmochimica Acta*, 64(23):4049–4081, 2000.
- [39] M.G. Kivelson et al. The permanent and inductive magnetic moments of Ganymede. *Icarus*, 157:507–522, 2002.
- [40] M.G. Kivelson et al. Magnetized or unmagnetized: Ambiguity persists following Galileo's encounters with Io in 1999 and 2000. *J. Geophys. Res.*, 106:26121–26135, 2001.
- [41] M.G. Kivelson et al. Galileo magnetometer measurements: A stronger case for a subsurface ocean at Europa. *Science*, 289:1340–1343, 2000.
- [42] M.G. Kivelson et al. Europa and Callisto: Induced or intrinsic fields in a periodically varying plasma environment. *J. Geophys. Res.*, 104:4609–4625, 1999.
- [43] M.G. Kivelson et al. The magnetic field and magnetosphere of Ganymede. *Geophys. Res. Lett.*, 24:2155–2158, 1997.

- [44] A. Kopp and W-H Ip. Asymmetric mass loading effect on Titan's ionosphere. *J. Geophys. Res.*, 106:8323–8332, 2001.
- [45] R.P. Lin et al. Lunar surface magnetic fields and their interaction with the solar wind: Results from Lunar Prospector. *Science*, 281:1480–1484, 1998.
- [46] R.P. Lin et al. Lunar surface magnetic field concentrations antipodal to young large impact basins. *Icarus*, 74:529–541, 1988.
- [47] Y. Ma et al. 3d multi-species MHD studies of the solar wind interaction with Mars in the presence of crustal fields. *J. Geophys. Res.*, 107:10.1029/2002JA009293, 2002
- [48] P.L. Matheson and D.E. Shemansky. The distribution of OH in the Saturn magnetosphere. *paper presented at XXI General Assembly, Int. Union of Geod. and Geophys., Boulder, Colo, July 2-14, 1995.*
- [49] R. Merrill et al. *The Magnetic Field of the Earth*. Academic Press, 1998.
- [50] D.L. Mitchell et al. Probing Mars' crustal magnetic field and ionosphere with the MGS electron reflectometer. *J. Geophys. Res.*, 106:23,419–23,427, 2001.
- [51] A.F Nagy et al. The interaction between the magnetosphere of Saturn and Titan's ionosphere. *J. Geophys. Res.*, 106:6151–6160, 2001.
- [52] N.F. Ness et al. Effects of magnetic anomalies discovered at Mars on the structure of the Martian ionosphere and solar wind interaction as follows from radio occultation experiments. *J. Geophys. Res.*, 105:15,991-16,004, 2000.
- [53] N.F. Ness et al. The induced magnetosphere of Titan. *J. Geophys. Res.*, 87:1369–1381, 1982.
- [54] M. Neugebauer et al. Solar wind observations of the Lunar surface with the Apollo-12 ALSEP. *Planet. Space Sci.*, 20:1577–1591, 1972.

- [55] M. Oieroset et al. Hot diamagnetic cavities upstream of the Martian bow shock. *28(5):887–890*, 2001.
- [56] G. Parks. *Physics of Space Plasmas*. Addison-Wesley, 1991.
- [57] J.D. Richardson. Thermal plasma and the neutral gas in Saturn's magnetosphere. *Reviews of Geophysics*, 36(4):501–524, 1998.
- [58] R.D. Richtmyer and K.W. Morton. *Difference Methods For Initial-Value Problems*. Interscience (John Wiley and Sons), 1967.
- [59] W.D. Riedler et al. Magnetic field near Mars. *Nature*, 341:604–607, 1989.
- [60] C.T. Russel and B.R. Lichtenstein. On the source of Lunar limb compression. *J. Geophys. Res.*, 80:4700–4711, 1975.
- [61] B.R. Sandel et al. Extreme ultraviolet observations from Voyager 2 encounter with Saturn. *Science*, 215:548–553, 1982.
- [62] G.R. Sarson et al. Magnetoconvection dynamos and the magnetic fields of Io and Ganymede. *Science*, 276:1106–1108, 1997.
- [63] L.R. Sharp et al. Orbital mapping of the Lunar magnetic field. *Moon*, 7:322–341, 1973.
- [64] D.E. Shemansky et al. Detection of the hydroxyl radical in the Saturn magnetosphere. *Nature*, 363:329–331, 1993.
- [65] D.E. Shemansky and D.T. Hall. The distribution of atomic hydrogen in the magnetosphere of Saturn. *J. Geophys. Res.*, 97:4143–4161, 1992.
- [66] W.H. Smyth and M.L. Marconi. The nature of the hydrogen tori at Titan and Triton. *Icarus*, 101:18–32, 1993.

- [67] G.A. Sod. A survey of several finite difference methods for systems of nonlinear hyperbolic conservation laws. *J. Computational Phys.*, 27:1–, 1978
- [68] C.P. Sonnet. Solar wind induction and Lunar conductivity. *Phys. of Earth and Planetary Interiors*, 10(3):313–322, 1975.
- [69] C.H. Tang. Bistatic radar measurements of electrical properties of the Martian surface. *J. Geophys. Res.*, 82(28):4305–4315, 1977.
- [70] M.I. Verigin et al. On the problem of the Martian atmosphere dissipation: Phobos-2 TAUS spectrometer results. *J. Geophys. Res.*, 96:19315–19320, 1991.
- [71] D. Vignes et al. Factors controlling the location of the bow shock at Mars. *Geophys. Res. Lett.*, 29(9):10.1029/2001GL014513, 2002.
- [72] D. Vignes et al. The solar wind interaction with Mars: locations and shapes for the bow shock and the magnetic pile-up boundary from the observations of the MAG/ER experiment onboard Mars Global Surveyor. *Geophys. Res. Lett.*, 27(1):49–52, 2000.
- [73] R. M. Winglee. Asymmetries produced in the mass loading of the magnetosphere during high dipole tilt and southward IMF. *Eos Trans. AGU, Fall Meet. Suppl.*, 83(47):SM72B-0629, 2002.
- [74] R. M. Winglee. Magnetic reconnection in the tail at global and meso-scale lengths. *Eos Trans. AGU, Fall Meet. Suppl.*, 83(47):SM61A-0473, 2002.
- [75] R. M. Winglee. Non-MHD influences on the magnetospheric current system. *J. Geophys. Res.*, 99(13):13,437–13,454, 1994.
- [76] R. M. Winglee and P.J. Kellogg. Electron beam injection I. electromagnetic wave emissions. *J. Geophys. Res.*, 95:6167–6190, 1990.

- [77] C.K. Zimmer et al. Subsurface oceans at Europa and Callisto: Constrants from Galileo magnetometer observations. *Icarus*, 147:329–347, 2000.

VITA

Erika Harnett was born and raised in Seattle, Washington. She received Bachelor's of Science degrees from the University of Washington in Physics and Math(Science) in 1995. She then completed a Masters in Physics in 1998 at the UW Physics department while studying high energy particle astrophysics. She worked with R. Jeffery Wilkes studying cosmic rays and the solar neutrino problem. She then transferred to the Geophysics program to begin studying space physics. It is there that she completed this thesis while working with Robert Winglee.